Tools for Investigating Molecular Magnetism: A New Mott Detector and Resonant Photoelectron Diffraction with Circular Dichroism

---

Dissertation

zur

Erlangung der naturwissenschaftlichen Doktorwürde
(Dr. sc. nat.)

vorgelegt der

Mathematisch-naturwissenschaftlichen Fakultät

der

Universität Zürich

von

Martin Morscher

aus

Österreich

Promotionskomitee

Prof. Dr. Thomas Greber (Vorsitz und Leitung der Dissertation)

Prof. Dr. Jürg Osterwalder

Prof. Dr. Danilo Pescia

Zürich, 2011

Die vorliegende Arbeit wurde von der Mathematisch-naturwissenschaftlichen Fakultät der Universität Zürich im Herbstsemester 2010/2011 als Dissertation angenommen.

Promotionskomitee:
Prof. Dr. Thomas Greber
Prof. Dr. Jürg Osterwalder
Prof. Dr. Danilo Pescia

Abstract

This thesis deals with topics that are related to the theme of molecular magnetism. The setup of a new electron spin detector, resonant x-ray photoelectron diffraction with structural and magnetic contrast, and endohedral fullerenes on surfaces are presented.
In the first part, we describe the design and construction of a Mott detector for spin resolved photoelectron spectroscopy. As the detector is going to be installed in an existing electron spectrometer, it has to fulfill certain requirements concerning size, stability and availability. Therefore, a scintillation scheme is used for the detection of electrons, which allows to move all electronics to outside of the vacuum chamber, close to ground potential. Additionally, the detector design was optimized for high count rates ($\approx 10^7$ counts/s per channel). First proof of principle asymmetry data have been measured.
The endohedral fullerene $Dy_3N@C_{80}$ has been studied with x-ray magnetic circular dichroism and resonant photoemission. We studied the coupling between the Dy_3N cluster and a ferromagnetic surface. Additionally, two non-magnetic endofullerenes, $H_2@C_{60}$ and $Ar@C_{60}$, have been examined with standard photoemission to better understand the guest-cage interaction and its consequence for the electronic structure of both the guest and the C_{60} molecule. For $Ar@C_{60}$, we find a large hybridization between the Ar 3p level and a C_{60} orbital with the same symmetry and a similar binding energy. Additionally, from the spectra the photoemission cross section of the Ar 3p level can be determined, which allows comparison to theoretical predictions where a giant enhancement compared to free Ar is proposed. However, this cannot be confirmed by our data.
When studying the coupling of molecules to magnetic substrates, it is crucial to first understand the substrate itself. Therefore, we developed a new method to determine the magnetization direction relative to the crystal structure, i.e. magnetic and structural properties are accessible within the same measurement. The method relies on resonant x-ray photoelectron diffraction with magnetic circular dichroism. It was demonstrated for a Ni(111) yoke crystal. The results confirm data with spin resolved photoemission of the same crystal.

Zusammenfassung

Diese Arbeit beschäftigt sich mit dem Gebiet des molekularen Magnetismus.

Im ersten Teil wird die Konzeption und Realisierung eines neuen Mott-Detektors für spinaufgelöste Photoemission beschrieben. Da der Detektor in ein bestehendes Photoelektronenspektrometer eingebaut wird, sind verschiedene Anforderungen bezüglich Abmessungen und Stabilität zu erfüllen. Aus diesem Grund wurde für den Detektor ein neues Konzept zur Nachweisung der Elektronen benutzt, das auf Szintillatoren beruht. Das darin erzeugte Licht wird über Lichtleiter über Durchführungen nach ausserhalb der Vakuum-Kammer geführt, wo es mit Photodetektoren nachgewiesen wird. Die notwendige Elektronik kann erdnah betrieben werden. Zusätzlich wurde der Detektor für hohe Zählraten optimiert ($\approx$ 10 MHz pro Kanal).

Ein weiteres Thema der Doktorarbeit sind endohedrale Fullerene. $Dy_3N@C_{80}$ wurde mit Röntgen-Zirkulardichroismus und resonanter Photoemission analysiert, wobei die magnetische Kopplung zwischen dem Dy_3N-Cluster und einer ferromagnetischen Ni(111)-Oberfläche untersucht wurde. Weiters wurde die Wechselwirkung zwischen Käfig und Gastatom bzw. -Molekül in $Ar@C_{60}$ und $H_2@C_{60}$ mit Photoemission untersucht. Im Fall von $Ar@C_{60}$ hybridisieren das Ar 3p Niveau und ein C_{60}-Orbital mit derselben Symmetrie. Die Aufspaltung zwischen dem resultierenden bindenden bzw. antibindenden Orbital kann über Photoemission bestimmt werden. Zusätzlich kann der Wirkungsquerschnitt aus den Daten bestimmt werden und mit theoretischen Vorhersagen verglichen werden, wo eine starke Überhöhung im Vergleich zu freiem Argon berechnet wird.

Ein drittes Thema dieser Arbeit befasst sich mit einer neuen Methode zur Bestimmung der Magnetisierungsrichtung einer Probe relativ zur Kristallstruktur, dh. magnetische und geometrische Eigenschaften werden in einer einzigen Messung simultan zugänglich. Das Funktionsprinzip wurde an einem Ni(111)-Kristall demonstriert. Die Resultate bestätigen Messungen mit spinaufgelöster Photoemission am selben Kristall.

List of acronyms

PSI	Paul Scherrer Institut
UHV	ultra high vacuum
STM	scanning tunneling microscopy
PES	photoelectron spectroscopy
XPS	x-ray photoelectron spectroscopy
UPS	ultraviolet photoelectron spectroscopy
ARPES	angle-resolved photoelectron spectroscopy
ARUPS	angle-resolved ultraviolet photoelectron spectroscopy
LEED	low energy electron diffraction
PED	photoelectron diffraction
XPD	x-ray photoelectron diffraction
DFT	density functional theory
h-**BN**	hexagonal boron nitride
2D	two-dimensional
3D	three-dimensional
ML	monolayer
L	Langmuir ($1\,\mathrm{L} = 10^{-6}\,\mathrm{Torr\,s}$)
MOKE	magneto optical Kerr effect
XMCD	x-ray magnetic circular dichroism
TDS	thermal desorption spectroscopy
SPI	serial peripheral interface
APD	avalanche photodiode
LVDS	low voltage differential signaling
TTL	transistor-transistor-logic
RESPES	resonant photoemission
FOM	figure of merit
SEMPA	scanning electron microscope with polarization analysis
AES	Auger electron spectroscopy

Contents

1 Introduction

Studying magnetic molecules on surfaces asks for methods that can access the electronic structure of a molecule, the magnetic state and the adsorption geometry on the surface. Photoemission spectroscopy with spin resolution is capable of measuring all this information. Up to now it is only rarely used for magnetic molecules, due to the inherently low efficiency of typical spin detectors. However, there are several advantages in using spin resolved photoemission: First, spin detectors can be used in a typical lab instead of having to apply for x-ray magnetic circular dichroism beamtime at a synchrotron, which allows to progress faster in the experiments. Second, spin resolved photoemission not only offers energy resolution but k-resolution as well. Thirdly, with pump-probe experiments the spin information can be measured time resolved. Therefore, it was decided to build a new spin polarimeter, which relies on Mott scattering, for the existing photoelectron spectrometer in the Osterwalder group. This thesis describes the setup of this detector.

A well-known method for determining structural properties of substrates and adsorbates is x-ray photoelectron diffraction (XPD). In this thesis, we describe how XPD can be extended for studying magnetic systems. The method relies on using resonant photoelectron diffraction with magnetic circular dichroism. By using the Ni(111) surface as a model system, we show how the magnetization direction can be determined in three dimensions relative to the crystal structure, which is simultaneously measured.

A particularly interesting class of magnetic molecules are magnetic endohedral fullerenes, where the most prominent member is probably $N@C_{60}$, which has been proposed as a Q-bit for quantum computing [1]. Since a few years, a new family of endofullerenes became available, the so called clusterfullerenes [2], which are composed of a relatively large cage (e.g. C_{80}) and a small cluster, often containing rare earth atoms with a high magnetic moment. A well studied example is $Dy_3N@C_{80}$, where the electronic structure has been determined by Shiozawa et al. [3], and the geometric arrangement of the cluster with respect to the cage has been studied by Treier et al. [4]. Here we focus on the magnetic properties of $Dy_3N@C_{80}$, where we are interested in the coupling to a ferromagnetic substrate.

Additionally, we report on measurements on the noble gas endofullerene $Ar@C_{60}$, where the interaction between the Ar atom and the surrounding cage is analyzed. We find a hybridization between the 3p orbital and a C_{60} orbital. Additionally, we determine the cross section of Ar in C_{60}. There are several theoretical studies on photoionization of noble gas endohedral atoms. Our data provide the first experimental test of cross section calculations.

2 Mott Detector Introduction

2.1 Methods for Measuring Spin Polarization

There are several ways to measure the spin polarisation of an electron beam. Unfortunately, the most obvious one, a Stern-Gerlach experiment, does not work for charged particles [5]. Therefore, other methods have to be used:

- Spin Polarized Low Energy Electron Diffraction: The electron beam is scattered at a well defined energy of 104.5 eV at a W(110) surface. The intensity difference between the $(2,0)$ and the $(\bar{2},0)$ spot is measured.
- Very Low Energy Electron Diffraction (VLEED): The reflection of an electron beam on a magnetized target is measured, for two opposite magnetizations. The electron beam energy is typically between 5-10 eV .
- Mott Scattering: The electron beam is scattered at a gold foil at energies from 20 keV to 100 keV. The asymmetry of the backscattered intensity at a polar angle of 120° and two opposite azimuthal angles is measured.

A review is given in [6].

The first two methods offer a relatively high efficiency, up to two orders of magnitude better than Mott scattering, but due to the low energy, the electron optics is much more difficult, and the targets are typically reactive, which makes absolute measurements over a longer time period (hours) very hard.

For these reasons, the most popular detector is still the Mott detector, although it suffers from a lower efficiency ($\approx 10^{-4}$). This detector will be described in detail below.

2.2 Mott Detector Principle

A Mott detector relies on the scattering of electrons at heavy nuclei, e.g. gold or thorium. The scattering mechanism is named after N. F. Mott who first described it [7, 8]. It is an extension to Rutherford scattering where the spin of the electron is considered. It describes an asymmetry in the angular distribution of scattered electrons if the primary beam is polarized, caused by spin-orbit interaction. For applications in spin polarimeters, Mott scattering is performed at energies around 20-100 keV in a backscattering geometry. The intensity is measured at two opposite points (typ. around 120°) defining a common scattering plane. The asymmetry is then calculated as

$$A = \frac{(N_L - N_R)}{(N_L + N_R)}$$

where N_L and N_R are the number of counts in a given time interval of two opposite counters (Left and Right).
With A and the Sherman function S, the spin polarization P can be calculated as

$$P = \frac{A}{S}$$

The Sherman function is the asymmetry that would be measured in the case of a fully polarized beam. It is in the order of 10%.
The statistical error of the polarization is given by

$$\Delta P = \frac{1}{S\sqrt{N_L + N_R}}$$

The derivation of the statistical error is given in [5].
The efficiency of a spin detector is typically expressed as the figure of merit (FOM):

$$\epsilon = \frac{N}{N_0}S^2$$

where $\frac{N}{N_0}$ is the ratio of counted electrons to the number of incoming electrons. Mott detectors typically have an FOM of $\sim 10^{-4}$.
By calculating the asymmetry of two opposite counters, the polarization along the axis perpendicular to the scattering plane can be determined. However, most Mott detectors use four counters, where one pair is rotated by 90°, which allows the simultaneous measurement of two spin directions.

2.3 Objectives for the New Design

Mott detectors are available commercially, classical and retarding field ones:

1. Classical Mott detectors by the group of V.N. Petrov, St. Petersburg

2. Retarding field Mott detectors in the Rice-University-design by SPECS and VG for their corresponding spectrometers.

None of these detectors could be considered for our system, simply for the fact that they don't fit, they are either far too long or need a CF150 flange. Additionally, the classical Motts cannot be baked to 120°C because their electron detectors which are placed inside of the vacuum chamber cannot withstand temperatures above 80°C. A service on both detectors is time consuming since it requires a shutdown of the whole system.
Therefore, it was considered to build a new Mott detector that would fit into the existing chamber. The compact size and the space limitations require a new design, that

cannot be copied from existing detectors. This allows to improve current designs and to implement new features that have not been used in the past.
Mott detectors suffer from an extremely low efficiency, typ. $\varepsilon \approx 10^{-4}$. The efficiency is limited by the physics of Mott scattering, it cannot be improved. However, the efficiency is not the only interesting quantity of a Mott detector. Another factor is the speed, i.e. the maximum count rate. In the detectors at the COPHEE experiment [9] at PSI, where detectors by V.N. Petrov are used, the count rate is limited to $2 * 10^5$ counts per second (cps). While this is sufficient for most photoemission experiments, even at synchrotrons (typ. count rates are around $10^3 - 10^4$), faster Mott detectors might be useful for Scanning Electron Microscopy with Polarization Analysis (SEMPA) [10], where electron guns are used as excitation source and secondary electrons are measured.
Electron guns can also be used for Auger Electron Spectroscopy (AES) and for analysis of the reflected and secondary electrons, i.e. the elastic and inelastic electron spectrum. For such experiments, a fast Mott detector is also useful for our system.
Another requirement is the stability of the detector. In classical Mott detectors, the electron detectors and part of the signal electronics are inside of the UHV chamber. In case of problems, a shutdown is required. Therefore, it would be advantageous to move all "active" parts outside of the vacuum. This leads to a completely different design: the electron detectors are replaced by scintillators. The light that they generate is transported with light guides to the photodetectors outside of the UHV system. The photodetectors are accessible for maintenance. The only crucial parts in the Mott detector are the gold foil and the scintillators. Gold is inert, and Mott detectors have operated with the same gold foil for many years, therefore the foil is not critical. The stability of the scintillators will be addressed in chapter 4.2.
To summarize, the design goal for the new detector are as follows:

- Compact size, based on a CF 100 flange, obeys space limitations at detector environment
- High speed measurements, maximum count rate $\sim 10^7$ cps
- All sensitive parts outside of the vacuum chamber
- Electron counting with scintillators and photodetectors

In the course of this work, the group of V. N. Petrov has constructed a detector that uses a similar concept as outlined above [11]. There, the electrons are detected with YAP-scintillators that are glued on photomultipliers. The photomultipliers are floating on the acceleration potential. A later version of the detector uses glass rods to transport the light outside of the vacuum chamber [12].

3 Design and Realization of the New Mott Detector

3.1 Boundary Conditions due to the Existing Setup

A Mott detector is typically not a stand-alone instrument, but it is used in connection with another device. In our case, the Mott will be located at the exit aperture of a VG Escalab 220 spectrometer which serves as an energy and momentum filter for the photoemitted electrons. At the time of purchase, the spectrometer was delivered with an additional tube at the exit of the analyser. This tube was intended for an optional XPS imaging unit which was not bought. The tube contains a Mu-metal shielding which is connected with the analyser. It is permanently fixed to the analyser and cannot be removed.

A good Mu-metal shielding is crucial for Mott scattering because the earth magnetic field and other magnetic fields by lab equipment would disturb the measurement. Mu-metal is difficult to handle because after machining it has to be annealed in a hydrogen atmosphere at 800 °C, which can only be done at specialized workshops.

For these reasons, the tube cannot be changed, no additional feedthroughs can be attached. All connections must be made through the CF100 bottom flange.

A sketch the tube and the exit of the analyzer is shown in figures 59 and 60.

About 15 cm below the bottom flange the monochromator of the aluminum X-ray source is located. As it is very time-consuming to remove, reattach and recalibrate the monochromator, the detector must be constructed such that it can be inserted without removing other parts at the system.

Additionally, all photodetectors and signal electronics must fit into this 15 cm space, with a light-tight cover around. A photo of the tube and its surrounding is shown in figure 1.

The photodetector and the signal electronics have to be easily removeable, because the system has to be baked at 120°C a few times per year.

A summary of all requirements due to the existing setup:

- Mu-Metal tube existing, cannot be changed
- All connections through CF100 bottom flange
- Must be mounted without removing the Al X-ray monochromator
- 15 cm space for photodetectors and electronics
- UHV compatible. All sensitive components outside of the vacuum demountable.

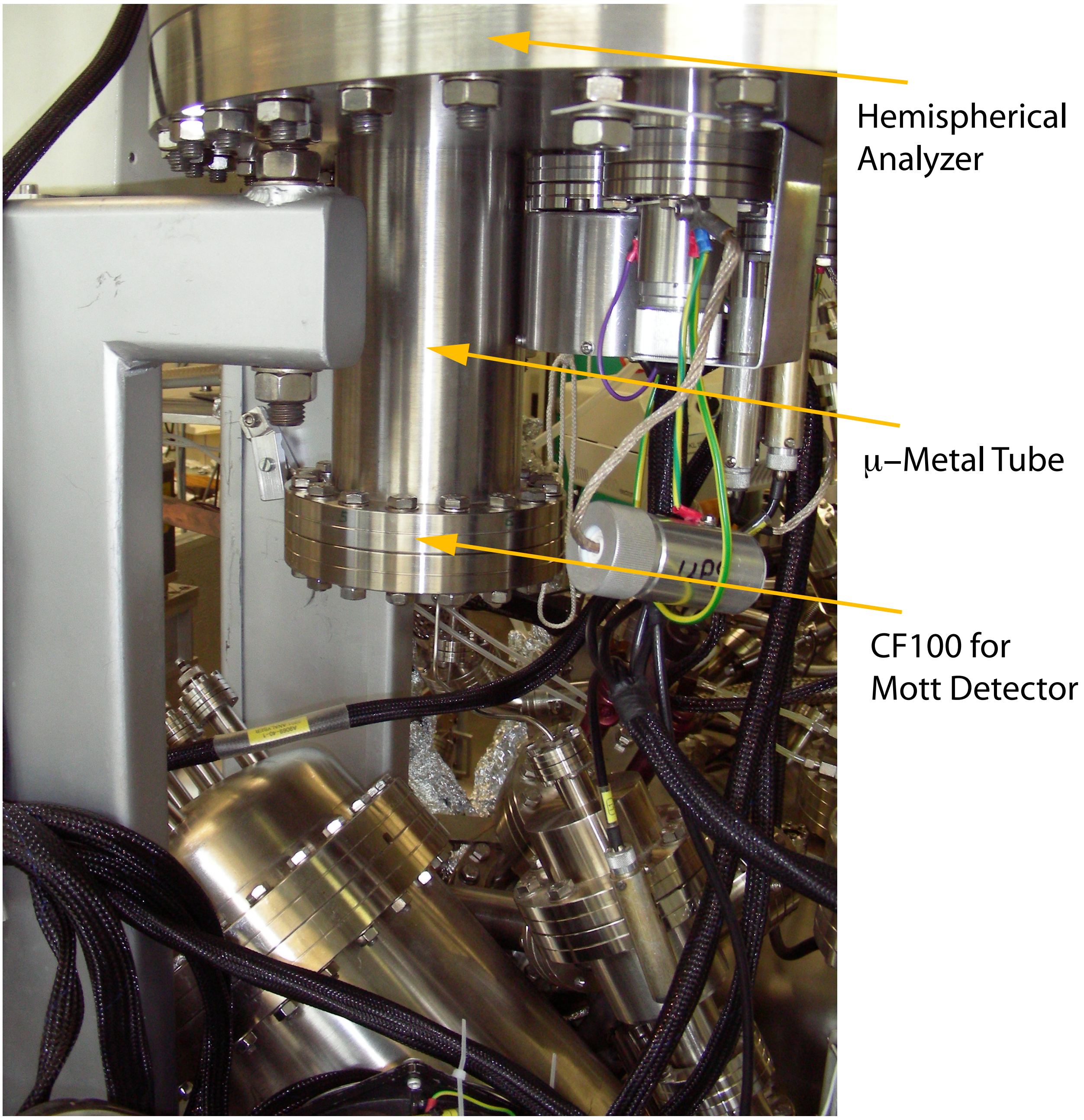

Figure 1: Photo of the tube where the Mott Detector is going to be installed.

3.2 Existing Monte-Carlo Simulations of the Mott Scattering Process

As mentioned above, the efficiency of a Mott Detector is determined by the figure of merit (FOM), $\epsilon = \frac{I}{I_0}S^2$, with I = measured electrons, I_0 = electrons entering the detector, S = Sherman function. The design should therefore be optimized concerning I and S. However, this requires a good knowledge of the angular and energy dependence of the Sherman function, since it may change its sign in the detection angle range.

There are several Monte-Carlo-Simulations for medium-energy Mott-scattering available [13],[14]. For this work, the simulations by S. Qiao and A. Kakizaki have been used [15]. They calculated I and S for different gold foil thicknesses and for different inelastic energy loss windows, and then, from these results, the figure of merit. The kinetic energy in the simulation is 50 keV.

The effect of increasing the foil thickness is twofold: On one hand, for a thicker foil the backscattering intensity increases. On the other hand, there are also more inelastic electrons that are backscattered, i.e. the Sherman function decreases. Therefore, an optimum thickness is expected. Qiao et al. calculate four FOM curves for 280 Å, 453 Å, 701 Å and 1150 Å, which are shown in figure 2 . Clearly, 280 Å and 453 Å are too thin, while for 701 Å and 1150 Å there is no significant difference. It can be assumed that for even thicker foils the FOM would start to decrease again. There is a small shift in the polar angle where the maximal FOM occurs. From these results, a thickness of 900 Å was chosen for our target. The target was produced by evaporating gold on a kapton foil. There is a uncertainty of ±100 Å in the coating process, but the simulation shows that this error is uncritical.

The inelastic energy loss window can be understood as follows: In an ideal Mott detector, only elastically scattered electrons are counted, because in inelastic scattering events the spin information may become lost. However, since the inelastic background spectrum is continuous, it is not possible to measure only elastic events. In a real experiment, the inelastic events are sorted out by pulse height analysis, i.e. the signal is fed into a threshold discriminator, where only pulses with sufficient energy can pass. As the elastic pulses also have an energy distribution due to the finite energy resolution of the detection system, the threshold has to be set slightly lower than the energy corresponding to the elastic peak energy. The difference between these two values is called the inelastic energy loss window. As for the gold foil, a change of the size of the energy window is ambiguous: A larger window clearly deteriorates the Sherman function because more electrons are counted that underwent inelastic scattering processes. However, a larger window increases the number of total events that are counted. Since the spin information is not lost for all inelastic electrons, this leads to an increase of the FOM.

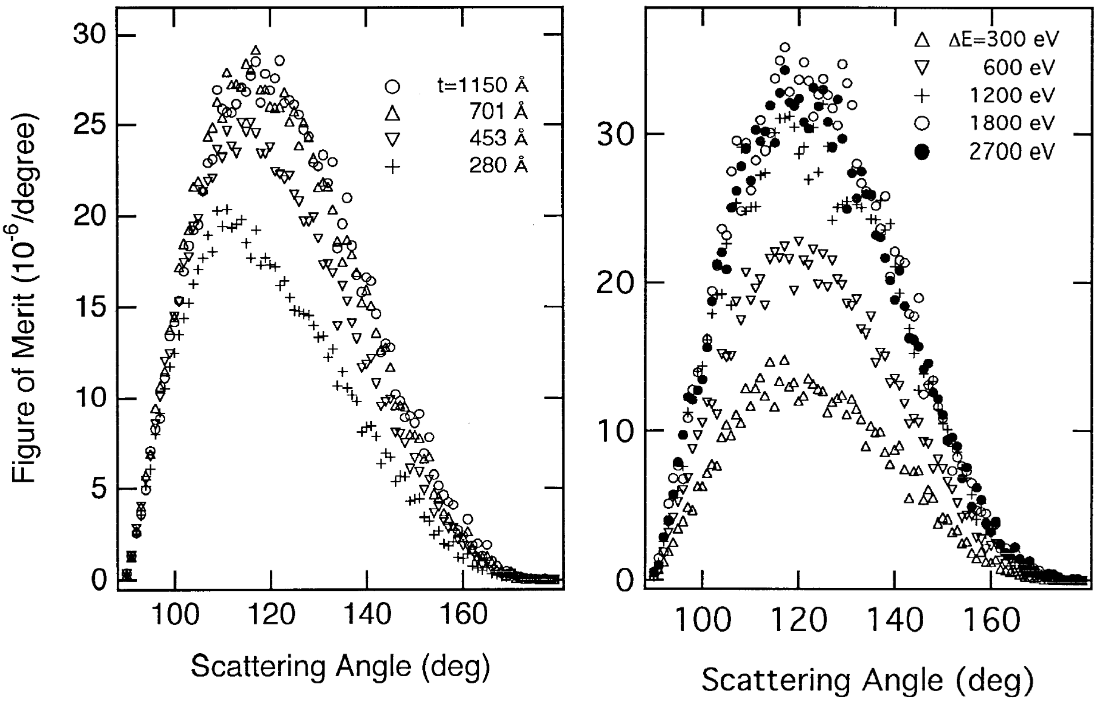

Figure 2: Monte Carlo Simulations by Qiao et al. [15]. The figure of merit (FOM) is calculated as a function of the scattering angle. In the left panel, the effect of gold foil thickness is shown. A foil with 280 Å is not useful because the backscattering is too low. For 701 Å and 1150 Å the FOM is similar. In the right panel the FOM is calculated for different inelastic energy windows. A very small window of 300 eV, i.e. excellent rejection of inelastically scattered electrons, is not expedient, because the total number of electrons that are measured is too low. The FOM is similar for values of 1800 eV and 2700 eV. This is a reassuring fact for our detector because there the energy resolution is rather poor, therefore a very large energy window has to be assumed.

Qiao et al. calculated the FOM for five different energy loss windows, 300 eV, 600 eV, 1200 eV, 1800 eV and 2700 eV. Their results are shown in figure 2. Interestingly, an excellent energy filtering is not beneficial. The FOM is rather low for 300 eV and 600 eV. For 1200 eV, 1800 eV and 2700 eV, the FOM saturates. For higher values, the FOM would decrease again, unfortunately it has not been calculated. This result is reassuring for our detector since at classical Mott detectors the energy resolution is rather poor, which causes a large energy window. The calculations show that this fact is probably not too critical.

From the simulation one can also learn where to place the detectors. As the Sherman function does not change its sign between 90° and 180°, in principle the full range can be used. A large collection angle is crucial for an efficient detector. However, for angles

$> 160°$ the FOM becomes very small, therefore we can restrict the range of detection to smaller values. The maximum of the FOM is around 120° for an energy loss window of 2700 eV. We chose to place the scintillators as shown in figure 3. They span a range of 55° polar angle, starting from an angle of 95°.

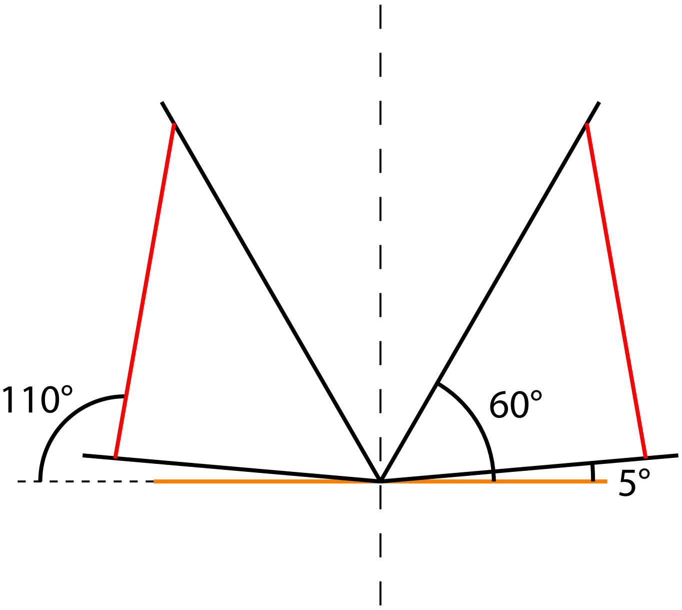

Figure 3: Final geometry that is used in the Mott detector. The scintillators (red lines) are placed such that they cover a polar angle of 55° at maximum. The orientation was chosen to minimize the bending angle between the scintillator surface and gold foil (100°) because the scintillation light is guided in a glass rod to the CF100 flange which is parallel to the gold foil. The losses are less severe if the bending angle is as small as possible.

As mentioned above, the Monte-Carlo-simulation has been calculated for 50 keV-electrons. The effect of the acceleration energy is as follows: The lower the energy, the higher the fraction of backscattered electrons, i.e. the ratio $\frac{N}{N_0}$ increases. On the other hand, the Sherman function decreases for lower operation voltages, because the discrimination of inelastically scattered electrons decreases due to the constant energy resolution of the detectors.

While the difference in acceleration voltage may be relevant for measurements, it can be neglected for choosing the scattering geometry, because the angular distribution does not change much between 40 and 50 keV. Also, the target thickness does not need to be adapted.

3.3 Basic Design Ideas for Vacuum Parts

One of the primary design goals was to achieve a compact detector which can be mounted on a CF 100 flange. This automatically limits the maximum acceleration voltage to about 40 kV, because higher voltages would require a feedthrough which would barely fit on a CF 100, leaving little space for additional feedthroughs. Also, additional insulation material would be necessary to ensure high voltage stability.

To increase the accuracy of the determination of the spin direction, electrons are measured at six points instead of four as in conventional Mott detectors. Eight would not have been possible due to space limitations. With six detectors, a determination of the S_x, S_y spin components is not possible, the direction is now found by fitting a sine curve through the six data points. This requires an accurate determination of the instrumental asymmetry, i.e. a reliable zero-measurement has to be made.

3.3.1 Gold Target:

The gold target was produced by evaporating 90±10nm gold on a kapton foil with 30 µm thickness. The gold film thickness was chosen by considering the Monte Carlo simulations by Qiao et al. mentioned above [15].

The thickness is a compromise between two effects: For a thicker gold foil, the number of backscattered electrons increases. However, the rate of inelastic scattering events in the gold foil also increases.

3.3.2 Scintillator

There were three important requirements to the scintillation material:

1. Speed: One design goal of the detector was to achieve count rates $\geq 10^7$counts/second. Therefore, a sufficiently fast material is needed with a scintillation decay time (typically the 1/e - time is given) of below 100 ns. This is already a stringent requirement that excludes many materials.

2. Light yield: Due to the relatively small acceleration voltage of 40 kV, a scintillator with a high light yield is necessary. However, this is often in conflict with requirement 1. As an example, one of the most efficient scintillators is NaI(Ti), i.e. NaI doped with Ti. At room temperature, the photon yield for electrons is 38000 photons/MeV. However, it is relatively slow with a decay time of 230 ns.

3. Non-hygroscopic: Todays best scintillators in terms of light output and decay time are hygroscopic. Unfortunately, we cannot use hygroscopic scintillators. Typically, these materials are processed in controlled atmospheres, e.g. glove boxes, and then

packaged into protection boxes with a thin entrance window. However, since we work with medium-energy electrons, any entrance window would absorb most of the electrons.

There is a wide range of scintillators available. Depending on the type of application, organic, inorganic or liquid scintillators are used. For our purpose, liquid scintillators are obviously not feasible. Inorganic scintillators are the most common scintillators. Typically high-Z materials are used to achieve short attenuation lengths. One of the best known inorganic scintillators is NaI(Ti). In typical data sheets the light yield is given compared to this scintillator. Here, despite its large light yield, NaI(Ti) is not suitable because of its long decay time constant of 250 ns. There are not many materials that fulfill both speed and light yield requirements at the same time. The three best materials available are Yttrium Aluminum Perovskite (YAP, decay time 25 ns, 70% light yield relative to NaI(Ti)), YSO (Yttrium Oxyortho-Silicate, decay time 35ns, 50% light yield relative to NaI(Ti)) and Lutetium Yttrium Silicon Oxide (LYSO, 41ns, 75% light yield, slightly radio-active due to Lutetium). We chose to evaluate a YAP crystal by Crytur, Czech Republic. The results are shown in chapter 4.2.

The last type are organic scintillators. They consist of a base material, e.g. polyvinyl toluene, and a dye molecule. Due to the low Z, they are impractical for typical high energy detectors since a large absorbing volume would be required, but the high hydrogen content makes them very useful for neutron measurements. For our purpose, the low Z is not critical since the penetration depth of electrons at 40 keV is in the order of µm. The real advantage of plastic scintillators is the extremely fast decay time of typ. 3ns, i.e. at least an order of magnitude faster than inorganic scintillators. This makes them ideally suitable for high speed applications.

The light yield is typically around 48% of YAP. In our case, this is still acceptable, though a higher photon number per electron would be advantageous.

Another important advantage of plastic scintillators is that they are available as resins that can be molded in arbitrary shapes and then are fully polymerized. We chose to evaluate the Scintillator BC-490 by Saint Gobain. It consists of three components, a resin, a catalyst and a catalyst solvent that have to be mixed in a suitable ratio. The light output is slightly lower than for normal plastic scintillators, it is ≈44% of YAP.

Here, the scintillator is directly applied on the light guide end face. This avoids a gap that would introduce reflection losses. On glass the scintillator gets a convex shape, which means that the thickness is not uniform over the diameter of the light guide (see figure 3.3.2). Due to the small penetration depth of electrons at 40 keV, this is not problematic except for the rim.

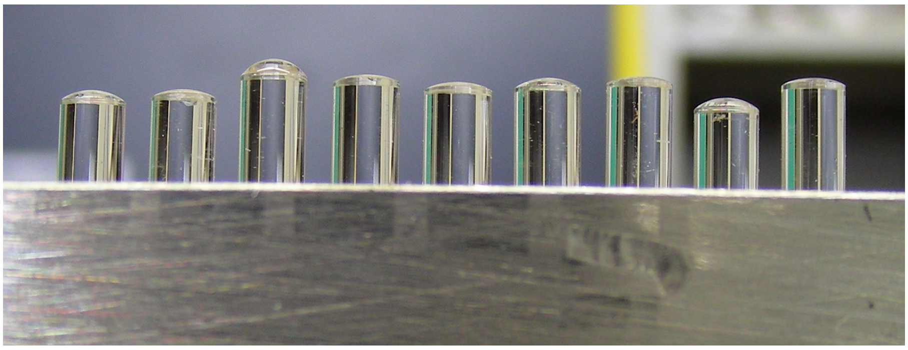

Figure 4: Photo of nine glass rods that are covered with plastic scintillator. Due to surface tension, the scintillator has a drop-like shape.

After producing the drop, the scintillator has to be cured at 80°C for eight hours and then post cured at 50°C for one week. Saint Gobain recommends to use an oxygen free atmosphere during production of the scintillator and during curing. Therefore, the drops were applied in a glove box with a controlled nitrogen atmosphere. The light yield doubles compared to a preparation in normal air.
An image of the scintillators is shown in figure 3.3.2.
Two other promising, new scintillators that have not been evaluated should still be mentioned.

- LaBr3: This is a new scintillator developed by groups in Bern and Delft [16]. It is available through Saint Gobain as “BrilLanCe 380”. It would be the perfect inorganic scintillator: it has a decay time of only 16ns and a light output of 165% compared to NaI(Ti). However, it is hygroscopic, which makes it impossible for us to use.

- ZnO: This is an old, well known material for phosphor screen applications. Typically it is doped with Ga. It has been known since a long time to have an extremely short decay time of below 1 ns. However, it was only available as a powder. Recently, ZnO:Ga has become available as a single crystal material through Cermet Inc. However, up to now there have not been many studies, its light yield under electron excitation is not known.

3.3.3 High Voltage Considerations

There are not many insulating materials that can be used in UHV chambers. The most common ones are glasses for viewports. For electrical insulation mostly sapphire based parts or ceramics are used. However, these materials are usually hard to machine. The best material for involved UHV parts is macor, a glass-ceramic material. Its dielectric strength is 40 kV/mm. It has to be emphasized that this value is the strength of the electric field when the material breaks down. The electric field at an operating voltage of 40 kV can exceed 40 kV/mm by far in special geometries or short distances. A well known example is the field enhancement at sharp tips. A general design rule is therefore to keep the electrical field strength as low as possible by avoiding sharp objects. Another consideration is to keep the parallel component of the electric field on the surface of the insulator as low as possible. Typically the normal component is uncritical, since macor, teflon or other UHV-compatible insulators have an extremely high dielectric strength, i.e. no breakdown is expected through the bulk. However, the surface poses new problems. In UHV, discharges typically start from field emission currents. Such currents are unavoidable, as the electrode surfaces are never perfectly flat, there are always some sharp edges or tips that may act as field emission centers. However, the current is normally extremely small. If electrons hit the insulator, two phenomena happen. An electron can produce a secondary electron avalanche causes a breakdown, or the insulator may charge, resulting in a breakdown as well. Therefore it is advantageous to keep the parallel field as small as possible to prevent electron transport on the surface. Additionally, the shortest path between two electrodes, i.e. the region of highest field strength, should be far away from the insulator, because field emission happens at high field strength. Other factors that help to decrease the probability for high voltage breakdown is the use of intermediate potentials, as in [17] and the polishing of all electrodes to avoid field emission centers. The insulator also requires special care. In UHV it is normally custom to clean all parts with organic solvents, typically acetone or ethanol. However, for insulators it is better to abstain from using them, because a solvent might leave remnants on the surface that may become graphite-like during a bakeout and thereby conducting.

A good introduction to high voltage considerations for applications in high vacuum is given in [18].

3.3.4 Light Guide and Feedthrough

As mentioned above, the acceleration voltage is limited to 40 kV due to the geometrical constraints. At this energy, electrons produce ≈ 440 photons in BC 490 which have to be transported to the photodetector. The light guide has to be highly efficient, yet must be compact enough to fit into the setup. In a Mott detector, backscattered electrons are measured. However, the feedthroughs for the light guides have to be on the CF100 flange, as there is no other flange available. As a consequence, the light guide has to be curved by more than 90°. Additionally it has to be integrated into an UHV compatible feedthrough. Another important issue is the cross-section of the light guide. The diameter of the scintillator defines the active area of the Mott detector. For practical

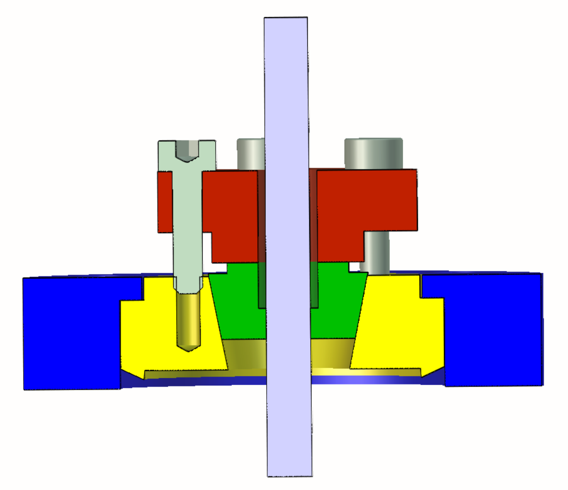

Figure 5: Glass rod feedthrough with aluminum gasket. The feedthrough is UHV compatible and bakeable to at least 130°C.

reasons this area should not become too small. In principle it would be possible to use a lens system to couple the scintillation light into a glass fiber or to use a lens/prism/mirror system. However, these ideas were discarded as too complicated. A fiber bundle was also considered, but there it would be difficult to construct a feedthrough, and due to the packing factor a considerable number of photons would be lost.

The solution that was chosen consists of a glass rod with a diameter of 3 mm. The light is guided simply by internal reflection, no additional cladding is coated. It is bent by 100° such that its end face is oriented close to the collision point. The rods were bent by Willi Möller AG in Zürich. A sketch of the glass rod is shown in figure 12.

The material of the glass rod is quartz. Ordinary lab glass, e.g. Pyrex, has too many defects, so that the light transmission is too low over the total length of 227.2 mm. The transmission around the emission wavelength of the scintillator (420nm) is close to 100% for both materials (when refraction at the end faces is not considered). It is crucial to polish the end faces of the glass rods as scattering at the interface could reduce the photon number considerably.

The feedthrough was designed following a short article by Abraham et al. [19] who reported of a feedthrough for glass fibers with a diameter of 120-160 µm. Their design is based on a Swagelock connector where the ferrules are replaced by a teflon cylinder whose shape resembles the ferrules. A hole is drilled into the axis of the cylinder and the fiber is fed through this hole. When the Swagelock connector is tightened, the teflon is compressed, thus sealing the leak around the glass fiber. With this feedthrough, Abraham et al. report pressures below $2*10^{-10}$ mbar, where the pressure is not limited by the feedthrough.

Initially, we have closely followed this design. However, it turned out that for our purpose teflon is not suitable. After baking the UHV chamber with the feedthrough mounted, the pressure is often at the normal level of $2 \cdot 10^{-9}$mbar, though sometimes a leak occurs. The leak can be easily closed by simply re-tightening the Swagelock connector. The main problem is that the teflon is not tight against small atoms/molecules, e.g. helium, which can be measured during leak checking. Therefore, the teflon was replaced with aluminum. To avoid rotation during compression, the design was changed, such that the aluminum gasket is compressed only vertically. Pure aluminum was used, as its alloys are usually harder. A sketch of the design is shown in figure 3.3.4. The feedthrough is mounted on a rotateable CF 16 flange. It is tight and bakeable. It was tested up to 130°C. During tightening, a small distortion in axial direction is unavoidable, as the aluminum and the copper gasket of the CF 16 flange are compressed.

An additional advantage of using aluminum instead of teflon is the light loss at the feedthrough. While the transmission with teflon is roughly 50%, it increases to ≈90% with aluminum, for a glass rod diameter of 5 mm and a contact length of 2mm.

3.4 Light Detector

As mentioned above, the number of photons that are produced at 40 keV is very low. The number of photons that arrives at the photodetector is around 100 photons. However, not all of these photons contribute to the measured signal, but the wavelength dependent response of the photodetector has to be considered. In data sheets, the response is either given as photocathode radiant sensitivity or as quantum efficiency. The radiant sensitivity is defined as the ratio between the current produced by the photocathode and the incident radiation flux. It is given in Ampere per Watt (A/W). The quantum efficiency is defined as the ratio between photoelectrons that are emitted from the cathode and the incident photon number. It is given in %. These two quantities are related by

$$\eta(\%) = \frac{1240}{\lambda} * Sk(\frac{A}{W})$$

with η=quantum efficiency, λ=wavelength of the incident light in nanometer, Sk=radiant sensitivity in A/W [20].

For this detector, obviously a high quantum efficiency around 420nm is needed. There are several types of light detectors on the market that have been considered. They can be categorized into two classes: semiconductor devices and photomultipliers. The latter has been the workhorse for low light level detection for a long time. Its main advantage is the high gain of typ. 10^6 which allows single photon detection without sophisticated amplification electronics, in principle an oscilloscope is sufficient. Semiconducting devices on the other hand are superior concerning quantum efficiency which can be up to 90%.

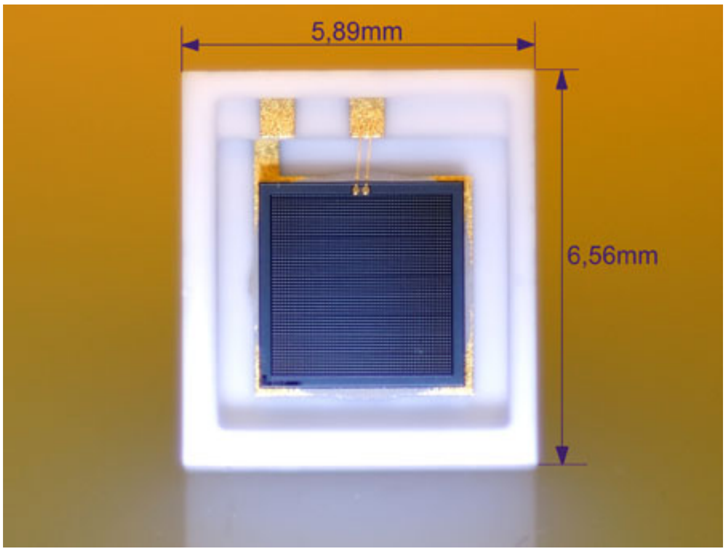

Figure 6: Photo of a Hamamatsu S10362-33-050C GAPD. The housing is made of ceramics.

However, the standard light detector, the photodiode, is not suitable for our purpose because it has no internal gain, i.e. one photon creates one electron-hole pair. For low light levels, it is often impossible to measure anything, even for pulsed light. A semiconductor detector with internal gain is the avalanche photodiode (APD). It is a diode which is operated in reverse bias. An incident photon creates an electron-hole pair. Due to the high voltages which are typically applied to an APD, the charge carriers are accelerated and subsequently multiplied by impact ionization.

Typically, APDs are operated at a gain of ≈100. By increasing the operating voltage, the gain can be increased up to 1000, then the device starts to breakdown continuously. The breakdown voltage is strongly temperature dependent, since thermal fluctuations start the breakdown. It has been shown by Dorokhov et al. [21] that at liquid nitrogen temperatures APDs can be operated at a gain of up to 10000. At the same time the dark count rate, which is also strongly temperature dependent, drops dramatically. While this is interesting for single photon counting applications, here liquid nitrogen temperatures are impractical. APDs are operated in the linear regime, i.e. the number of electrons or holes in the avalanche is proportional to the energy of the incident photon (or to the number of simultaneous photons).

APDs are operated below the breakdown voltage, in the so called linear regime. Here the current is proportional to the deposited energy.

In recent years there has been enormous progress in the development of so called Geiger Mode APDs (GAPD), also referred to as Solid State Photomultiplier (SSPM) or MultiPixel Photon Counter (MPPC). Essentially this is an APD which is operated slightly

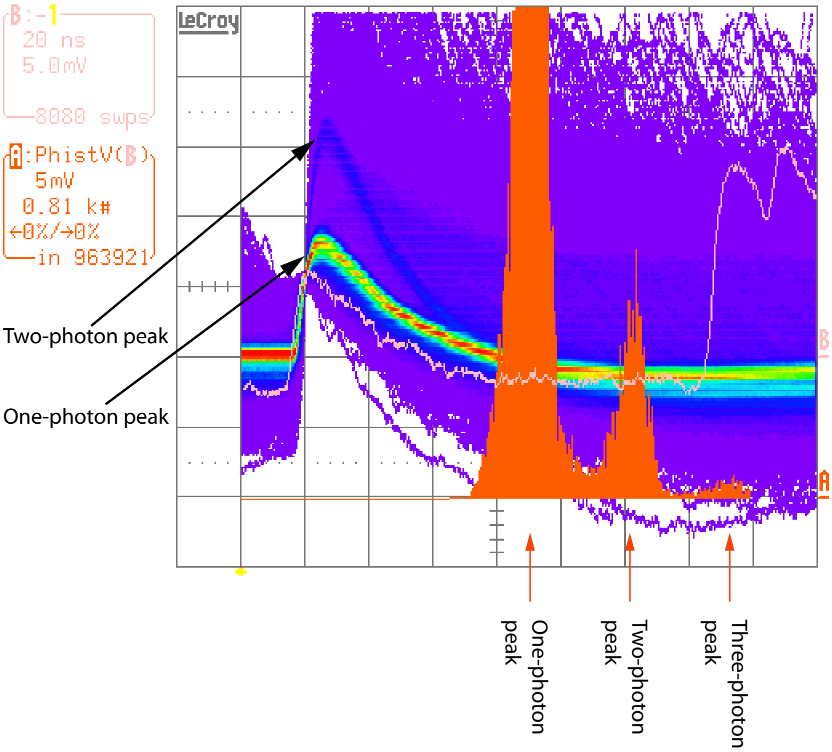

Figure 7: Oscilloscope image of a Hamamatsu S10362-33-050C GAPD connected to a preamplifier “AMP-0611” by Photonique. Two strong bands are visible, one which is interpreted as the signal representing a one-photon-event, and a weaker one which occurs when two photons are detected simultaneously. The rise- and fall time of the signal is determined by the preamplifier, the GAPD is much faster. The AMP-0611 has a rise time of 700 ps and a fall time of around 20ns. The orange curves represent a histogram of all signals. Three peaks are discernible, a dominant one-photon peak, a weaker two-photon peak and a tiny three-photon peak.

above the breakdown voltage. If the current is limited by a resistor the current is unstable and stops by itself. An external excitation is needed to restart the current flow, e.g. a photon that creates an electron hole pair. Such an electron hole pair will start an avalanche that discharges the APD. A GAPD can be understood as a binary device, i.e. the output pulse is not proportional to the incident pulse energy or to the light pulse intensity, it can only differentiate between photon or no photon. To circumvent this problem, GAPDs do not consist of a single APD, but they consist of several hundred or thousand single APDs that are arranged in an array. By combining the digital information of each pixel, light intensities can be measured in terms of photon numbers. Due to the array arrangement the APD cells do not cover the whole active area, there is passive space surrounding each pixel. This decreases the photon detection efficiency of the GAPD. Fortunately, the intrinsic quantum efficiency of Si APDs is very high, around 90%, so that the final photon detection efficiency can be still as high as 65%, depending on the filling factor of the single pixels.

Due to the operation above the breakdown voltage, the dark count rate is extremely high, typ. several megacounts/s. This makes GAPDs unfeasible for normal single photon counting experiments (at room temperature), but for scintillation applications this is not critical since the photon number per pulse is typically far higher.

A disadvantage of GAPDs is the large temperature dependence of the gain, it increases 10% per degree.

For our detector we evaluated an MPPC by Hamamatsu, the 3x3mm model S10362-33-050C. In figure 7, we show an oscilloscope measurement of the output of a GAPD and an amplifier (AMP0611 by Photonique). The image shows two curves, the signal and a histogram of the pulse height distribution. In the signal, two bands are clearly visible and marked with two arrows. The strongest band corresponds to single photon events. There is a second band coming from two-photon events, i.e. two photons arriving at the same time. In principle there is also a three-photon band and a four-photon band, but they are too weak to be seen on the oscilloscope. However, in the histogram, at least the three-photon peak shows up. Remarkably, in both the signal curves and the histogram, the peaks corresponding to different photon numbers can be easily distinguished. This allows an easy calibration of a scintillation spectrum in terms of photon numbers. It should be emphasized that here no real photons were measured, only the dark counts of the GAPD were used.

Figure 6 shows a photo of a Hamamatsu S10362-33 GAPD.

3.5 Power Supply

The power supply for Mott Detectors should fulfill several requirements. Apart from the obvious, like safety, user-friendliness, reliability, it should be resistant to high voltage breakdowns, even when a large capacitance, i.e. the detector, is connected to the power supply. Its high voltage should be stable, reproducible and ripple-free.

Additionally, the power supply should be resistant to temperature and humidity variations. This is important in environments without air conditioning.

We chose to use the power supply MP40 by Spellman, which can deliver up to 200 µA at 40 kV, or $\approx 10^{15}$electrons/s. This exceeds the count rate of the detector by far, i.e. the detector is not limited by the power supply.

The power supply has a monitor output for both voltage and current.

For safety reasons, there are three interlocks that switch off the power supply. One interlock is controlled by the cold cathode gauge at the test chamber. If a certain pressure is exceeded, the high voltage switches off. This may happen e.g. during an accidental venting of the UHV chamber, or after a high voltage breakdown. A second interlock is operated by the cooling water guard. Finally, there is a manual interlock on the case of the high voltage supply.

Between the detector and the high voltage supply, a 1 GΩ resistor has been added to protect the power supply. In case of high voltage breakdown, the peak current is limited by the resistor.

3.6 Design of Electron Optics

The electron optics has been designed using the SIMION software. It solves the Laplace-Equation for any electrode configuration which can be defined in the program. The geometry can be either drawn in SIMION itself, determined with script files or imported from CAD-software. The electron trajectories in the calculated potential can be simulated by raytracing. SIMION is restricted to metallic electrodes, it cannot simulate dielectric materials. Space-charge effects are also not included.

An introduction to electron optics is given in [9], a detailed description of SIMION can be found on the web [22].

Typically, the electron optics of classical Mott detectors is given by two concentric hemispheres, with one near ground potential and one connected to the high voltage. The accelerating field for the electrons is therefore located between the hemispheres, its shape such that the focus should be ideal in the center point. However, after simulating this scheme including realistic conditions at the analysator exit/Mott entrance, the hemispheres were abandoned in favour of a simpler optics with two lenses.

One design goal was to operate without grids since the transmission of electrons through a grid is typically below 80%. Then, however, the high voltage potential is not screened any longer and it will penetrate into the lens system, which makes it harder to design, especially since the lenses should operate below 2 kV.

A simulation of the final design is shown in figure 8. The detector was simulated in cylinder symmetrical geometry, i.e. the sixfold symmetric construction of the detector with the six glass rods is not considered. However, the glass rods can be neglected since they are screened by the high voltage hat on the central part of the detector.

The beam was simulated starting from the beginning of the exit slit of the analyser. This is about the same height as the entrance of the channeltrons. At this point, the kinetic energy of the electrons corresponds to the pass energy, which we use as the initial energy in the simulation. The electrons are guided through a trapezoidal channel (see figure 60). Then the electrons enter the Mott detector. The lenses are mounted on a cylinder which is isolated from ground potential, it is connected to the herzog plate potential, so there is no additional potential along the trajectory of the electrons.

The electron optics was simulated for four different pass energies: 2 eV, 5 eV, 10 eV and 20 eV.

With the design presented here, spot sizes of 300 μm for entrance energies between 2 and 20 eV are predicted.

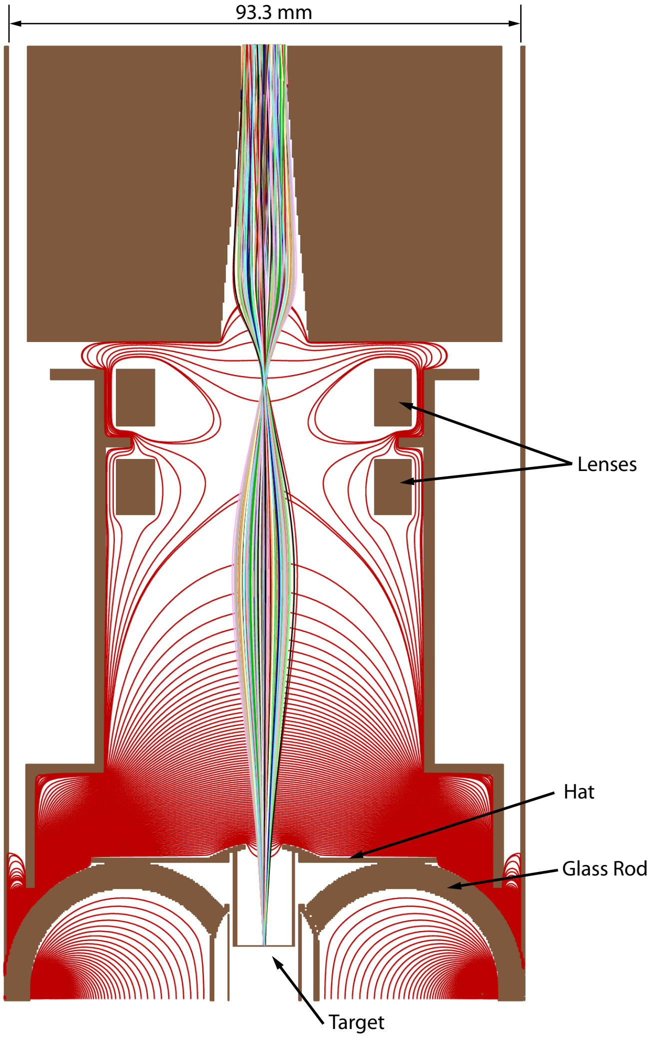

Figure 8: Electron optics simulation with SIMION. The electrons (multicoloured lines) enter the detector through the trapezoidal entrance channel at the top. Then they are accelerated/decelerated by two lens elements before the final acceleration step towards the target. The glass rods are shielded behind the acceleration electrode. Several equipotential lines are drawn with red color.

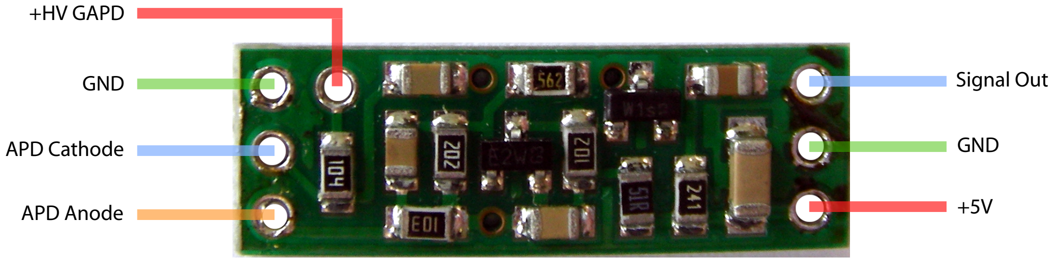

Figure 9: Amplifier AMP-0611 by Photonique. The GAPD is directly soldered on the amplifier to avoid noise pickup.

3.7 Signal Electronics

3.7.1 Amplifier

The GAPDs have an internal gain of $\approx 10^6$. Despite this high value, the signal still needs further amplification for reliable operation. We use the amplifier “AMP-0611” by Photonique, Geneva. Its key features are a signal amplification of 10x-20x and a signal rise time of 700ps. The amplification depends on the supply voltage. At 5V, it is $\approx$ 12x. The amplifier is AC-coupled, both at the input and at the output.

The GAPD is directly mounted on the amplifier to avoid noise pickup on cables. A photo of the amplifier with the signal connections is shown in figure 9.

3.7.2 Electronics

During the course of this work, two versions of the signal electronics have been used. For completeness both will be described here. The second one (see figure 11) is an improved version of the first one (figure 10), the concept is the same for both versions.

The main idea for the signal processing chain is shown in figure 13. A photon creates an electric pulse in the GAPD. The pulse is then amplified. For technical reasons, the output of the amplifier is put on a potential of 2.5 V in the first version of the electronics and on 3.88V in the second version. Then the signal is fed into a fast comparator. In the first version, it was an ADCMP604 by Analog Devices. The signal is compared to a reference voltage, which needs to be controllable to set a defined cutoff. Therefore, the it can be controlled with a computer programmable digital potentiometer (MCP41010 by Microchip, 8 bit resolution) which is accessed via a standard SPI interface. The potentiometer range is chosen to be $\approx$100 mV.

In the second version of the electronics, the comparator is an ADCMP605, again by Analog Devices. The main difference to the old comparator is a hysteresis option. This

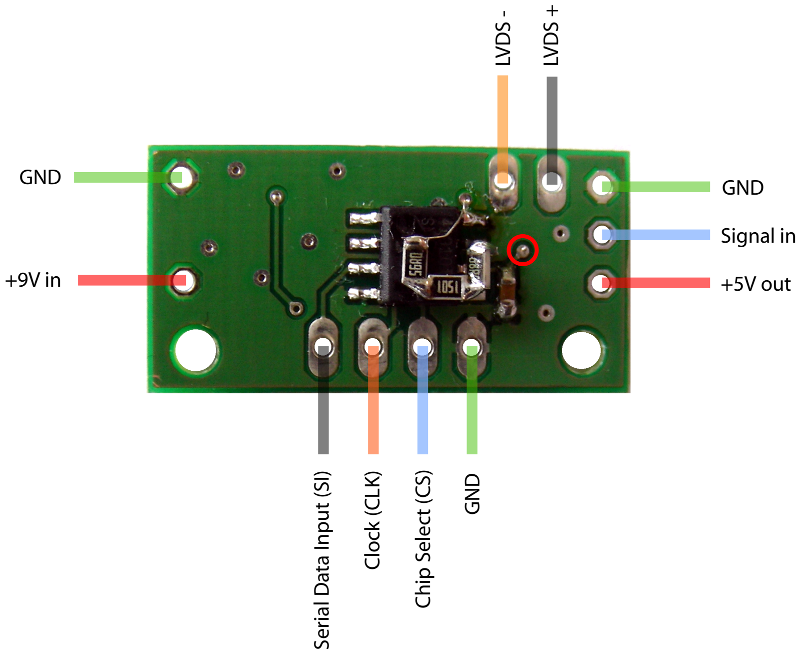

Figure 10: First version of the electronics. The chip in the middle of the board is the programmable potentiometer. The comparator and LVDS driver are on the backside.

is important for small and noisy signals. For an ideal pulse, a comparator would start a logic output when the pulse exceeds the threshold and then end the output when the pulse falls under the threshold. However, in reality the input signal is noisy, therefore the comparator will trigger also on noise. A comparator with a hysteresis has a lower threshold for ending the output, thus the comparator is less sensitive to noise, the output ends when the pulse is really finished.

Both comparators include a Low Voltage Differential Signaling (LVDS) output. LVDS has to be used because the distance between detector and measurement computer can become quite long, at least 3m. For such long distances, TTL based signal transmission becomes unreliable at high rates (10 MHz).

In the first version, the LVDS signal was directly transferred to an interface box close to the measurement computer via an ethernet cable. The interface box translates LVDS into TTL, which is the signal level suitable for the counter card which we use, a National Instruments 6602. The card offers eight 32bit counters, 80 MHz source frequency and up to 32 digital input/output (DIO) lines. In the interface box, optocouplers are used to separate the grounds of the detector and the computer to avoid ground loops and noise pickup from the computer power supply.

The counter card has certain specifications for the input pulse. The TTL pulse must be at least 5 ns long, followed by a pause of at least 7.5 ns before a new pulse is accepted.

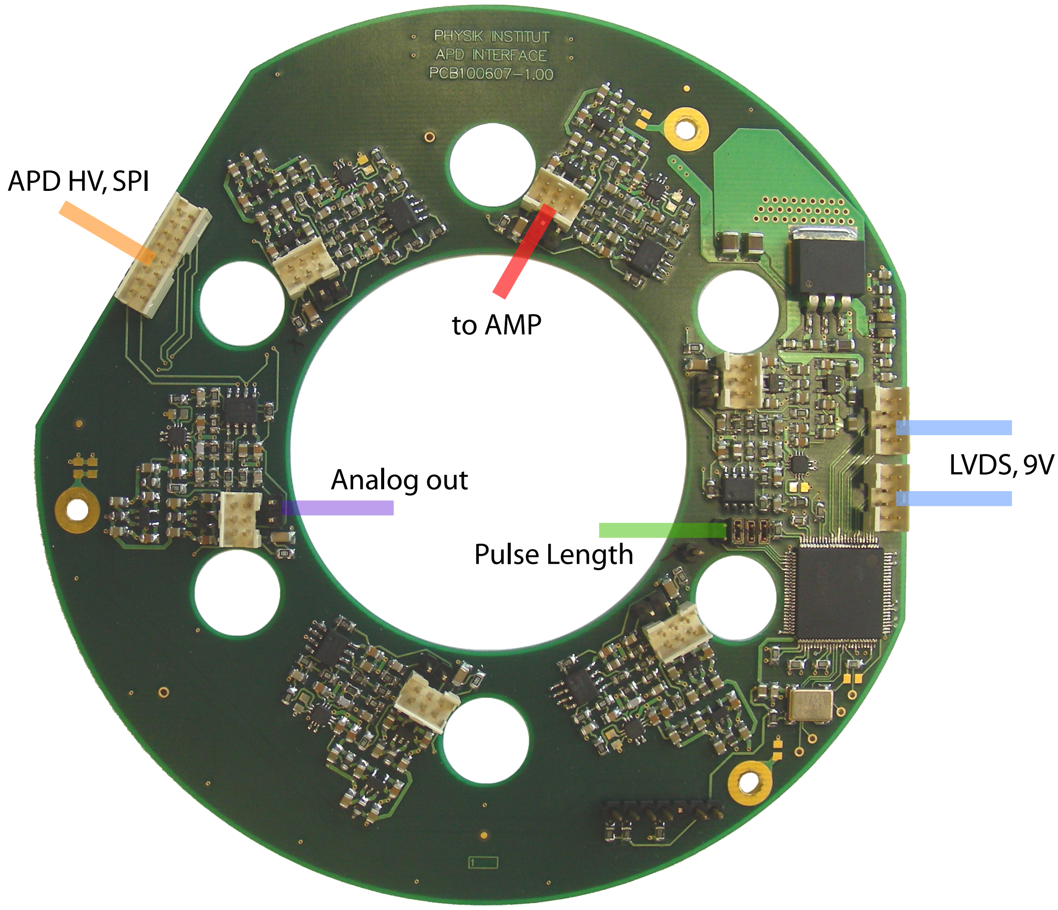

Figure 11: Final version of the electronics. The output pulse length can be controlled with jumpers in a range from 5 to 70ns. Optionally the analog pulse from the GAPD/amplifier can be picked up before the discriminator to analyse the waveform.

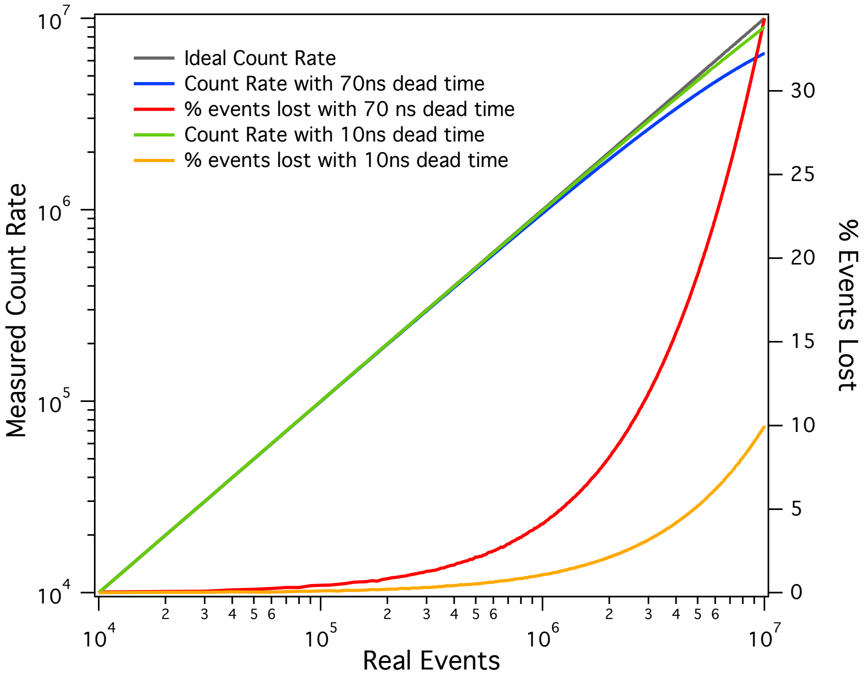

Figure 12: Effect of dead time in the counting electronics on the measured signal rate.

In the first version, this timing requirement was not controllable, the pulse duration was given by the GAPD pulse length plus the noise on the signal as explained above. Therefore, in the second version an additional logic chip (LCMXO1200c by Lattice Semiconductors) has been added to control the LVDS pulse length directly. The chip can be programmed to generate pulse lengths in the range of 5-70ns. A longer pulse length obviously decreases the maximum count rate of the detector. In figure 12, the effect of pulse length has been calculated for two values, 10ns and 70 ns. We compare the number of real events to the number of events that are actually measured when we assume a certain pulse length. The pulse length can be understood as dead time, i.e. during the output pulse the channel cannot accept new pulses. It is important to understand that this effect can introduce artificial asymmetries between the different channels of the Mott detector. More seriously, the artificial asymmetry depends on the real asymmetry and on the count rate. Let us assume a situation with 1.000.000 real events in counter 1 and 750.000 real events in counter 2, i.e. an asymmetry of 14.3%. The measured count rate, however, is 726440 events in counter 1 and 958830 events in counter 2, which gives an asymmetry of 13.8%, a 0.5% difference to the real asymmetry. This difference increases for larger count rates, however it decreases for smaller real asymmetries.

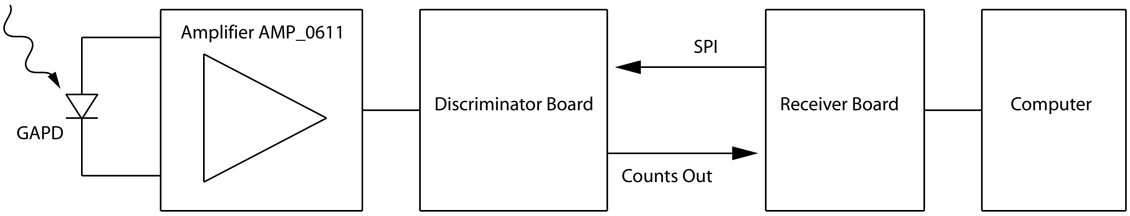

Figure 13: Signal processing chain. The pulses from the GAPD are amplified and then pulse-height discriminated. The treshold can be set via a SPI-interface. The signals are counted with a standard National Instruments counter card in a computer.

3.8 Design of Vacuum Parts

As mentioned above, there is little space to mount the detector, because the x-ray monochromator is located 15 cm below the tube for the Mott detector. On the other hand, the tube has a length of 233.5 mm, measured from the exit aperture of the analyser to the CF100 flange of the tube. Therefore, the detector cannot be mounted in one piece, but the final assembly must be done directly at the tube. An image of the Mott detector is shown in figure 14, technical drawings can be found in the appendix. The feedthrough for the high voltage is in principle specified for 30 kV, but as the atmosphere in the laboratory is controlled and additional insulation is added, it also works at 40 kV. The feedthrough has been placed into a cylinder which is welded on a CF100 flange such that the feedthrough is basically in the UHV tube, i.e. the feedthrough does not protrude below the CF100 flange.

The detector itself is mounted on a CF100 flange. It is standing on three rods which are made of molybdenum, which has the lowest thermal expansion of all standard non-magnetic UHV compatible metals ($4.8 \cdot 10^{-6}/\mathrm{K}$). This is important because the quartz glass rods have a thermal expansion of $5.5 \cdot 10^{-7}/\mathrm{K}$. At a length of 10 cm and a bake temperature of 120°C, this introduces a expansion difference of 42.5µm.

The detector core is mounted on a high voltage insulation ceramics made of macor, which is supported by an aluminum carrier. On this carrier, an aluminum cylinder will be installed. On the cylinder the lenses are fixed. The cylinder and the lenses are mounted separately from the CF100 flange and are installed first. Then the detector is inserted. The last step is to mount the cylinder on the aluminum carrier with macor insulation ceramics in between so that the cylinder voltage can be floated.

In the detector core, the glass rods with the scintillators at the front face are installed such as to cover an angular range as discussed in figure 3. A gold foil with a thickness of 90±10 nm on a kapton foil with 30µm thickness is placed in the center.

The glass rods might introduce an asymmetry in the electric field that the electrons experience on the path to the gold foil. Therefore, an additional plate (see fig. 14) has been placed on the detector core to screen the glass rods and to shape the acceleration field.

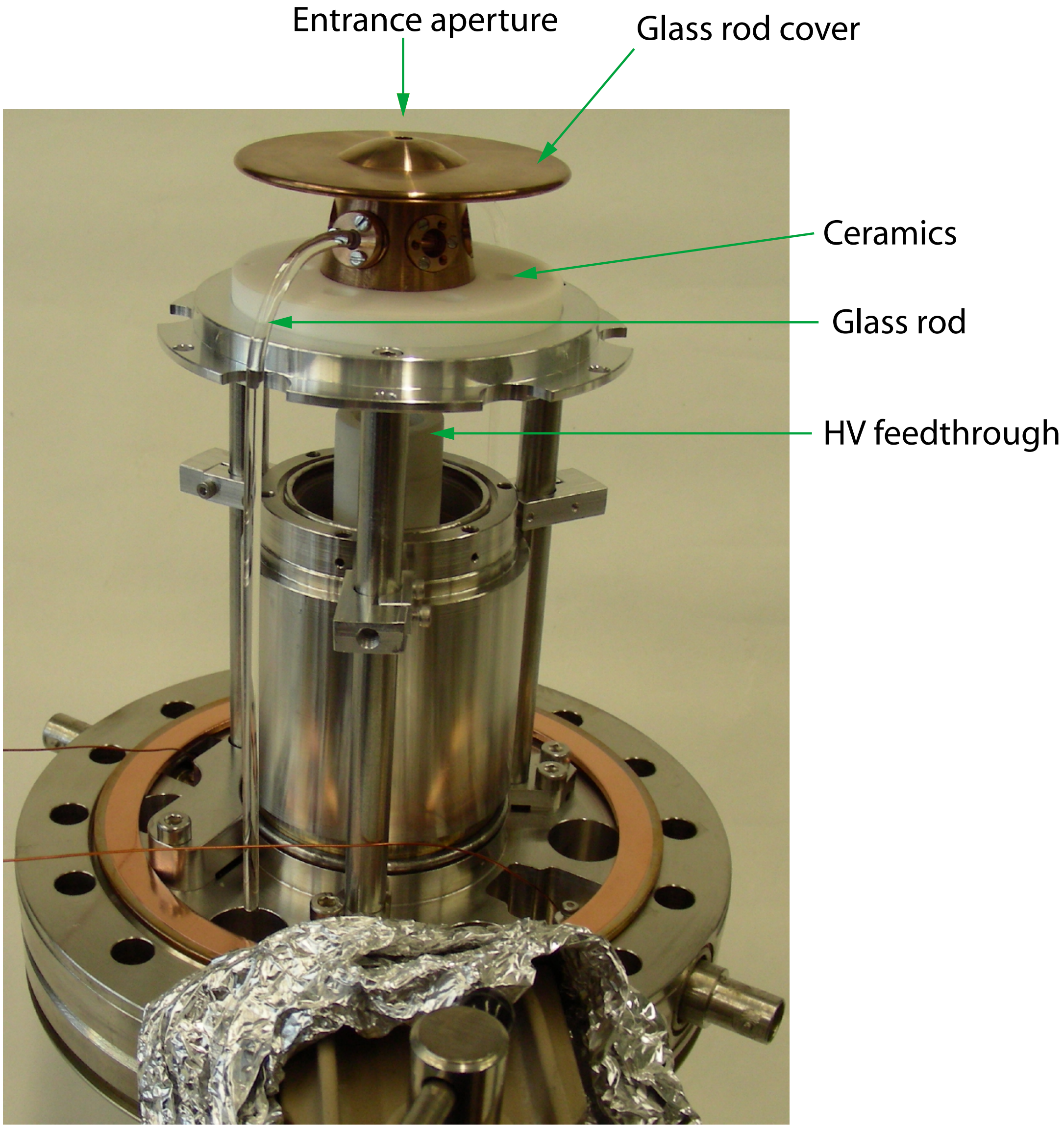

Figure 14: Photo of the Mott detector with two glass rods installed. The lens assembly has been removed so that the detector core is visible.

4 Feasibility Experiments

As explained above, the detection scheme is based on optical detection of electrons with scintillators. Before constructing the detector, the key question to be answered is if it is possible to construct an optical system with a scintillator, a light guide and a photodetector that allows counting of the electrons with sufficient energy resolution to discriminate some part of the inelastic electron spectrum and the photodetector noise. The energy resolution depends on the root of the number of detected photons per electron, $\Delta E \sim \sqrt{N}$. The energy resolution determines how efficiently the inelastic electrons can be discriminated. As a consequence, a good energy resolution is important to achieve a high Sherman function. Therefore, the photon number per pulse that is measured at the photodetector needs to be optimized.

For this purpose, a special test setup has been used which will be described below. The following points were addressed:

- Choice of scintillator
- Material of light guide, transmission losses due to bending, losses at the feedthroughs
- Interface light guide-photodetector
- Coating of scintillator

The measurement setup needs to be able to count individual events, i.e. light pulses, and to perform photon number analysis per event. There are basically two possibilities to measure the photon number. Either the pulse height after the photodetector is measured or the total charge that is transported in the photodetector. A histogram of either pulse height or charge shows the distribution of the number of photons per event. It is rather difficult to measure the pulse height for each event accurately. An easier approach is to measure the count rate while varying the discrimination threshold. This is demonstrated in chapter 4.4. However, the charge histogram method offers higher accuracy, better control of the experiment and an easier data interpretation - at the price of a more involved setup, which will be described in the next section.

4.1 Technical Description:

4.1.1 Experimental Chamber

The experiments have been performed in two setups: One in a light-tight box made of PVC and an UHV chamber with a base pressure of $2 \cdot 10^{-9}$mbar. The UHV chamber was used for experiments involving high voltage and other tests which could not be carried out in the box, e.g. the development of the feedthroughs or the tests of the plastic scintillator. The PVC box has a port for a photomultiplier which is located outside of the box in a light-tight aluminum tube and looks into the box.

The experiments are performed on a CF100 flange which is shown in figure 14. On the flange, the high voltage feedthrough is welded and on the CF16 flanges, feedthroughs for light guides can be installed. A light-tight cover is mounted, which also carries the photomultiplier tube assembly. The photomultiplier is elastically supported with a spring for optimal contact to the light guide. No grease was used for the optical connection. It does increase the light transmission, as once determined, but the grease is not bakeable. If it is not totally removed from the light guides before a bake, it might become hard or even intransparent, therefore we refrained from applying it.

In the course of the experiments, we have used two photomultipliers, a Burle S83062E and a Hamamatsu R7400U. If not otherwise mentioned, the data has been measured with the Burle.

Opposite of the CF100 with the scintillator, a field emission electron gun was mounted.

For experiments with X-rays, a source with variable photon energy by QSA Global GmbH was used. A primary Americium 241 source excites Kα-radiation from Cu (8.04 keV), Rb (13.37 keV), Mo (17.44 keV), Ag (22,1 keV), Ba (32.06 keV), Tb (44.23 keV).

4.1.2 Signal Electronics

Here we describe the pulse counting and pulse integration setup mentioned above. A sketch of the signal processing is shown in figure 4.1.2. The signal from the PMT is first fed into a fast LeCroy 612A amplifier with a fixed gain of 10x. At the amplifier, the signal is tapped twice. One part is used at a LeCroy 623B discriminator, where all pulses with sufficient height are converted into a digital NIM pulse with adjustable width, which is used as a gate signal. This signal starts a LeCroy 2249A Charge ADC which integrates a signal over a period which can be defined by the gate signal. Now the second part of the signal has to be delayed such that it falls into the time window defined by the gate signal. Then the charge ADC signal corresponds to the integral of the pulse. This method is very useful for determining photon numbers per pulse, but it is too slow for use in the Mott detector since the ADC has a dead time of several µs.

For monitoring purposes, a counter has been added which uses the digital pulses from the discriminator.

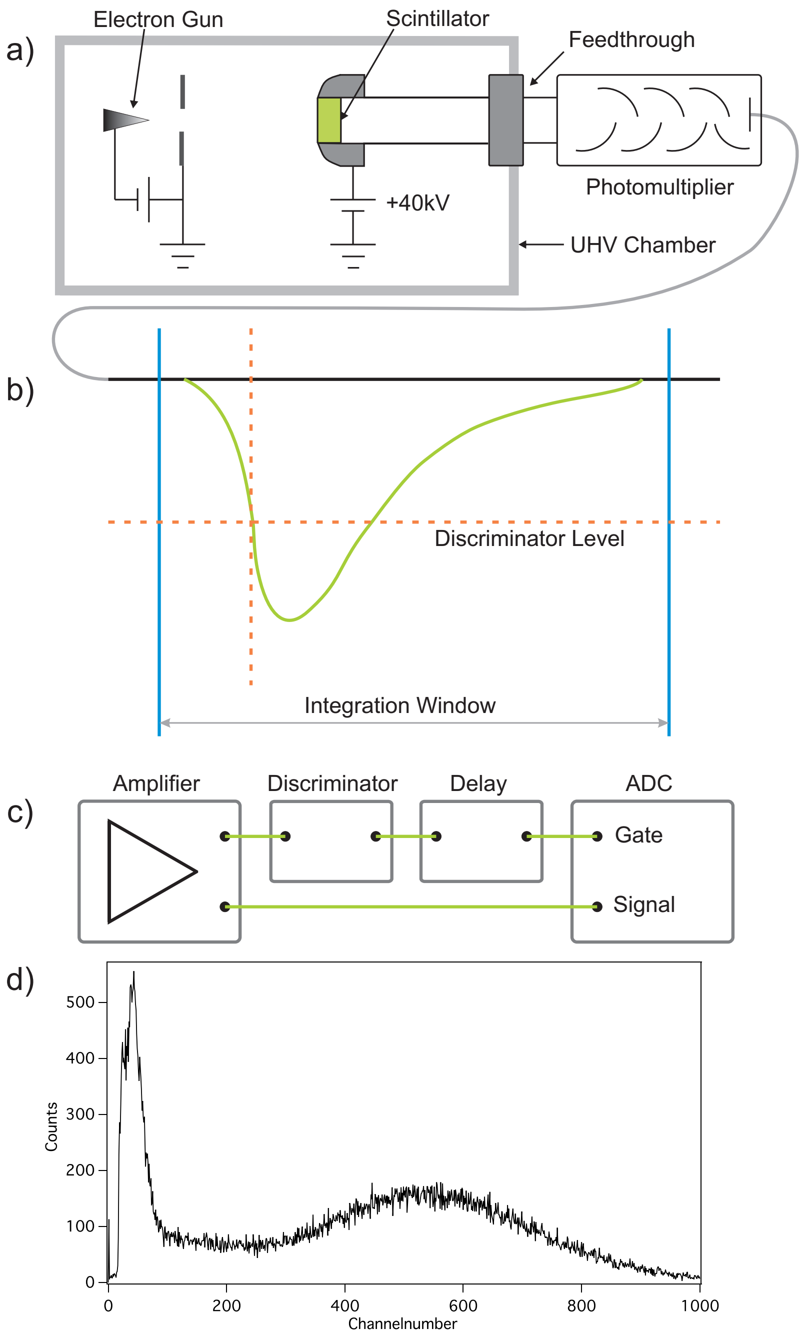

Figure 15: (a) Sketch of the experimental setup. Electrons coming from a field emission electron gun are accelerated by a high voltage on a scintillator that produces a light pulse. The photons are transported in a glass rod to a photomultiplier outside of the vacuum chamber. The photomultiplier converts the light pulse into an electric pulse, shown in (b). All signals coming from the photomultiplier that exceed a predefined discrimination level are integrated over a certain time window with a charge sensitive ADC. The signal processing chain is shown in (c). The discriminator signal is used to properly define the integration window. After measuring thousands of events, a histogram of all integrals is generated, see (d). The histogram is shown as a function of an arbitraty channelnumber of the ADC. Two peaks are discernible, a broad one corresponding to the light pulses from the scintillator and a second peak caused by single photons.

4.2 Choice of Scintillator

As mentioned above, we focused on two scintillators: Yttrium Aluminum Perovskite (YAP) and the plastic scintillator BC490. Short experiments with phosphor powders from Phosphor Technology Ltd, England (we used BK58/N-S1 and QM58/N-S1) were unsuccessful. Probably the light transport through polycrystalline films to the light guide is too inefficient for our purpose.

All data were measured with the system described in chapter 4.1.2. For YAP, many data could be measured in a light-tight PVC box, with the X-ray source with variable photon energy mentioned above. This approach unfortunately does not work with plastic scintillators, because the absorption length for X-rays in plastic is too long. Therefore, all experiments for plastic scintillators were carried out in the UHV chamber.

How many detected photons per electron can be expected in such an experiment? A simple estimation shows the following. At 40 keV, an electron creates about 400 photons in YAP. If we assume that the scintillation light is emitted isotropically, then half of them are emitted in the wrong direction. For YAP, there are losses at the interface scintillator-light guide, since there is an air or vacuum gap. The feedthrough causes an additional loss which can only roughly be estimated. For the test experiments, a teflon feedthrough has been used, with a contact length of 2 mm. The glass rod diameter for the test experiments was 5mm. At the interface glass rod - photodetector there is once again an air gap. Finally, only a fraction of the photons that enter the photodetector is measured, depending on the quantum efficiency of the photocathode. YAP has its emission maximum at 370 nm. At this wavelength, the Burle photomultiplier has a quantum efficiency of 32%, i.e. only a third of all photons is detected. If we assume a transmission of 50% in the feedthrough, we can estimate a number of $\approx$70 photons that should be observed.

The photon number has been measured by integrating the charge over a well defined time window, as explained above. A typical result is shown in figure 4.1.2(d) , where a histogram of the charge distribution of thousands of events is displayed. There are two peaks visible, a single photon peak and the peak due to the signal from the scintillator. The x-axis of the histogram is first of all an arbitrary channel number of the ADC. By calibrating the single photon peak, the x-axis can be expressed in terms of photon numbers.

The most important results are summarized in figure 16, where the measured photon number of both YAP and the plastic scintillator are plotted against the excitation energy. For YAP, both x-rays and electrons were used as excitation source. The data were fitted with a line going through zero. For technical reasons explained below, it was not possible to excite YAP with electrons with a higher energy than 30 keV.

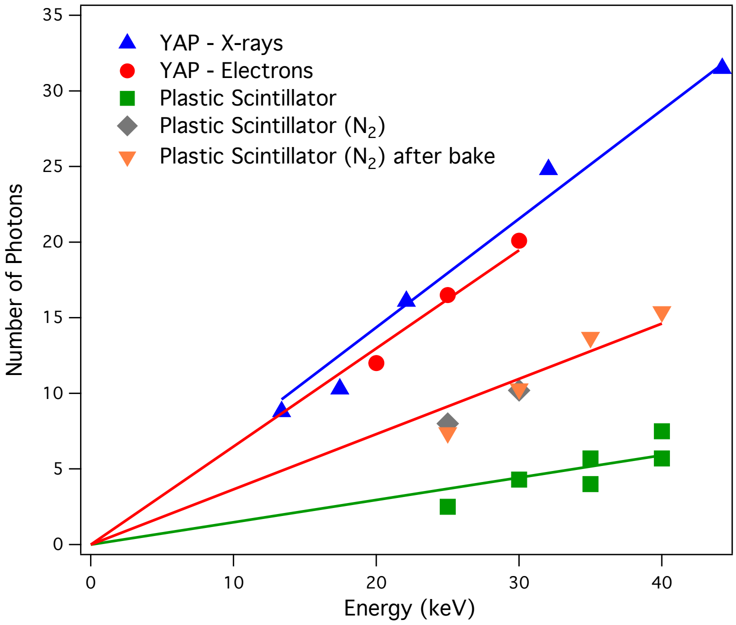

Figure 16: Light Yield of YAP and the plastic scintillator BC490 after a light guide made of quartz glass and a teflon based vacuum feedthrough as a function of the excitation energy. The curve for YAP has been measured for Xray- and electron-excitation. The results agree very well. The plastic scintillator has once been prepared in normal laboratory condidtions and once in a N_2-atmosphere in a glove box. The latter preparation is shown before and after a bake-out of the vacuum chamber. The absorption length for X-rays in plastic scintillators is too long for our case, therefore only electron excitation could be used. The light yield is lower than for YAP, but when the scintillator is prepared in N_2-atmosphere, the light yield is more than doubled, and a value of 50% of YAP is achieved. The bake-out does not decrease the performance of the scintillator.

It is evident that the data for X-ray- and electron excitation agree very well, i.e. the photon number does not depend on the different penetration depth or on the primary excitation step in the scintillator. The photon number for YAP is roughly 50% lower than expected. There are several uncertainties in the measurement setup that might explain the discrepancy, e.g. the transmission of the feedthrough, the transmission of the glass rods, the loss at the interfaces etc.

The plastic scintillator has a much lower photon yield than YAP. One explanation is that for this experiment, the plastic scintillator has been prepared in normal conditions, not in an oxygen-free atmosphere which is recommended by the manufacturer, as mentioned above.

In a later experiment it was found that the preparation in a nitrogen atmosphere doubles the light yield.

An important criterion is the temperature stability of the scintillator. It has to support a bake of the UHV chamber to 120°C over several days. While YAP can easily withstand such conditions, it was not clear for the plastic scintillator. After such a bake, no degradation in the photon number was found.

As mentioned above, half of the photons are lost because they are emitted into the halfspace opposite of the glass rod. If a part of these photons could be used, the energy resolution would improve. Therefore, it was tried to coat the plastic scintillator with a thin silver film. Silver was used because of its high reflectivity at 420 nm and because it can be applied with a standard evaporator. A thin film has two contrary effects: On one hand, it reflects the photons back into the scintillator and then into the glass rod. On the other hand, the primary electrons lose energy in the film and produce less photons in the scintillator.

The silver was evaporated on the scintillator during a photon counting measurement, i.e. the change in photon number could be directly observed. However, no increase in photon number was found.

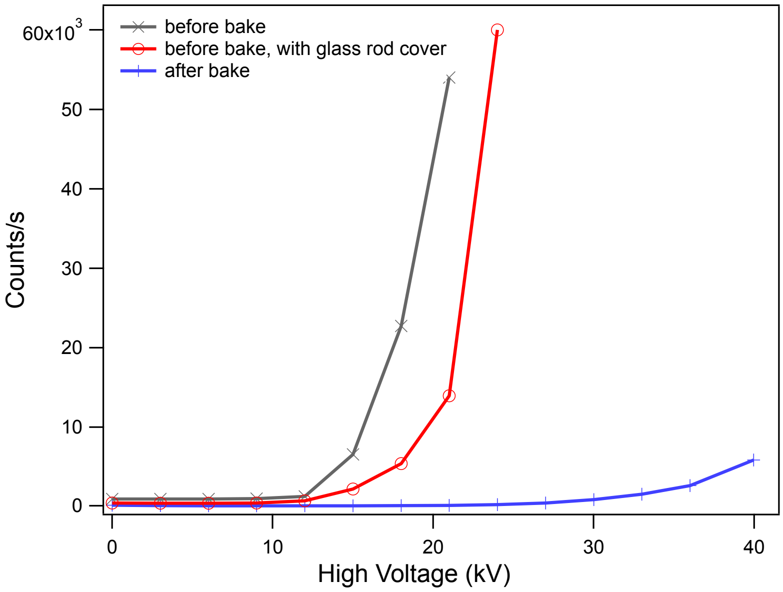

Figure 17: Increase of single photon counts with increasing acceleration voltage. The HV is directly connected to one end face of the glass rod, where the scintillator is placed. Starting from 10 kV, a steep increase in single photon counts is observed. The behaviour does not change when the glass rod is hidden in a metal tube, i.e. stray electrons that hit the glass rod are not responsible for the increase. After a bake of the UHV chamber, the increase is still present, but to a much weaker extent. It is now possible without problems to go to the maximum voltage of 40 kV. Probably adsorbates on the glass rod surface are responsible for the luminescence.

A surprising observation was made when measuring with electrons instead of X-rays, i.e. when high voltage was applied to the scintillator and the front part of the scintillator. Starting from ≈15 kV, a steep increase in the single photon count rate was found. This is shown in figure 17. The increase was so severe that no meaningful photon number measurements could be made above 30 kV for scintillator pulses.

A first suspicion was that field emitted electrons may hit the glass rod and create luminescence in the glass rod, because quartz glass is known to exhibit luminescence in the visible light region [23]. Therefore, a steel tube was placed as a cover around the glass rod. However, no significant difference was found.

However, after baking the UHV chamber with the uncovered glass rod at 120°C for two days, a clear improvement was observed. Most probably, adsorbates on the surface of the quartz rod are responsible for the increase in single photons. A small current on the surface of the otherwise insulating glass rod may excite the adsorbates to generate light. However, almost no current was measured at the high voltage supply, i.e. the current is in the order of the measurement sensitivity of the supply (≈ 100nA).

After baking, the increase in single photon counts is only around 7000 counts/s at 40 kV. This value is negligible, it can be easily discriminated.

4.3 Light Guide and Interfaces

We evaluated two materials, quartz and pyrex. It turned out that for our purpose, pyrex is by far not good enough, there are too many defects that decrease the transmission. A simple optical inspection shows that even for a well-polished, straight rod with a length of 20 cm, it is not possible to look through the glass rod. This is easily possible for quartz. We used HSQ 300 by Heraeus Quarzglas GmbH, obtained at WISAG AG, Zürich. The glass rods were polished by Hellma Optik, Germany.

When using YAP, the crystal was mechanically pressed on the glass rod, no contact substance was used, because in UHV the standard optical grease must not be used. Instead, optical epoxy-glue can be used, but then the crystal cannot be removed again.

The other end face of the glass rod is in air, so in principle it would be possible to use optical glue. However, the UHV chamber has to be baked several times per year. If the grease is not fully removed before baking, it might harden and become difficult to remove after the bake. Therefore, it was not used so far. However, it might be useful to increase the photon number if at some point it turns out to be necessary.

4.4 Pulse Height vs. Discriminator Level Spectra

In the results mentioned above, the integral of a pulse from the photodetector has been measured. However, in a real Mott detector, it is not possible to use this method because the dead time of the ADC is too long. Even with faster ADCs the speed of the detector would be limited by the length of the integration window which must be longer than the full pulse length, i.e. not only the 1/e -length. Therefore, we restrict the measurement to discrimination by pulse height instead of by the integral. This is far easier and the standard method for Mott detectors.

In principle, this method even allows to reconstruct the information given by the histogram of the charge integral. This is shown in figure 18. In the upper panel, a standard histogram is shown, where the single photon peak and the scintillator peak are clearly visible. In the lower panel, a counting experiment is shown as a function of the discrimination level. When the discrimination level is decreased, the count rate increases, as shown in the gray curve. However, it does not increase linearly, but according to the histogram in the upper panel. The maximum increase, i.e. the steepest slope of the gray curve, must be at the maximum of the histogram peak. Therefore, by differentiating the count number, the histogram can be reconstructed. This is shown in the blue curve in the lower panel. Clearly, the resolution is worse than with the histogram method, but the scintillator peak can be resolved.

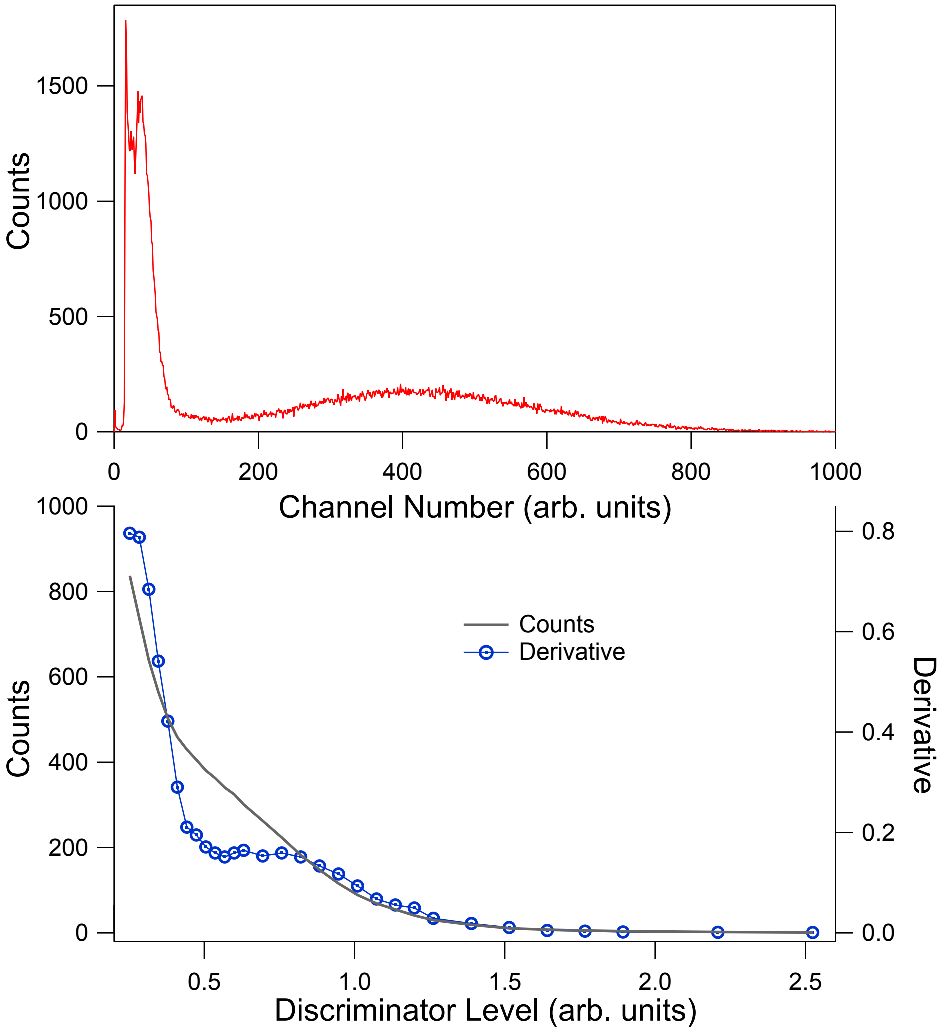

Figure 18: Two different methods of measuring photon numbers: In the upper pannel, a charge sensitive ADC measures the integral of a pulse from a photodetector. The histogram over thousands of events is displayed. Two peaks are discernible, a broad peak caused by events in the scintillator, and a single photon peak. In the lower panel, only the count rate is measured, while varying the discrimination threshold. The derivative is to some extent equivalent to the histogram in the upper panel. Here only the scintillation peak can be resolved. The resolution and the separation from noise is clearly worse, but the method is far simpler.

5 Performance experiments with Mott detector

5.1 Focus Tests

For reliable operation, a stable focus point of the electrons on the gold foil is an essential requirement. The focus should be independent of the electron beam entrance position, the shape of the beam and the intensity, because these parameters might change during an experiment and thereby introduce artificial asymmetries. Conventional Mott detectors are inherently more stable against such fluctuations because the electrons are accelerated as soon as they enter the detector, and they are measured at the acceleration potential. In retarding type Mott detectors, the electrons are decelerated after scattering and measured close to ground potential. Therefore, the electron optics of retarding type detectors is more demanding. Petrov et al. conducted a comparative study of classical and retarding type detectors [24]. In the experiment, the beam entrance parameters were changed. Indeed, the classical detector turned out to be much more stable.

A good discussion of instrumental asymmetries, including the effect of misaligned primary beams, is given in Kessler [5].

For our detector, a different experiment was designed to test the focus stability. We observed the focus of the electron beam directly and could then study the influence of different parameters, like the primary energy, the lens settings etc. This is achieved by replacing the gold foil with a phosphor-target made of ZnS. The electron beam therefore creates a light spot at the focus position, which can be photographed. From the pictures, the focus position, size and intensity can be determined.

The experimental setup is shown in figure 5.1. As mentioned, the gold foil is replaced by a scintillating target. The electron gun is not pointed at the detector entrance directly, instead it is aiming at a nickel yoke sample which is mounted on a rotary arm. The sample is similar to the the one described in figure 33. It can be magnetized with the coil around one side of the yoke. Additionally, the surface can be held on a certain potential against ground. This allows to use the surface as an electrostatic mirror. Therefore, the electrons from the gun can be either scattered at the surface or they can be reflected before they reach the surface. Later, the electrons reach the detector entrance aperture which has a diameter of 7mm. Then they are accelerated on the scintillating target. The focus is then photographed through a CF100 window facing the aperture and target.

The pictures were taken with a video camera (JVC GR 2000), which has the advantage of having simultaneous live video images and a large magnification objective. The drawback is a poor resolution of the CCD chip (640x480 pixel). The camera was read out with IGOR Pro.

The following issues were addressed in the focus tests:

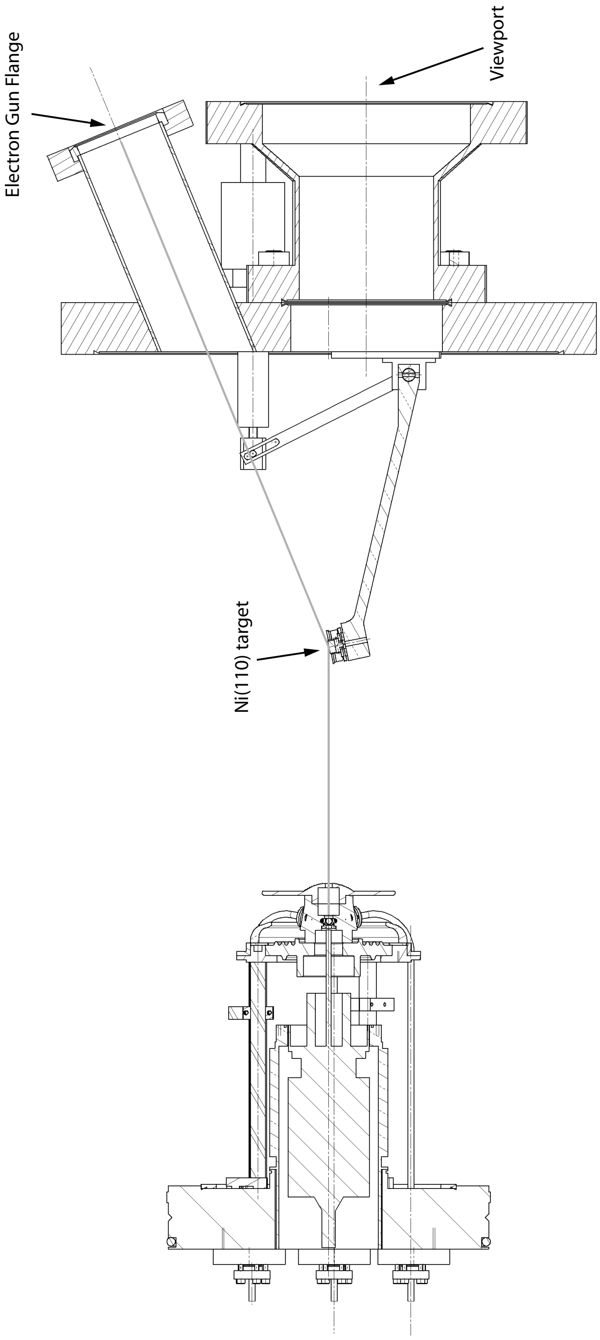

Figure 19: Setup for the focus tests. Instead of the gold foil, a scintillating target is mounted in the detector. The excitation source is an electron gun. The electrons are either deflected or scattered at a Ni(110) sample before entering the detector, depending on a bias voltage which can be applied to the sample. The nickel crystal is mounted on a rotation arm that is used to adjust the position. A CF100 viewport allows to observe the scintillation target. The setup is enclosed in a µ-metal tube (not shown).

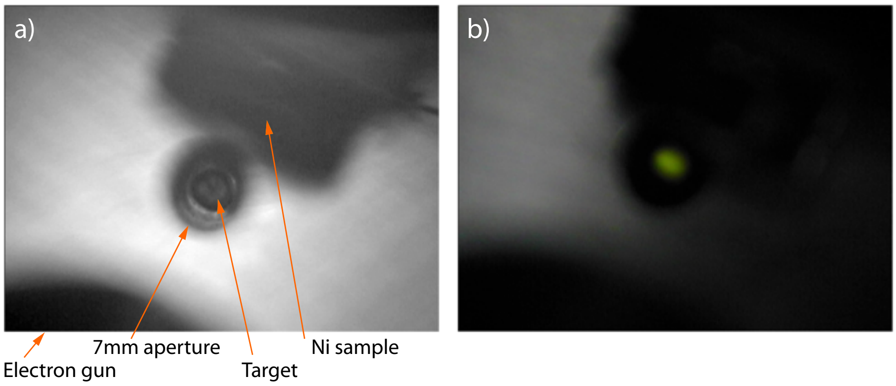

Figure 20: (a) Image of the nickel sample that was used as an electrostatic mirror, the entrance aperture and the scintillating target. (b) The same view, now with applied high voltage and electron irradiation on the scintillating target. The focus is not optimized yet, a broad green spot is visible.

- Stability against changes in the acceleration voltage
- Stability against changes in the lens voltage
- Behaviour upon changes in the electrostatic mirror voltage, i.e. changes in the electron entrance position.

Pictures of the experiments are shown in figures 21 and 20.
In figure 20(a), an image of the entrance aperture without wires is shown. Here, the scintillating target is also visible, as well as the nickel sample and a small part of the electron gun. In image 20(b), the external illumination is decreased and the electron gun and the high voltage are switched on. A green spot appears on the scintillating target. This spot can now be optimized on-line and analyzed by taking pictures and then making spot-profiles or fitting gauss curves. The parameters that were optimized before the real experiment (and then left constant) are the focus voltage, the anode voltage and the X-Y-deflection voltages of the electron gun.
In figure 21, another photo of the entrance aperture to the detector is shown. Two wires have been added in a cross-shape to give a reference point on the scintillating target. This setup has been used for the experiments presented below.
The images have been analysed in pixels. 1mm corresponds to 20 pixels.
During the experiment, the focus size and position was measured as a function of the acceleration voltage in the Mott, as a function of the lens voltage and as a function of the mirror voltage. The results are shown in figure 22-5.1.2.
All experiments have been carried out with a kinetic energy of 5 eV of the electron gun. The lens voltage always refers to the lens element at the Mott entrance. The voltage at

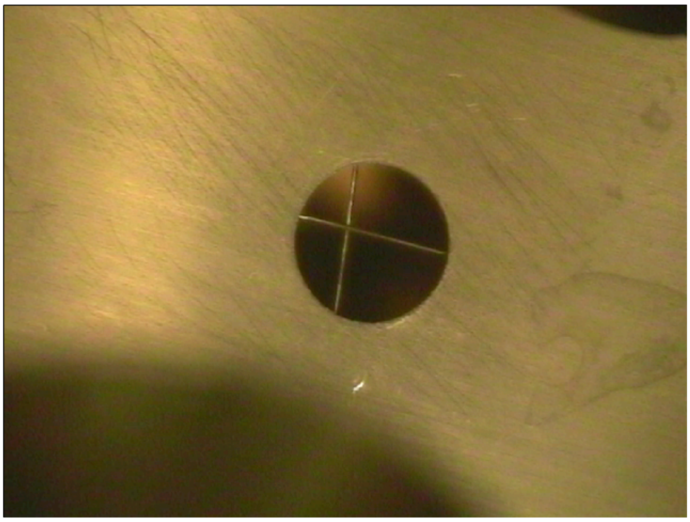

Figure 21: Image of the entrance aperture (diameter 7mm) for the focus tests. A wire cross has been added to give a reference point. The wires have a diameter of 0.25 mm.

the second element is divided down by a resistor network and amounts to $\sim \frac{1}{7}$ of the voltage at the first element.

5.1.1 Effect of Lens Voltage:

The lens has been designed to operate at voltages between 0 and 2 kV. Ideally, the lens should focus/defocus the beam, but it should not change its position on the target. A moderate change in the focus size probably does not introduce an instrumental asymmetry, but a position shift very likely does so. The results are shown in figure 22. The datapoints have been recorded starting from 0V to 400V in steps of 50V and then to 1700V in steps of 100V. The arrow indicates the direction of increasing lens voltage. The two black crosses indicate the center position before and after the experiment. Clearly, the spot does not stay fixed, but it moves on the scintillating target.

5.1.2 Effect of High Voltage:

Here we expect a similar behaviour of the spot size as above. For higher voltages, the spot should become sharper, but it should not move. This was measured for five different lens voltages (0V, 400V, 800V, 1200V and 1600V) and for a high voltage between 10 and 30 kV. The results are shown in figures 23 and 5.1.2.

As visible in figure 23, the spot moves with high voltage as well, the focus point walks along a line. The behaviour is similar all the lens voltages, but the focus point is slightly shifted, as expected from the discussion above.

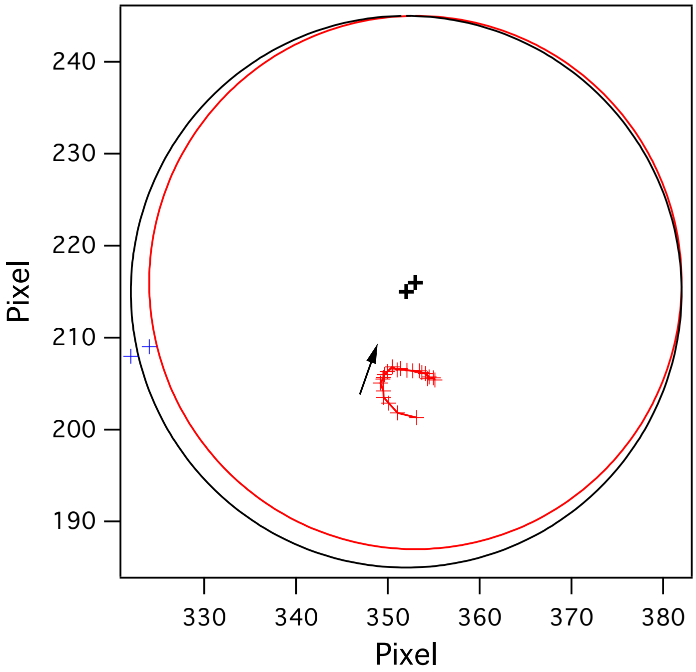

Figure 22: Focus position as a function of lens voltage. The focus position moves with increasing lens voltage. The direction of movement is indicated with an arrow. 1mm corresponds to 20 pixels. The two black crosses indicate the center of the target before and after the experiment, the two blue crosses the wire cross position. The black and red circle represent the scintillating target area.

As expected, the width of the focus point decreases with increasing high voltage (fig. 5.1.2 (a)), and the integral increases because the spot becomes much brighter (fig. 5.1.2(b)).

5.1.3 Effect of the Electrostatic Mirror:

Here the spot size and position has been measured as a function of the voltage on the electrostatic mirror voltage. In contrast to the previous focus experiments, it is expected that the focus point moves on the target. To understand the data presented in this chapter it is important to emphasize that the wire cross at the entrance aperture has been used (fig.21). During the experiment the focus crosses one of the wires, therefore two spots are visible and are recorded separately for a certain voltage range.

In figure 25, the position of the focus point is measured for five different lens voltages. For each lens voltage there are two curves, where each curve represents the spot on one side of the wire. The mirror voltage was varied between 0 and 9V in steps of 0.5V.

In figure 26, the spot integral for the same data is shown.

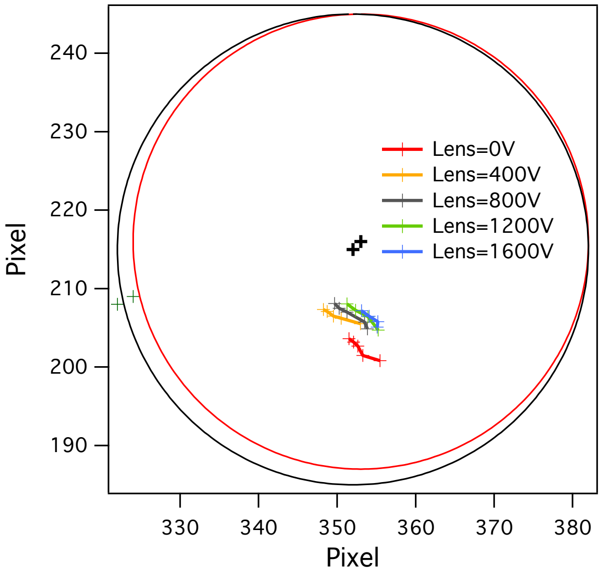

Figure 23: Focus position as a function of acceleration voltage (10-30 kV), for five different lens voltages. The focus position is not constant, but changes with the acceleration voltage.

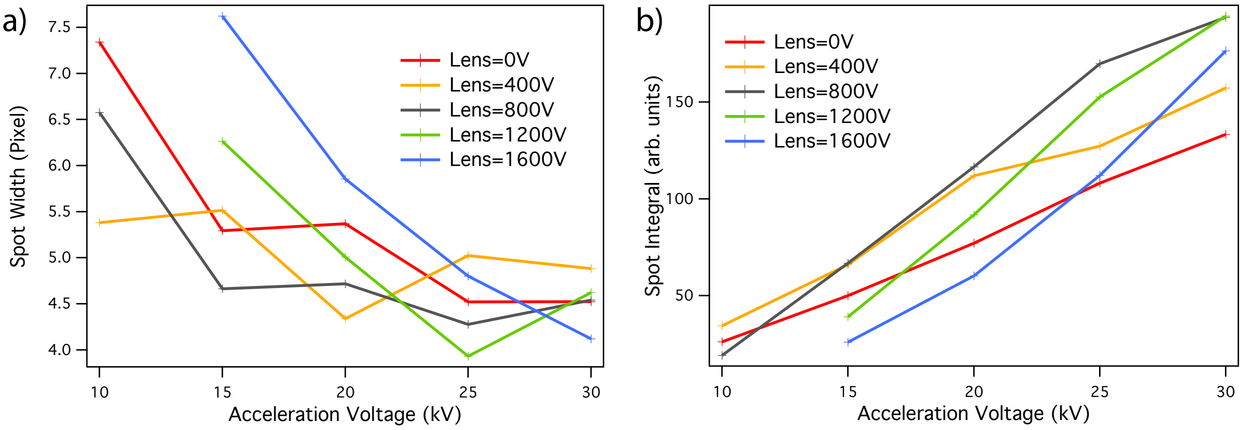

Figure 24: (a) Spot width as a function of the acceleration voltage, for five different lens voltages. The spot size clearly decreases for increased high voltage, as expected. (b) Spot Integral as a function of the acceleration voltage, for five different lens voltages. Despite the decreasing width, the integral increases due to the increasing intensity.

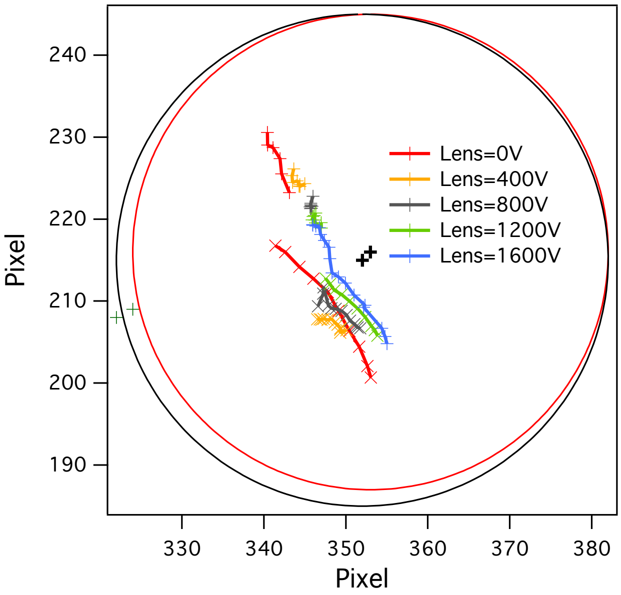

Figure 25: Focus position as a function of the electrostatic mirror voltage, for five different lens voltages. During a mirror voltage scan, the spot moves over one wire on the aperture, therefore two spot positions are shown.

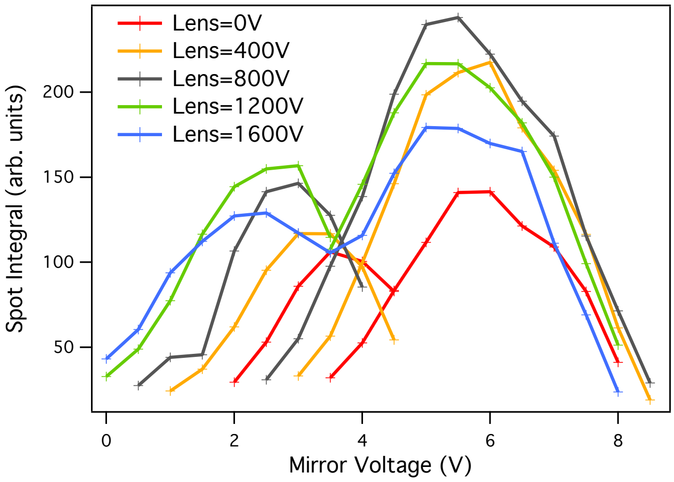

Figure 26: Spot integral as a function of the electrostatic mirror voltage, for five different lens voltages.

5.2 Operation and Stability of the Photon Detection Setup

For the first tests with the Mott detector, only two scintillators were mounted. The goal was to test the performance of the electronics, the efficiency of the light transport and detection system, the stability of the system and to detect teething problems. The present setup is capable of measuring asymmetries, i.e. in principle we can determine the spin polarization in one direction. In the following, we will show results that were measured with the electronics discussed above and a Labview program that controls the discriminators and reads out the counters.

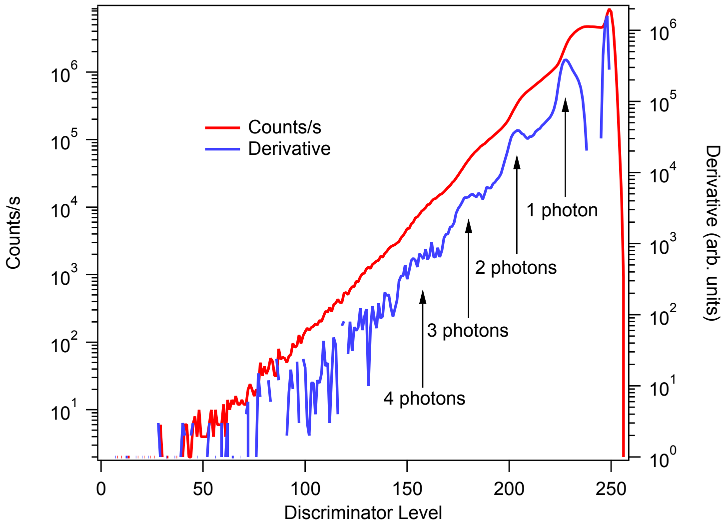

Figure 27: Discriminator Level spectrum, analogous to figure 18. The discriminator level is displayed as a 8bit number which is the resolution of our discriminator. Here, a level of 255 corresponds to a threshold at the baseline, i.e. the threshold is in the noise. A level of 0 corresponds to a threshold of ≈100mV. The red curve shows the count rate that increases when the discriminator level approaches the baseline. The blue curve gives the derivative, which can be understood as mentioned in section 4.4. In both spectra, clear steps or peaks are observable. They can be assigned to the one-photon signal, two photon etc. These spectra allow a simple calibration of the energy axis in terms of photon numbers. Here, only dark counts are measured, i.e. the GAPD was not exposed to any light. However, the GAPD intrinsically has a dark count rate of ≈4Mcps.

In figure 27 a typical discriminator spectrum is shown for a GAPD which is not illuminated. These spectra have been discussed in section 4.4 for the example of a photomultiplier. For a GAPD, the principle of measurement is the same, i.e. the count rate is measured as a function of the discrimination level. However, the spectrum for a dark GAPD looks different from a photomultiplier because it is possible to distinguish different photon number peaks, as mentioned above. The different peaks can already be seen in the raw spectrum when it is plotted on a logarithmic scale. The unit of the discrimination level corresponds to the numeric value which is written to the 8bit-potentiometer that supplies the reference threshold. Here a value of 0 corresponds to the highest threshold, while for a value of 255 the threshold is close to the baseline. The shape of the spectrum is a function of the APD supply voltage which defines the internal amplification.

Now we turn on the electron gun and the Mott high voltage and accelerate electrons on the gold foil. In figure 5.2, we show a comparison between the “dark” GAPD spectrum and the spectrum under excitation with 40 kV electrons. The difference between the two curves is the signal related to light coming from the scintillator. Obviously the two contributions are not separated well enough to distinguish them clearly. For an good Mott detector, the threshold should be set such that the dark count rate is below 10 counts/s but without loosing a significant part of the useful information. For a better separation, the photon number per event that is measured by the GAPD must be improved or the dark count rate minimized. Three immediate problems were identified: The active area of the GAPD does not fully cover the glass rod end face, i.e. a part of the light is lost. A new mounting system has been constructed, but not tested yet. Secondly, the light transport at the interface between GAPD and glass rod can be improved with optical grease due to refractive index matching. Thirdly, there is a new model of the Hamamatsu GAPD with a higher photodetection efficiency (70% vs 50%) which was not available at the time of purchase. Combining these three measured, a much better separation can be expected.

In figure 29, a first asymmetry measurement of two opposite scintillators is shown, albeit with an unpolarized electron beam. The spectrum has been measured roughly 30 minutes after switching on the detector, with an acceleration voltage of 40 kV. The discriminator level has been placed on an arbitrary level, but above the dark count level, i.e. the count rate is zero before switching on the electron gun. A decrease in the count rate of both channels over time is observed. The reason is related to thermal drifts in the APD and is discussed below. Due to this decrease, the asymmetry in the lower panel is not useful as an absolute value, but the curve indicate that the electronics is capable of measuring the count rates and therefore the asymmetry reliably.

How can this decrease be explained? Several reasons are possible, and they are not exclusive. We tested all voltages involved for stability over time. Finally, the most likely explanation stems from figure 30. Here the count rate and the GAPD current are measured simultaneously. In both curves, an exponential decay is observed. The time constants do not match perfectly, but they are comparable. There are two possible reasons for the similar trend: Either a decrease in the dark count rate of the GAPD or a

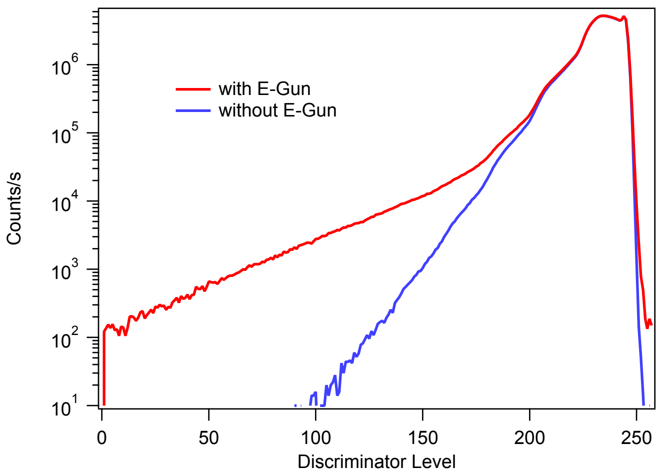

Figure 28: Discriminator spectrum for a GAPD, once with excitation of the scintillator with 40 kV-electrons and once without. The difference between the two curves is the signal we want to measure. The dark counts are not well enough separated from the real signal, i.e. the light transport and photodetection efficiency is too low. Possible reasons are discussed in the text.

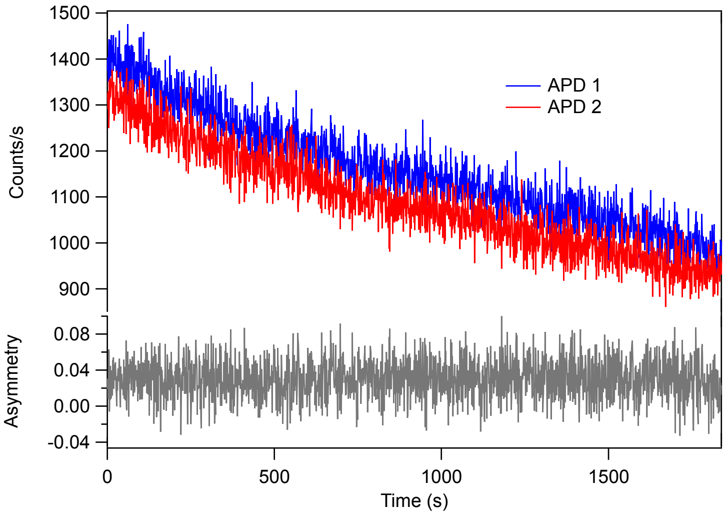

Figure 29: A first asymmetry measurement with two APDs as a function of time. The discriminator level is set to an arbitrary value, however above the noise level, i.e. only real events coming from the scintillator are counted. The excitation energy here was 40 keV. The count rate of both APDs decreases due to thermal effects, as discussed below. The asymmetry is then not useful as an absolute value, but the curve shows that the detector is in principle capable of measuring count rates, and reliable asymmetries can be determined.

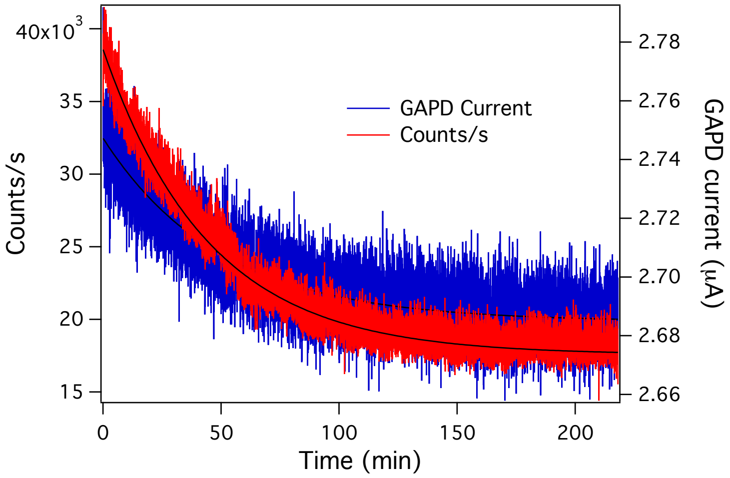

Figure 30: Count rate and GAPD current vs time. The decay time constant is comparable, which suggests a common cause for both curves. As shown in figure 31, the decrease is caused by a warming up of the GAPD which decreases its amplification.

decrease of its amplification. To better understand the trend, we measured discriminator spectra as a function of time. Totally 130 spectra have been acquired where one spectrum takes about two minutes. The result is shown in figure 31. A cut along a constant discriminator level (right panel) , as indicated by the gray arrow, reproduces the count rate curve in figure 30. From these spectra, a simple shift in the discriminator level can be excluded, because then the spectra should shift horizontally. A decrease in the dark count rate or an intensity drift of the electron gun cannot be excluded, but they fail to explain the observed features. The individual photon peaks are not only decreasing in intensity, but also their position in the discriminator spectrum shifts. This must be caused by a decrease in the amplification of the GAPD, which would also explain the decrease in the GAPD current.

The GAPDs are known to have a strong temperature dependence concerning their amplification. Hamamatsu specifies a drift of 10%/°C. Therefore, the GAPDs must be temperature stabilized. Such a thermal stabilization has been constructed for this detector, but it has not been used yet. The GAPDs are mounted on copper plates which are connected to a cooled copper disc which serves as a thermal reservoir. It will be tested in the coming months.

Additionally we tested other potential sources of temporal drifts. In figure 32, the reference voltage for the discriminator is shown for two channels as a function of time. We observe a decrease of ≈0.5 mV over 14 hours, starting after two hours. Furthermore we observed a drift in the APD supply voltage. We do not show curves because this drift is not responsible for the trend observed in figure 30 and we have improved the power

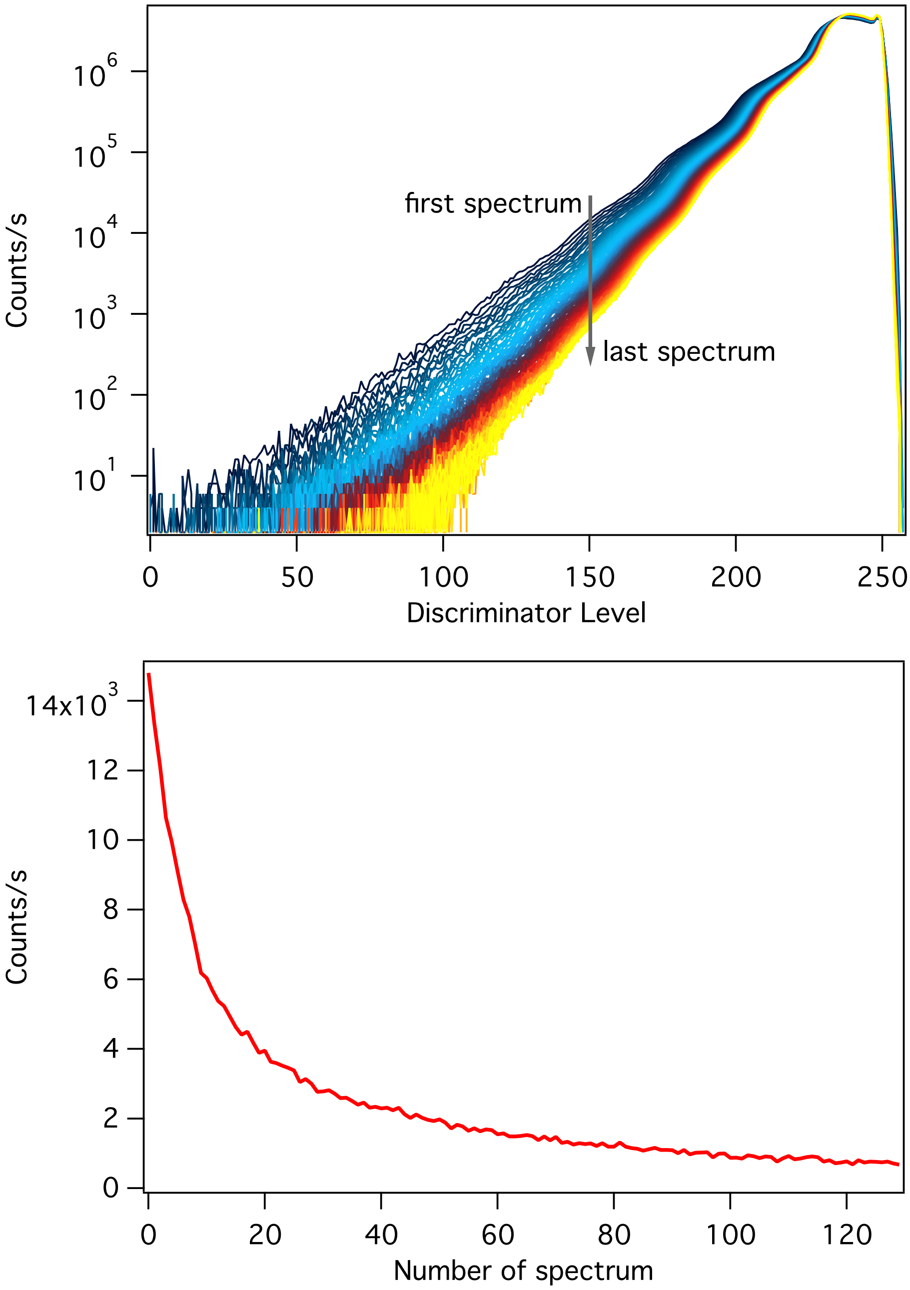

Figure 31: Left panel: Discriminator spectra as a function of time. Totally 130 spectra have been measured, where one spectrum takes 2 minutes. The spectra indicate a decrease in the amplification of the GAPD. Right panel: A cut through the spectra at a constant discriminator level (grey arrow) reproduces the decrease in the count rate shown in figure 30.

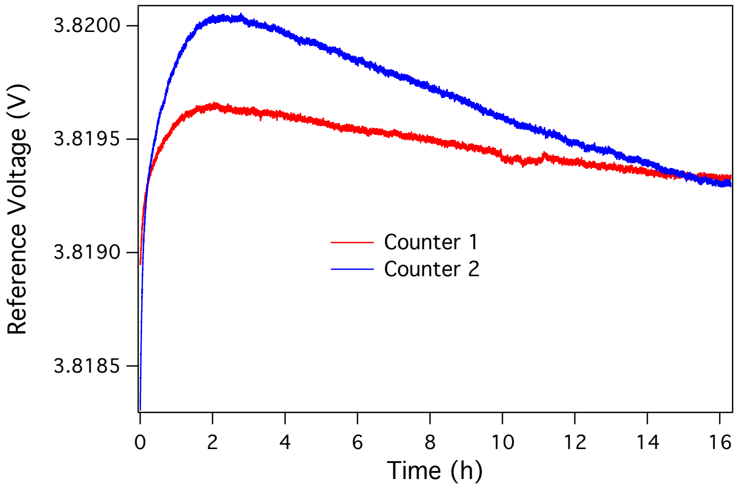

Figure 32: Reference voltage for the discriminator as a function of time. After two hours, the voltage starts to decrease by 0.5mV in 14 hours.

supply.

5.3 Status and Outlook

As mentioned above, the detector has not left the commissioning and test phase yet. The photon number per pulse still needs to be optimized. As discussed above, we will try three different solutions. Results will follow soon.

In the preceding chapter, temporal drift in the detector has been discussed extensively. We have already optimized several components to minimize any changes in voltages. The largest effect stems from the warming up of the GAPD. To avoid this, a temperature stabilization system has been implemented, but not tested yet.

Other temporal drifts can possibly be overcome by simply not switching off the electronics. Then it will warm up initially, but after a certain time a thermal equilibrium should be reached. Of course, this requires a stable room temperature, but this is the case in the ESCA lab where the temperature remains stable within one degree.
]

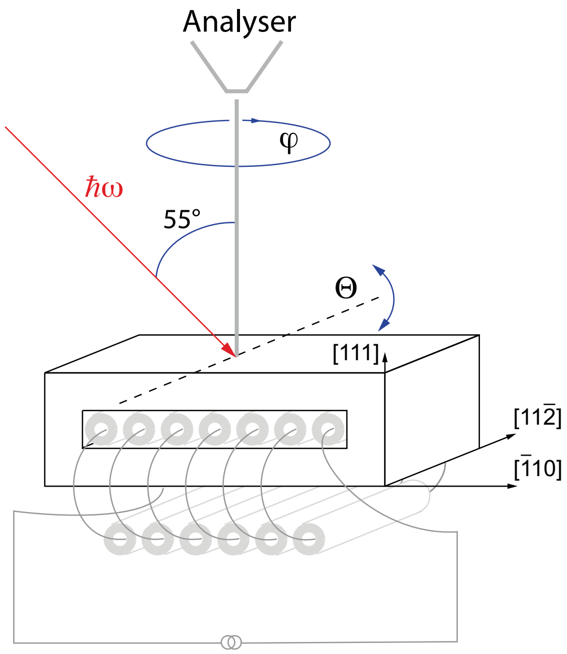

Figure 33: Sketch of a Ni(111) yoke crystal. The crystal can be magnetized with a coil which is wrapped around the lower yoke side. The long side of the yoke is oriented along the [$\bar{1}$10]-direction.

6 Resonant Photoelectron Diffraction of Ni(111)

6.1 Introduction

An important prerequisite for spin-resolved experiments on magnetic surfaces is the ability to magnetize the sample along a defined direction. Additionally, for momentum-resolved measurements the stray field at the surface must be small to avoid electron deflection due to Lorentz forces. An elegant way to circumvent these problems is the use of yoke crystals. A sketch of our sample is shown in figure 33. For nickel, M. Donath has reviewed experiments with yoke crystals with the low-Miller-index surfaces (001), (110) and (111). For the (111) surface he finds that the magnetization coincides with the [$\bar{1}$10]-direction, i.e. the direction of the magnetic flux, if a current is passed through the coil. However, for our crystal, we find that the magnetization is aligned closely to the [$\bar{1}\bar{1}$2]-direction, as described in publication A. The difference in the two crystals can probably be explained by the geometry difference of the two crystals, strain or other factors, as discussed by Donath.

6.2 Experimental

Two methods have been used to magnetize the crystal:

- Magnetization with a current pulser: Here, a capacity of 3 mF, charged with 40V, is short-circuited over the coil of the sample, resulting in a high-current pulse of short duration. The magnetization can be switched simply by changing the polarity of the connecting leads. However, the mutual induction of the nickel core has to be considered, which leads to a smaller effective field pulse with a longer duration.
- Magnetization by continuous current: A DC current is passed through the coil, first 1 A for one minute, then 1.5 A for one minute, finally 2 A for 30 seconds. Afterwards the current is slowly turned off. During this procedure, the crystal warms up, but the temperature stays below the lower measurement limit of a pyrometer (∼ 550 K).

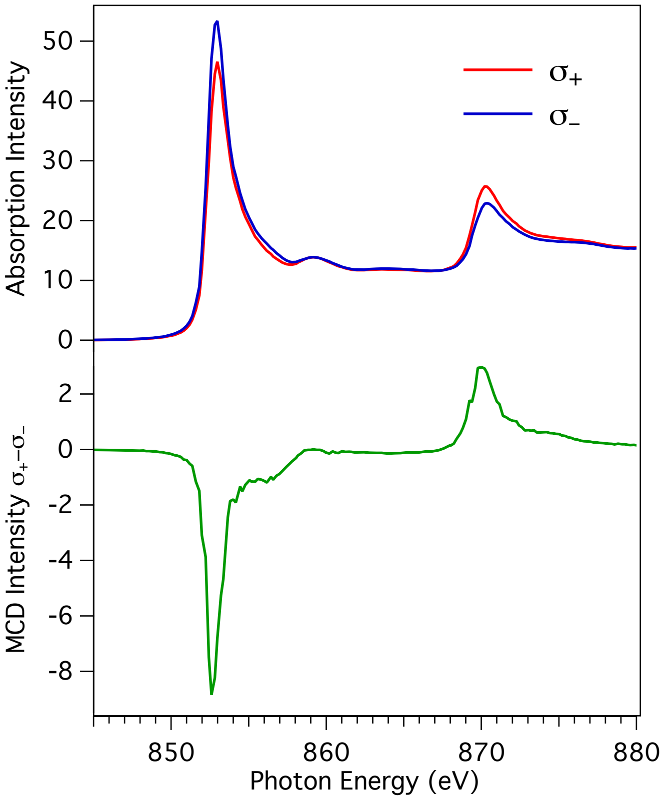

Figure 34: XAS and XMCD spectra at the Ni$L_{2,3}$-edge. From the spectra, the magnetization can be calculated.

All data were measured at the X11MA beamline at the Swiss Light Source (SLS) in an endstation dedicated for x-ray photoelectron spectroscopy (XPS) and angle-resolved x-ray photoelectron diffraction (XPD). The XMCD spectra were recorded in the total-electron-yield (TEY) mode. The spectra have been normalized by dividing by a reference for the photon flux that is measured at a mirror in the beamline path. The undulators of the X11MA beamline offer a precise control of the polarization state of the x-rays. When working with the first harmonic, the degree of polarization is better than 98 % for both linear and circular polarized light. Therefore, it is not necessary to correct for incomplete polarization. The spot size was ≈ 2-3 mm. The base pressure was below $2 \cdot 10^{-10}$ mbar. The substrate was cleaned by repeated cycles of argon sputtering and annealing.

To determine the magnetization, we compare our results, shown in figure 34, to the XMCD data measured by Chen et al. [25]. In their analysis, they first subtract a constant to set the baseline of the absorption spectra to zero. Then they normalize the two spectra such that the sum equals 100 % at the L_3-edge. The difference is then directly the magnetic circular dichroism spectrum. For a completely magnetized sample, they determine a difference of 19 % at the L_3-edge. We use this value as a reference to calculate the magnetization of our sample. Due to our measurement geometry, we have to correct for the angle of incidence since the XMCD intensity is proportional to the scalar product of the magnetization vector and the wave vector of the X-ray beam. Therefore, we have to divide all measured values by a factor of $cos(\theta)cos(\phi)$ where θ and ϕ are the polar and azimuthal angle between the two vectors. Depending on the magnetization method, we obtain the following results:

- Current pulser: We obtain a magnetization of 34 % ± 1.9 %
- DC Current: The scatter is larger than with the former method. On average, the sample is 55 % magnetized, with a standard deviation of 13.2 %. It is possible to magnetize the sample up to 70 %, however it is not clear where the large deviations come from. It might be related to the history of the sample.

6.3 Publication A: Resonant Photoelectron Diffraction with Structural and Magnetic Contrast

Resonant Photoelectron Diffraction with circularly polarized light

Martin Morscher,[1] Frithjof Nolting,[2] Thomas Brugger,[1] and Thomas Greber[1,*]
[1] *Physik-Institut, Universität Zürich, Winterthurerstrasse 190, CH-8057 Zürich, Switzerland*
[2] *Paul Scherrer Institut, CH-5232 Villigen PSI, Switzerland*
(Dated: February 10, 2011)

Resonant angle scanned x-ray photoelectron diffraction (RXPD) allows the determination of the atomic *and* magnetic structure of surfaces and interfaces. For the case of magnetized nickel the resonant L_2 excitation with circularly polarized light yields electrons with a dichroic signature from which the dipolar part may be retrieved. The corresponding L_2MM and L_3MM Auger electrons carry different angular momenta since their source waves rotate the dichroic dipole in the electron emission patterns by distinct angles.

PACS numbers: 79.60.-i, 61.05.js, 75.25.-j, 79.60.Bm
Keywords: Resonant Photoemission, XPD, Dichroism

The quest for atomic scale structure determination at surfaces and interfaces lead to the development of a large number of powerful methods [1]. Among those, x-ray photoelectron spectroscopy (XPS) with angular resolution (XPD) allows structure determination paired with chemical and magnetic sensitivity [2]. The signal is best, when the x-ray absorption coefficient is at maximum. These maxima occur in resonant excitation and have so far been exploited for the probing of defect states in TiO_2 [3], for looking inside an endofullerene [4], or for the investigation of the mixed valence structure of magnetite [5].

In this letter, angle scanned resonant photoelectron diffraction (RXPD) is applied to nickel, the "fruit fly" of resonant photoemission [6–10]. Circularly polarized light is used for the precise measurement of the dipole induced by the x-ray magnetic circular dichroism which is largest at resonance. After this proof of principle we show that the angular momentum of the outgoing electrons can be measured with RXPD. This extends the results of Daimon et al., who demonstrated that forward scattering XPD patterns rotate due to the angular momentum of circularly polarized photons [11–13]. Here, the electron source wave [14, 15] rotates the magnetisation direction in the final state of the emitted electrons. It is also found that Auger electrons may carry angular momenta opposite to that of the exciting photon and larger than ħ.

Circular magnetic dichroism ΔI_{MD} is the difference between the absorption coefficient of right and left circularly polarized light. It is proportional to the scalar product of the magnetization $\mathbf{m}$ and the angular momentum of the incoming photon $\mathbf{L}_{ph}$ [16].

$$\Delta I_{MD} \propto \mathbf{m} \cdot \mathbf{L}_{ph} \tag{1}$$

For right circularly polarized light (σ^+) $\mathbf{L}_{ph}$ is parallel to the propagation direction of the photon, and for left circularly polarized light (σ^-) $\mathbf{L}_{ph}$ is antiparallel. ΔI_{MD} is a dipole, i.e. proportional to $\cos(\vartheta)$, where ϑ is the angle between $\mathbf{m}$ and $\mathbf{L}_{ph}$. From this follows that the absolute orientation of $\mathbf{m}$ is determined from three or more non-coplanar light incidences.

Photoemission yields ΔI_{MD}, under the assumption that the photoemission current is proportional to the x-ray absorption coefficient. This must not hold for partial measurements like in angular resolved photoemission where $dI/d\Omega$ is measured [17]. The different photoelectron source waves of electrons excited with differently polarized light lead to different photoemission final states that comprise information on the magnetism *and* the surrounding of the emitter [18]. Here we show that contributions of the atomic and the magnetic structure can be disentangled with a spin integrated experiment.

The experiments have been performed at the SIM beamline at the Swiss Light Source (SLS) [19] in an endstation dedicated for x-ray photoelectron spectroscopy (XPS) and angle-resolved x-ray photoelectron diffraction (XPD) with a base pressure below $2 \cdot 10^{-10}$ mbar. The x-rays impinge perpendicular to the polar rotation axis with an angle θ_o between the x-rays and the electron energy analyzer of 55° (see Figure 1). The degree of polarization is better than 98%. All measurements are done at room temperature. The Ni(111) yoke crystal [20] was cleaned by repeated cycles of argon sputtering and annealing. It is magnetized by passing a current of 2 A for 30 s through the yoke coil. The resulting magnetization was inferred from an x-ray magnetic circular dichroism (XMCD) spectrum at the Ni L_2,L_3-edges in the total-electron-yield mode. Comparison with corresponding spectra of Chen et al. [21] indicate a magnetization of ∼40%, which is not 100 % due to a multidomain structure.

RXPD experiments on 3d transition metals will make use of the most intense L_3 absorption edges [3, 21]. Here we investigate the L_2 resonance since it provides L_2MM *and* L_3MM emission which allows for direct comparison and consistency checks. Figure 2 shows resonant x-ray photoelectron spectra from magnetized Ni(111) of right and left circularly polarized light. The photon energy is set on the Ni L_2-resonance ($2p_{1/2} \rightarrow 3d$) at $\hbar\omega$ = 870.5 eV. The Fermi level E_F at 870.5 eV elec-

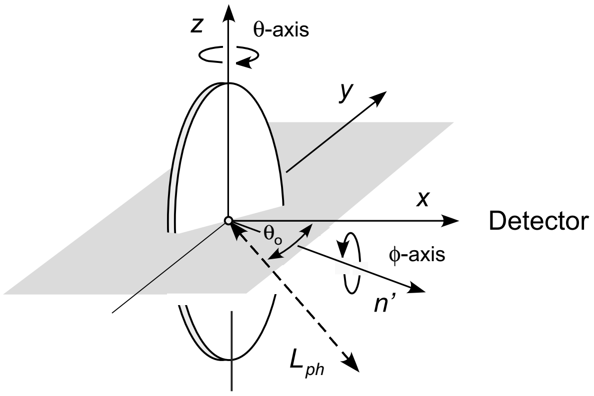

FIG. 1: Geometry of the XPD experiment. The electron detection is parallel to **x** and the polar (θ) rotation axis parallel to **z**. The sample normal $\mathbf{n}'$ is the azimuthal (ϕ) rotation axis and lies with the light incidence along its angular momentum $\mathbf{L}_{ph}$ in the xy plane (shaded area), θ_o =55° away from **x**.

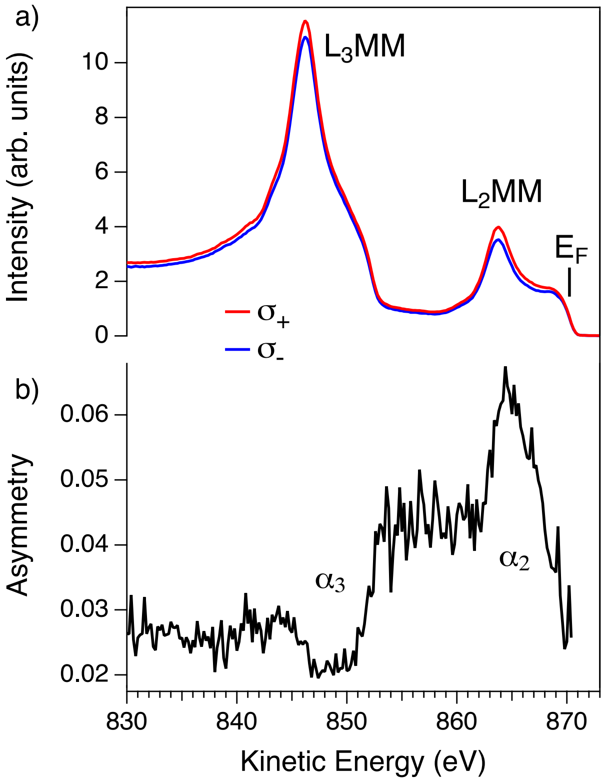

FIG. 2: (Color online) (a) Near normal photoelectron spectra with left and right circularly polarized light with an angle of 30° and 180-30° between $\mathbf{L}_{ph}$ and $\mathbf{m}'$. The photon energy is set on the Ni L$_2$-resonance at $\hbar\omega$ = 870.5 eV. The spectra have been normalized with the photon flux. The Fermi level E_F, the L_2MM and the L_3MM Auger deexcitation peaks are indicated. (b) The asymmetry A between right and left circularly polarized light exhibits two distinct extrema α_2 and α_3, on which we performed XPD measurements.

tron energy, the L_2MM (863.8 eV) 6 eV satellite (see [22] and references therein), and the L_3MM (846.2 eV) Auger deexcitation peak are most prominent. The spectra have been normalized with the photon flux. Figure 2b) demonstrates circular dichroism in these resonantly excited electron emission spectra. The asymmetry $A = (I(\sigma^+) - I(\sigma^-))/(I(\sigma^+) + I(\sigma^-))$ between right and left circularly polarized light exhibits a maximum at α_2 and a minimum at α_3. The asymmetry can be reversed by switching the magnetization or by the rotation of the sample by 180° [23]. Off resonance, at $\hbar\omega = 873.5$ eV the dichroic asymmetry in the L_2MM Auger line is 1.4 ± 0.8 % (data not shown). The extrema α_2 at 848.4 eV and α_3 at 863.6 eV do not exactly coincide with the L_2MM and the L_3MM intensity maxima, which indicates multiplet structure [24]. In the following we use the labels α_i^σ for electrons at the energies of α_2 and α_3, excited with σ^+ and σ^- polarized radiation, respectively.

If we perform on these resonances angle scanned x-ray photoelectron diffraction (RXPD), the experiment yields information on the atomic *and* the magnetic structure. Briefly, the sample frame (x', y', z') is rotated in the lab frame (x, y, z). The photoelectron intensity I is mapped in polar coordinates $(f(\theta), \phi)$, where the polar angle θ and the azimuthal angle ϕ define the sample orientation with respect to the electron detection direction (see Figure 1) [25]. This leads for ΔI_{MD} to a dipolar function $D(\theta, \phi)$ in the XPD map that depends on $\mathbf{L}_{ph}$, the electron detection direction in the lab frame and $\mathbf{m}'(\theta_m, \phi_m, a_m)$ in the sample frame, where the amplitude a_m is a measure for the magnitude of the dichroism [23].

Figure 3a) shows RXPD data for α_2^+. The XPD map is dominated by the information on the atomic structure which corresponds to that of a face centered cubic (fcc) crystal which is cut along the (111) plane [26]. Below the obvious atomic structure dichroic information must be hidden. In order to visualize the dichroism, we form the asymmetry A between the α_2^+ and the α_2^- XPD scans (see Figure 3b). These data contain information on the dipolar (magnetic) nature of dichroism and higher order multipoles, which are related to differences in the diffraction patterns due to different source waves [11, 27]. The dipolar part has the symmetry $A(\theta, \phi) = -A(\theta, \phi{+}180°)$, as it is expected for in plane magnetisation. Figure 3c) shows the fit of a dipolar function $D(\theta, \phi)$, which determines $\mathbf{m}'$. We find $\theta_m = 89.0 \pm 1°$, and $\phi_m = 39.1 \pm 1°$, where $\phi = 0$ is set to the $[\bar{1}10]$ direction. This result is consistent with spin polarized photoemission [20], though the magnetization is not aligned along the second easy axis $[1\bar{1}0]$ as it was the case for an other Ni(111) picture frame crystal [28]. The rotation of the sample and the incidence of the light impose on D *two* nodal lines ($\mathbf{m}' \cdot \mathbf{L}_{ph} = 0$): A circle at $\theta_o = 55°$, and a diameter perpendicular to ϕ_m. In Figure 3d) the residuum of the asymmetry and D is shown. It has the C$_3$ symmetry

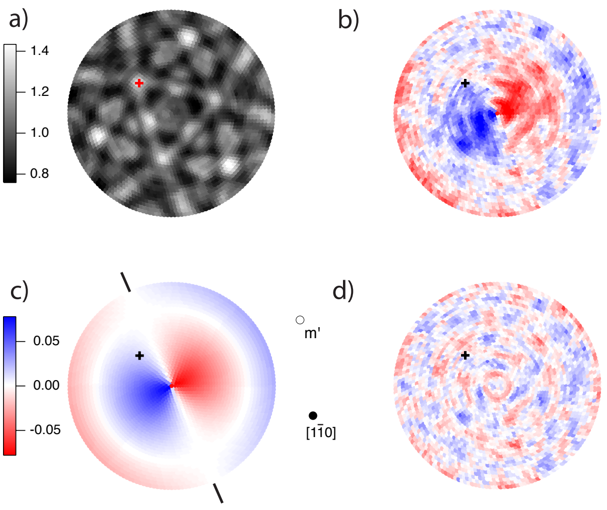

FIG. 3: (Color online) (a) Resonant x-ray photoelectron diffraction (RXPD) data of Ni(111). The 3500 stereographically projected data points for polar angles $0 \leq \theta \leq 70°$ of the intensity at α_2 (E_{kin}=863.8 eV, $\hbar\omega$ = 870.5 eV, σ^+) in Figure 2. The data are ϕ-averaged, i.e. normalized at each polar angle with the corresponding average intensity. The [011]-direction (cross), and the yoke axis along $[\bar{1}10]$ are marked. (b) Asymmetry of two XPD data sets at α_2 measured with right and left circularly polarized light. The twofold i.e. dipolar pattern reveals the direction of the magnetization. (c) D-function-fit to the asymmetry in (b). The direction of magnetisation $\mathbf{m}'$ and ticks for the corresponding azimuthal orientation at $\phi_m \pm 90°$ are indicated. (d) Residuum of the fit in (c) with respect to (b).

of the substrate and indicates further differences in the diffraction patterns due to different source waves created by σ^+ and σ^- photons, respectively. Such effects have been pioneered by Daimon et al., where they showed that the angular momenta of the photons are transferred to the photoelectrons, which in turn lead to an emitter scatterer distance dependent rotation of the forward scattering peak [11, 12].

For the data in Figure 3 b) we expect no photon induced rotation because in the asymmetry between σ^+ and σ^-any such effect should be canceled. This changes, when a dipolar function D is fitted to an individual XPD scan with either σ^+ or σ^- radiation. If we fit a dipolar function D to the data in Figure 3a), or the ones recorded with σ^- polarization, we find magnetisation directions which are within ±6° consistent with the magnetization direction as found from Figure 3 b). Although this has the practical advantage that the magnetization is determined without switching the light polarization, it is not very accurate since the D-function is much weaker than the forward scattering induced XPD patterns.

If we want to extract more quantitative information on the rotation of the D-functions upon use of light with plus or minus $\hbar$ angular momentum we have to perform a normalisation that removes the forward scattering intensity modulations and, in contrast to the asymmetry used in Figure 3, produces a pattern with a polarization. We do so in using the ϕ-averaged data $\bar{\alpha}_i^\sigma$ and form $\Delta\alpha_2^\sigma = 2 \cdot \bar{\alpha}_2^\sigma / (\bar{\alpha}_3^+ + \bar{\alpha}_3^-) - 1$ and vice versa.

As α_2 and α_3 electrons are expected to have very similar XPD patterns [15] - the wavelength-difference between the two selected electron energies of α_2 and α_3 is 1% - the XPD information on the atomic structure should be cancelled, though the $\Delta\alpha_i^\sigma$ are expected to show a polarization dependent rotation $\Delta\phi_m(\alpha_i, \sigma)$ of the observed magnetisation direction. For the 6 eV satellite, i.e. the L_2 resonance, we find a rotation $\Delta\phi_m$ of ±4.2° around the value of Figure 3b). It is related to the Daimon effect, i.e. forward scattering peak rotation [11]. Essentially, the angular momentum of an outgoing photoelectron induces a rotation of all features in the XPD patterns with respect to the crystal lattice. For single scattering the maximum angle of rotation γ_{max} is given by $n \cdot \hbar / (R \cdot p \cdot \sin^2(\theta_o))$, where R is the distance between emitter and scatterer, p the momentum of the outgoing electron and θ_o the angle between the light incidence and the electron detection (see Figure 1) [12, 29]. For nickel, n = 1, an electron kinetic energy of 850 eV and θ_o=55°, γ_{max} gets 2.2°. Of course, the angular shift is not isotropic, it depends on the angle between the electron angular momentum and the nearest neighbour directions. However, for an fcc material as it is nickel, the 12 nearest neighbours of an emitter in the bulk sit on a sphere with radius R, on the vertices of a cuboctahedron and must lead to a fairly isotropic rotation of the XPD patterns around the axis of the incoming photons. The $\Delta\phi_m(\alpha_2)$'s have the same sense of rotation as the corresponding photon angular momentum and are compatible with the transfer of $2\hbar$ of angular momentum to the emitted electrons.

Figure 4 shows the $\Delta\alpha_2^\sigma$ and the $\Delta\alpha_3^\sigma$ XPD scans for σ^+ and σ^- radiation. Dipolar functions (D) as shown in Figure 3c) appear, where the sign changes upon change of the polarization. The D-functions for $\Delta\alpha_2^\pm$ and $\Delta\alpha_3^\pm$ indicate $\Delta\phi_m$'s of ±4.2° and $\pm - 12.6°$, respectively. We want to note that the use of more than 3000 different photon incidence angles allows a very accurate ±0.8° determination of the $\Delta\phi_m(\alpha_2)$'s and permits for single quantum assignments $2\hbar$ ($-2\hbar$). In the $\Delta\alpha_3$ scans with a lower asymmetry (see Figure 2) the error increases by a factor of 3 and makes it compatible with angular momenta of $-6 \pm 2\hbar$ or $6 \pm 2\hbar$ (see Figure 4 e)). This surprising result implies that a L_3MM Auger electron channel produces electrons with large, opposite angular momentum compared to that of the photons. These results emphasise that the information on the angular momentum of an electron source wave may not only be accessed by a forward scattering peak rotation [11], but for magnetic systems also by the precise measurement of the source wave dependent circular magnetic dichroism.

In summary it has been shown that resonant x-ray

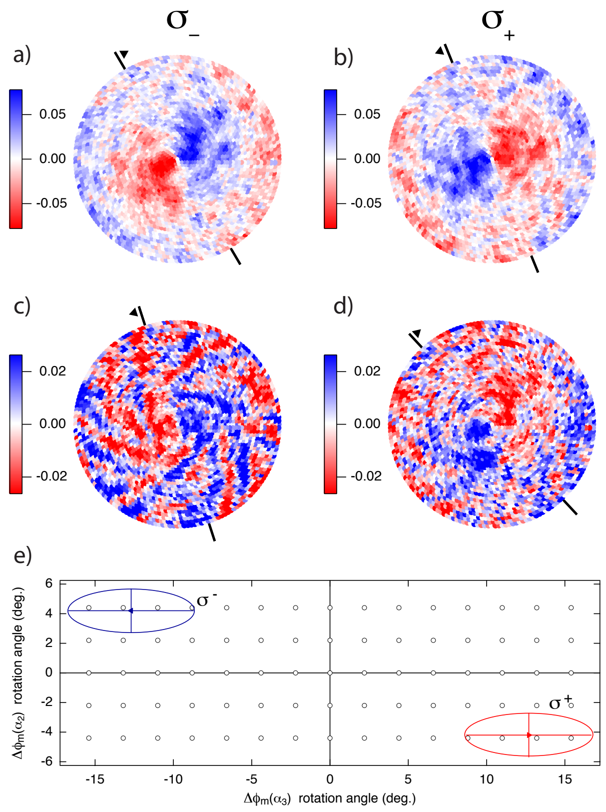

FIG. 4: (Color online) (a)-(d): Individual XPD scans with the same orientation as in Figure 3 of (a) $\Delta\alpha_2{}^-$, (b) $\Delta\alpha_2{}^+$, (c) $\Delta\alpha_3{}^-$ and (d) $\Delta\alpha_3{}^+$ (for definition see text). The ticks lie on the azimuth of the node of the corresponding dichroic dipole. The solid triangles indicate the rotation towards the magnetsisation direction. (e) Rotation angles $\Delta\phi_m(\alpha_2^\pm)$ versus $\Delta\phi_m(\alpha_3^\pm)$. For a given polarization the electrons rotate in opposite directions. The ellipses represent the error bars. The open circles are the rotation angles as expected from quantized angular momenta $n \cdot \hbar$.

photoelectron diffraction (RXPD) is suited to extract the atomic and magnetic structure of surfaces and interfaces. Furthermore it is demonstrated that the method directly accesses the angular momenta of the emitted electrons.

Fruitful discussions with J. Osterwalder and the support of the Swiss National Science Foundation are gratefully acknowledged. The experiments have been performed at the Swiss Light Source.

---

* Electronic address: greber@physik.uzh.ch

[1] M. A. Van Hove, Surface and Interface Analysis **28**, 36 (1999).
[2] C. S. Fadley, Journal of Electron Spectroscopy and Related Phenomena **178**, 2 (2010).
[3] P. Krüger, S. Bourgeois, B. Domenichini, H. Magnan, D. Chandesris, P. Le Fèvre, A. Flank, J. Jupille, L. Floreano, A. Cossaro, et al., Physical Review Letters **100**, 055501 (2008).
[4] M. Treier, P. Ruffieux, R. Fasel, F. Nolting, S. Yang, L. Dunsch, and T. Greber, Physical Review B **80**, 081403 (2009).
[5] H. Magnan, P. Le Fevre, D. Chandesris, P. Kruger, S. Bourgeois, B. Domenichini, A. Verdini, L. Floreano, and A. Morgante, Physical Review B **81**, 085121 (2010).
[6] C. Guillot, Y. Ballu, J. Paignè, J. Lecante, K. Jain, P. Thiry, R. Pinchaux, Y. Pètroff, and L. Falicov, Physical Review Letters **39**, 1632 (1977).
[7] L. A. Feldkamp and L. C. Davis, Physical Review Letters **43**, 151 (1979).
[8] L. Tjeng, C. Chen, P. Rudolf, and G. Meigs, Physical Review B **48**, 13378 (1993).
[9] G. van der Laan, International Journal of Modern Physics B **8**, 641 (1994).
[10] M. Weinelt, A. Nilsson, M. Magnuson, T. Wiell, A. Wassdahl, O. Karis, A. Föhlisch, N. Mårtensson, J. Stöhr, and M. Samant, Physical Review Letters **78**, 967 (1997).
[11] H. Daimon, T. Nakatani, S. Imada, S. Suga, Y. Kagoshima, and T. Miyahara, Japanese Journal of Applied Physics Part 2 - Letters **32**, L1480 (1993).
[12] H. Daimon, Physical Review Letters **86**, 2034 (2001).
[13] F. Matsui, T. Matsushita, and H. Daimon, Journal of Electron Spectroscopy and Related Phenomena **178**, 221-240 (2010).
[14] T. Greber, J. Osterwalder, S. Hüfner, and L. Schlapbach, Physical Review B **45**, 4540 (1992).
[15] T. Greber, J. Osterwalder, D. Naumovic, A. Stuck, S. Hüfner, and L. Schlapbach, Physical Review Letters **69**, 1947 (1992).
[16] J. Stöhr and H. Siegmann, *Magnetism - From Fundamentals to Nanoscale Dynamics* (Springer, 2006).
[17] C. Westphal, J. Bansmann, M. Getzlaff, and G. Schönhense, Physical Review Letters **63**, 151 (1989).
[18] A. Chassé, W. Kuch, M. Kotsugi, X. Gao, F. Offi, S. Imada, S. Suga, H. Daimon, and J. Kirschner, Physical Review B **71**, 014444 (2005).
[19] U. Flechsig, F. Nolting, A. Fraile Rodriguez, J. Krempasky, C. Quitmann, T. Schmidt, S. Spielmann, and D. Zimoch, AIP Conf. Proc. **1234**, 319 (2010).
[20] T. Okuda, J. Lobo-Checa, W. Auwärter, M. Morscher, M. Hoesch, V. N. Petrov, M. Hengsberger, A. Tamai, A. Dolocan, C. Cirelli, et al., Physical Review B **80**, 180404 (2009).
[21] C. Chen, N. Smith, and F. Sette, Physical Review B **43**, 6785 (1991).
[22] S. Hüfner, *Photoelectron Spectroscopy: Principles and Applications* (Springer, Berlin, 2003).
[23] M. Morscher, F. Nolting, T. Brugger, and T. Greber, Manuscript in Preparation (2011).
[24] M. Magnuson, N. Wassdahl, A. Nilsson, A. Föhlisch, J. Nordgren, and N. Mårtensson, Physical Review B **58**, 3677 (1998).
[25] J. Osterwalder, T. Greber, A. Stuck, and L. Schlapbach, Physical Review B **44**, 13764 (1991).
[26] J. Wider, F. Baumberger, M. Sambi, R. Gotter, A. Verdini, F. Bruno, D. Cvetko, A. Morgante, T. Greber, and J. Osterwalder, Physical Review Letters **86**, 2237 (2001).
[27] T. Greber, Journal of Physics - Condensed Matter **13**, 10561 (2001).
[28] M. Donath, Surface Science Reports **20**, 251 (1994).
[29] A. Chassé and P. Rennert, Physical Review B **55**, 4120

(1997).

6.4 Additional Information

In publication A, we use resonant photoelectron diffraction with circularly polarized light to determine the surface magnetization direction on the (111)-surface of a nickel yoke crystal. An XPD dataset is measured with both circularly left and right polarized light. The asymmetry of the two patterns can be fitted with a dipolar function, which allows to determine the magnetization direction quantitatively. When the fit is subtracted from the data, the twofold symmetry vanishes, and the residuum pattern is threefold symmetric. As shown in publication A, this residuum pattern can be expanded with spherical harmonics. The expansion reveals a sense of rotation in the residuum pattern. This rotation is probably related to the forward focusing peak (FFP) rotation effect that has been extensively studied by H. Daimon et al. A good review is given in [26]. It is a dichroism effect that was first observed on Si(001) [27], i.e. a nonmagnetic, nonchiral surface. The FFP rotation depends on the circular polarization of the incident x-ray beam, the FFPs are rotated clock- or counterclockwise around the light incidence axis. The rotation angle can be calculated as

$$\Delta = \frac{m}{kRsin^2\theta}$$

where m is the magnetic quantum number of the photoelectron, k the wave vector of the electron, R the distance between emitter and scatterer, and θ the angle between photon incidence direction and the outgoing photoelectron direction [26].

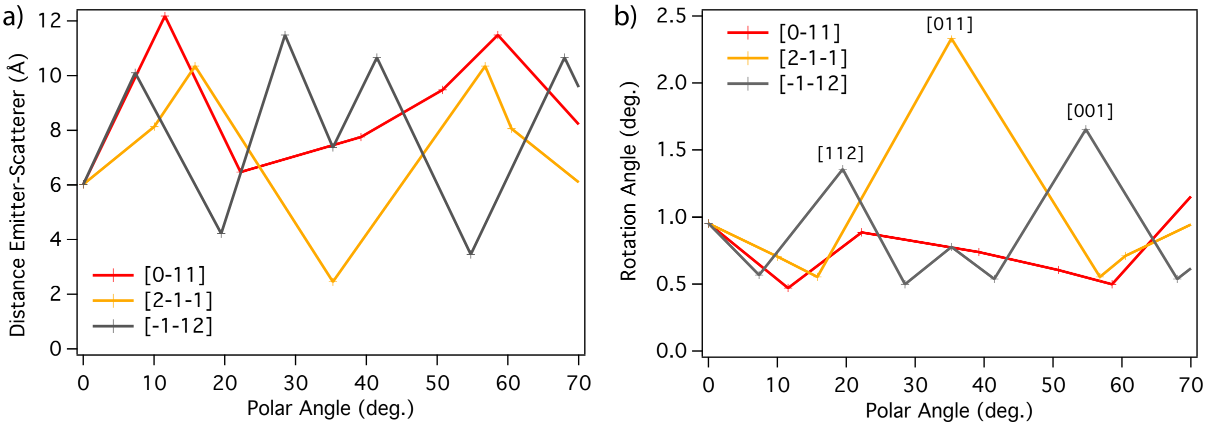

Figure 35: (a) Distance between emitter and scatterer on a fcc (111) surface, calculated for directions along the path between the (111) direction and three in-plane directions mentioned in the legend. (b) Calculated peak rotation angles for the FFPs in (a).

Most of the experiments that use the FFP rotation effect have been carried out using an elliptical display analyser. In such an analyser, the sample orientation is fixed relative

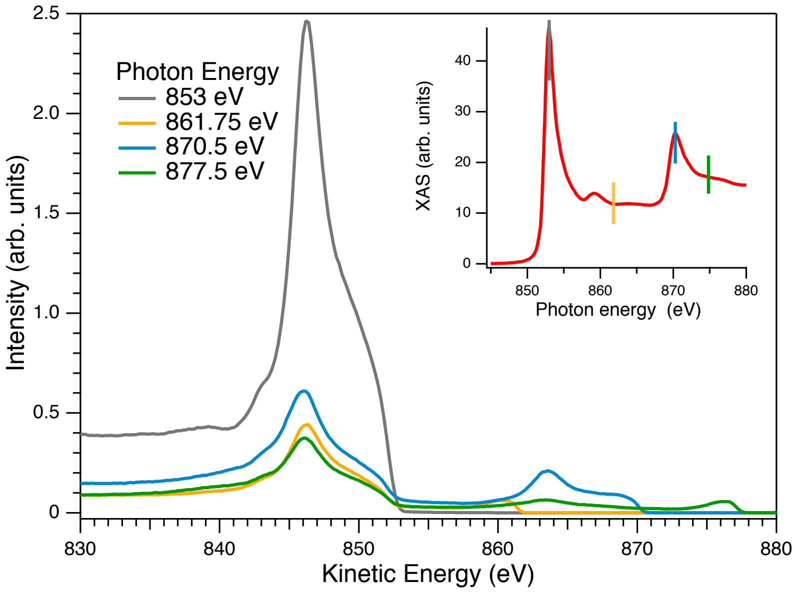

Figure 36: Photoemission spectra in the vicinity or on the L2, L3-resonances of nickel. The dramatic intensity increase of the resonant Auger $L_{2,3}MM$ peaks is clearly visible. The inset shows the XAS spectrum at the $L_{2,3}$-edge.

to the incident light. However, the direction of the outgoing electrons varies.

In our setup, the direction between the incident light and the analyser is kept fixed, but the sample is rotated. While in the display analyser case, both R and θ vary, in our case it is only R that is changing. For a (111)-surface, this is shown in figure 35(a), where R, i.e. the distance between emitter and scatterer, is plotted for cuts on the hemisphere above a (111) surface, where the cuts start at the [111] direction and end at the [0-11], the [2-1-1] and the [-1-23]-direction. Each datapoint represents a prominent FFP on the cut.

From the cuts, the rotation angle can be calculated. This is shown in figure 35(b). The rotation angle is not monotonically changing as a function of the polar angle, but oscillates between 0.5° and 2.3°. This difference is even given at a constant polar angle, for different azimuthal angles. This complicates the analysis of a XPD pattern considerably.

In figure 36, the Auger peak for four different photon energies close to or on the resonance energies of the L_2 and L_3 edge is shown. The dramatic increase of intensity on both Auger peaks at the corresponding resonance is clearly visible.

In publication A, we showed valence band resonant photoemission data with both circular polarization at the L_2 and the resulting asymmetry for one sample orientation and one magnetization direction. In figure 37, the same spectra are plotted again, however now all combinations of polarization, opposite sample orientations and magnetizations are shown. The first panel corresponds to the figure in publication A. In (b) the asymmetry is formed as $\frac{M_+ - M_-}{M_+ + M_-}$ for both circular polarizations and for opposite sample orientations. When the polarization is switched while keeping the sample orientation constant, the sign of the asymmetry changes. Correspondingly, when the polarization is keepd fixed, the asymmetry changes sign when the sample is rotated by 180°. In the third panel, the asymmetry is calculated as $\frac{\sigma_+ - \sigma_-}{\sigma_+ + \sigma_-}$. Again, if the magnetization or the orientation is reversed, the asymmetry changes its sign correspondingly. The same is true for (d), where the asymmetry is formed as $\frac{\phi_0 - \phi_\pi}{\phi_0 + \phi_\pi}$, and the polarization and the magnetization are switched.

6.5 PEEM Results

Two short experiments at the PhotoElectron Emission Microscope (PEEM) at the SLS made it possible to look at the domain structure of the yoke crystal. The crystal was placed into a special sampleholder where a Swissstub sample holder can be mounted such that it can be introduced into the Elmitec PEEM, with heating contacts and thermocouple attached. In the first beamtime, the sample was still covered with h-BN and $Dy_3N@C_{80}$ from the beamtime mentioned in chapter 9. Considering the lower surface sensitivity of PEEM compared to photoemission, this is not critical for our purpose. Before the second beamtime, the crystal was cleaned with three cycles of argon sputtering and annealing. The crystal was then magnetized as explained above, i.e. with a direct current of 2A for 30s or by using a current pulser.

It is possible to record PEEM images even at 2A of current through the coil, which means that the stray field at the surface must be below ~ 200 Gauss.

In figure 38, three typical topography images (a, c, e) and corresponding dichroism images (b, d, f) are displayed. The field of view (FOV) for these images was 50 µm. The photon energy was set to the Ni L3 edge. The topography images have been calculated as the sum of two PEEM images with opposite circular polarizations. The dichroism images are obtained by dividing two images with opposite circular polarizations. In the topography images, some scratches from polishing can be seen, a lot in (a) and only a few in (c) and (e). Furthermore, defects or dirt on the surface is visible in the form of white spots. These spots have been used as a position marker, when the sample was rotated.

In the dichroism images (b) and (d), the domain structure is composed of small scale features that are not clearly resolved at this FOV. However, in (f), very large domains appear, domains that are too big for this FOV. Obviously there are processes on several length scales involved. To better understand the domain structure, more beamtime would be needed.

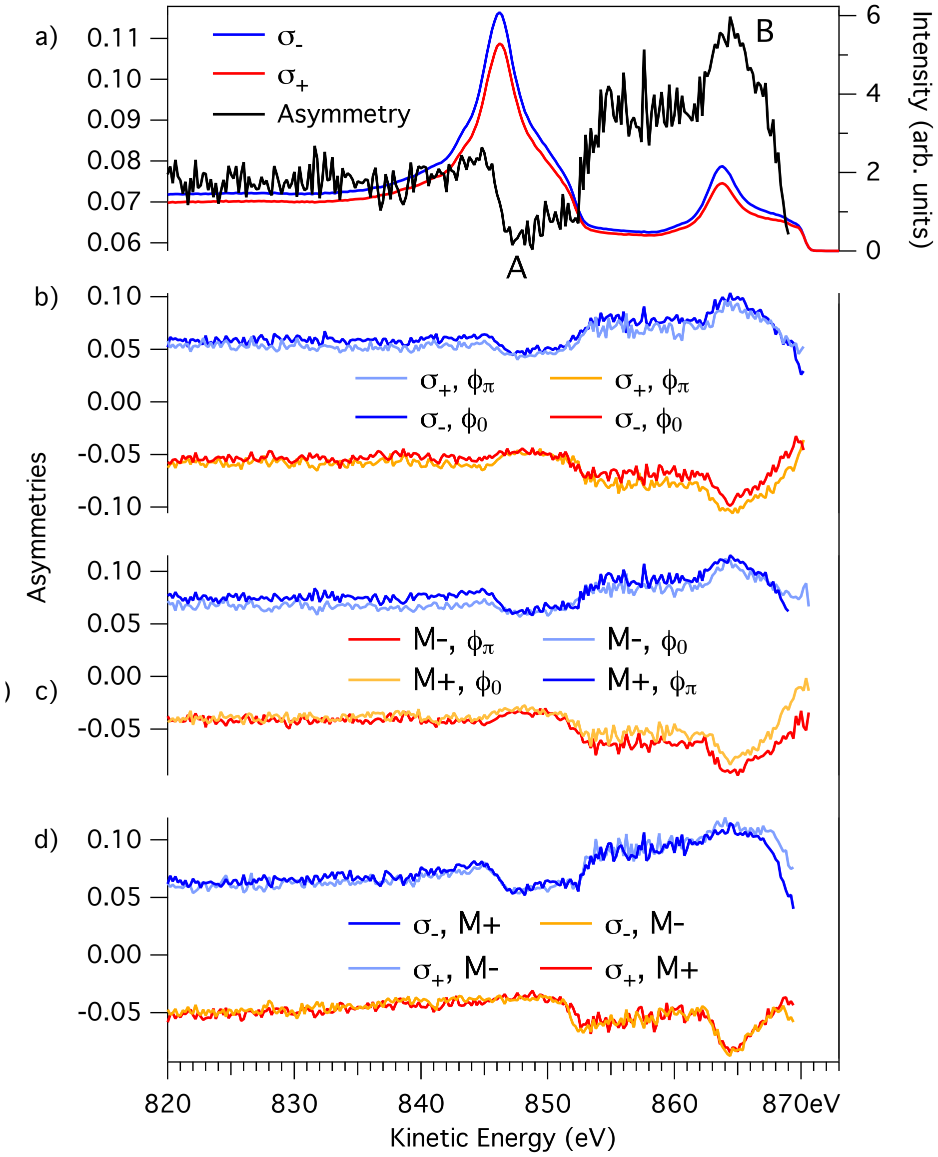

Figure 37: (a) Photoemission spectra with left and right circularly polarized light at 10° polar angle, where the photon energy is set on the Ni L_2-edge ($\hbar\omega$=870.5 eV). The asymmetry exhibits two distinct peaks A and B, on which we performed the XPD measurements shown in publication A. (b)-(d) Photoemission spectra asymmetries. Eight photoemission spectra were measured, with both circular polarizations (σ_+, σ_-), opposite magnetizations (M_+, M_-) and opposite sample positions (ϕ_0, ϕ_π). From these, asymmetries can be formed as follows: In (b), the asymmetry is calculated as $\frac{M_+ - M_-}{M_+ + M_-}$ for both polarisations and at opposite angles. As expected, the asymmetry changes its sign when the polarization is switched or when the crystal is rotated by 180°. In (c), the asymmetry is $\frac{\sigma_+ - \sigma_-}{\sigma_+ + \sigma_-}$, for opposite magnetizations and angles. The asymmetry also changes when the magnetization is switched. In (d), the asymmetry is formed as $\frac{\phi_0 - \phi_\pi}{\phi_0 + \phi_\pi}$. (b)-(d) consistently show that the peaks in the asymmetry are due to the dichroism in photoemission.

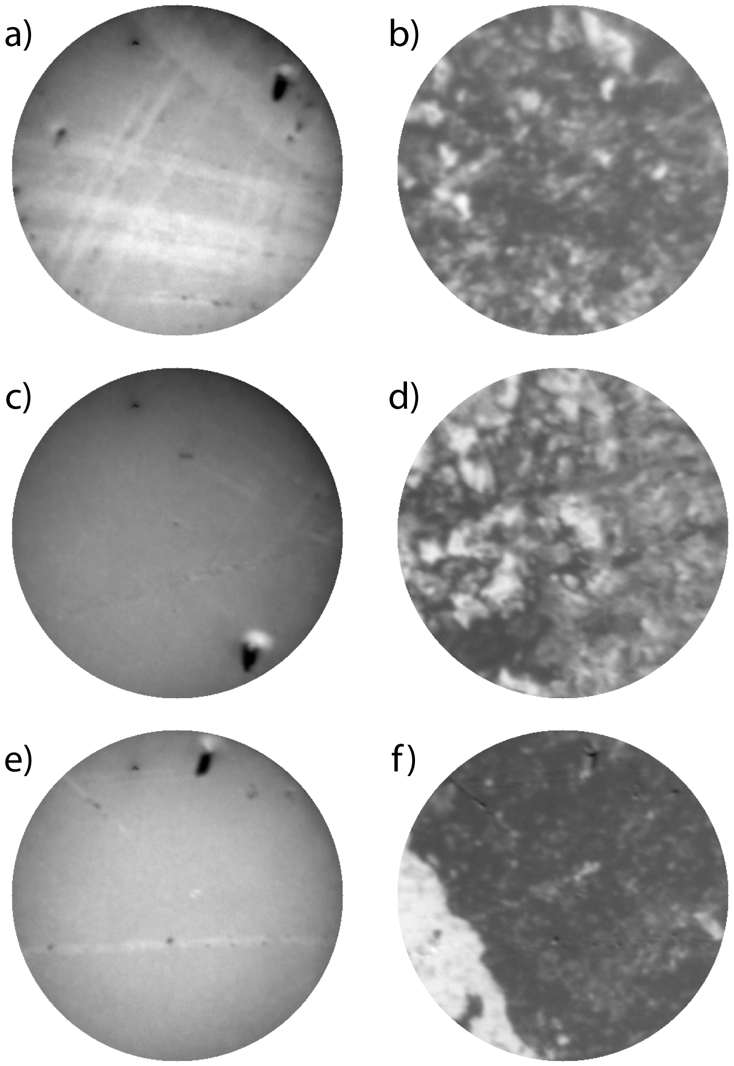

Figure 38: Three examples for PEEM images on the Ni(111) surface (a, c, e) and the corresponding dichroism images (b, d, f). All images are recorded with a field of view (FOV) of 50 µm. The photon energy was set to the Ni L3-edge. The angle between surface normal and photon incidence is 74°. In the topography images, some scratches from polishing are visible and some small defects which were used as orientation points. The dichroism images are calculated by dividing two images of opposite circular polarization, not by forming the asymmetry. In the dichroism images (b) and (d), only small scale structures are visible, which cannot be understood at this FOV. In (f), two large domains appear, with some substructures that cannot be resolved as well. The light incidence direction can be inferred from the shadow at the defects in the topography images.

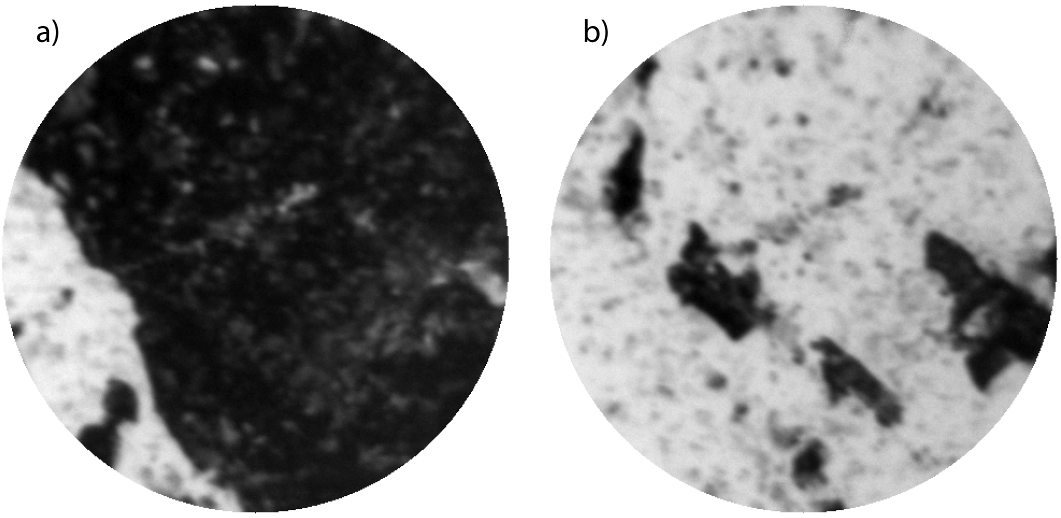

Figure 39: Example for the change of the domain structure when the magnetization is reversed. The image parameters are the same as in figure 38, the position does not change between (a) and (b).

7 $Ar@C_{60}$

7.1 Summary

Multilayers of endohedral Ar in C_{60} have been prepared and measured with photoelectron spectroscopy. A strong hybridization between the Ar 3p level and the close-lying $6T_{1u}$-level is found. Both bonding and antibonding orbital can be resolved in the photoemission spectra. No giant Ar 3p cross section enhancement, as predicted by Madjet et al. [28], was found. These results are shown in publication B, which has been accepted at Physical Review A. Additional data with He IIα-radiation are shown where the cross-section can be extracted for a higher photon energy.
Furthermore, the ratio between the HOMO and HOMO-1 is analyzed for $Ar@C_{60}$and compared to C_{60}, where this ratio is known to exhibit oscillations as a function of the photon energy[29].
Additionally, we discuss radiation damage in $Ar@C_{60}$, which was observed for He I, II-α-radiation as well as for Mg Kα x-rays.

7.2 Introduction

Endohedral noble gas fullerenes have been a subject of intense theoretical work concerning the photoionization properties, numerous papers have appeared ([30, 31, 32, 33] and references therein). The photoionization cross section of the guest atom is expected to be strongly modified by the interaction with the surrounding cage. However, so far no experimental work on photoionization of endohedral noble gas fullerenes has been reported. The reason is the difficult and laborious synthesis of even smallest sample quantities. Recently, N. Dragoe, S. Ito and H. Takagi succeeded in the production of several milligrams. This quantity allowed them to study the superconducting properties of $Ar@C_{60}$ doped with alkali metals [34, 35]. A small quantity of these molecules has been used for the experiments presented below.

There are two main questions to be addressed. First, the electronic structure of the guest atom in the C_{60} cage needs to be determined. It is expected that argon, a noble gas, only weakly interacts with the cage, since the valence shell is completely filled. However, at least van der Waals and Pauli repulsion must be present.

The second question is the influence of the cage on the characteristic line shape of the gas phase Ar spectrum. We focus on the Ar 3p level, which is spin-orbit split in the photoemission spectrum by 177 meV. Madjet et al. [**?**] have predicted a giant enhancement of the Ar 3p cross section compared to free argon by one order of magnitude at 21.2 eV. This should be easily observable in the experiment. The enhancement is due to a coupling between the Ar 3p level and the C_{60} cage which allows the Ar atom to participate in the C_{60} photoionization channels.

Furthermore, it is well known that the peaks of adsorbed molecules are significantly broadened compared to the gas phase. The same is true for condensed argon where the spin-split Ar 3p levels are broadened such that the splitting cannot be resolved anymore. Several explanations for line broadening have been put forth ([36],[37]). For $Ar@C_{60}$, it is interesting to study if the Ar 3p lines are broadened as well.

An interesting theory which could not be addressed here has been discussed by Averbukh et al. [38]. They studied interatomic Coulomb decay (ICD) in $Ne@C_{60}$. Unfortunately, in $Ar@C_{60}$ this effect can only be studied with synchrotron radiation, because the Ar 3s level, for which ICD is expected, is not accessible with He Iα radiation and the cross section is too low for He IIα.

7.3 Publication B

Publication B has been accepted for publication in Physical Review A.

PHYSICAL REVIEW A **82**, 051201(R) (2010)

Strong $3p$-T_{1u} hybridization in Ar@C_{60}

M. Morscher,[1] A. P. Seitsonen,[2] S. Ito,[3] H. Takagi,[3] N. Dragoe,[4] and T. Greber[1,*]
[1] *Physik-Institut, Universität Zürich, Winterthurerstrasse 190, CH-8057 Zürich, Switzerland*
[2] *Physikalisch-Chemisches Institut, Universität Zürich, Winterthurerstrasse 190, CH-8057 Zürich, Switzerland, and IMPMC, CNRS and Université Pierre et Marie Curie, 4 place Jussieu, case 115, F-75015 Paris Cedex 05, France*
[3] *Department of Advanced Materials, University of Tokyo, Kashiwa-no-ha 5-1-5, Kashiwa 277-8561, Japan*
[4] *Laboratoire d'Ètude des Matériaux Hors Équilibre (LEMHE-ICMMO), UMR 8182-CNRS, Université Paris Sud, F-91405 Orsay, France*

(Received 1 July 2010; published 29 November 2010)

Multilayers of fullerenes with and without endohedral Ar units, Ar@C_{60} and C_{60}, were investigated by photoemission and density-functional theory. The stoichiometry and the endohedral nature of Ar were checked by x-ray photoelectron spectroscopy and x-ray photoelectron diffraction. Valence-band ultraviolet photoemission spectra showed a strong hybridization of the Ar $3p$ valence shell with the $6T_{1u}$ molecular orbital of C_{60}. A hybridization gap of 1.6 ± 0.2 eV was found. This is in agreement with density-functional theory, which predicts 1.47 eV and indicates that Ar@C_{60} is a noble gas compound with a strong coupling between Ar and the C_{60} cage. No giant Ar photoemission cross section as previously predicted for the gas phase in Phys. Rev. Lett. **99** 243003 (2007) was found.

DOI: 10.1103/PhysRevA.82.051201 PACS number(s): 61.48.−c, 71.20.Tx, 33.60.+q, 61.05.js

Shortly after the discovery of C_{60} [1], it was proposed that fullerene carbon cages could be filled with other atoms or molecules [2]. The realization of such molecules, called endofullerenes or incar-fullerenes, was expected to lead to new functionalities, where the endohedral units are isolated by the carbon cage from the surroundings. Single nitrogen atoms in C_{60} are a prominent example [3], where the paramagnetic nature of atomic nitrogen even led to the idea of using N@C_{60} as a qubit [4].

Nuclear magnetic resonance [5] and electron-spin resonance [3] were the first probes of the interior of fullerenes, and photoemission allowed the determination of the valency of endohedral units [6]. The first view inside endofullerenes came from spectacular transmission electron microscopy experiments on so-called peapods, where single Gd atoms that were seen inside C_{82} were lined up in a single-wall nanotube [7]. Only recently, x-ray photoelectron diffraction allowed a direct look at the arrangement of Dy_3N inside C_{80} [8].

Fullerenes containing noble gases were particularly useful for studies on the influence of the endohedral unit on the molecular properties [5,9] and vice versa. There are extended x-ray-absorption fine-structure [10] and x-ray-diffraction experiments [11] on Kr@C_{60}. For Ar@C_{60}, it was shown, for example, that in K_3Ar@C_{60} samples the superconducting transition temperature decreased compared to K_3C_{60} [12]. It was also predicted that the dynamic coupling between Ar and the C_{60} cage would lead, near the C_{60} plasmon frequency, to a giant photoemission cross-section enhancement [13].

All these phenomena call for a better understanding of the coupling between the endohedral unit and the fullerene cage. In this Rapid Communication, we explore Ar@C_{60} layers by means of photoemission, where a comparison with C_{60} allows the quantitative determination of the hybridization between Ar and C_{60}. The hybridization turns out to be larger than the Ar valence-band width in condensed Ar, which establishes Ar@C_{60} as a noble gas compound.

Photoemission experiments rely on highly purified samples. For endohedral fullerenes, the synthesis is difficult due to the low production yield and the many purification cycles using high-pressure liquid chromatography. Several milligrams of Ar@C_{60} have been produced with a purity >95% [12]. To efficiently deposit the molecules on a substrate, we employed a custom-made evaporator with mini Knudsen cells that can be closely approached to the sample (∼2–3 cm). This allows the preparation of layers from small amounts of material. We used about 10 μg of Ar@C_{60}. The experiments were performed in a modified VG ESCALAB 220 photoemission spectrometer with a base pressure of $< 5 \times 10^{-10}$ mbar [14]. All data were measured at room temperature. As a substrate, we used an Al(111) single crystal that was cleaned by repeated cycles of neon ion sputtering (15 min, 1 keV, $\sim 1.5\ \mu A/cm^2$) and annealing to ∼700 K. The coverages and the cleanliness of the samples were examined with x-ray photoelectron spectroscopy (XPS). The molecular ordering and the endohedral position of argon were evidenced by x-ray photoelectron diffraction (XPD) [15]. Valence-band photoemission spectra were recorded with monochromatized He $I\alpha$ radiation ($\hbar\omega = 21.2$ eV). Experiments with layers between 3 and 7 monolayers of C_{60} or Ar@C_{60} have been performed.

The gas-phase geometric and electronic structure of Ar@C_{60} and C_{60} was determined using density-functional theory (DFT) and the wave-function-based Moller-Plesset method (MP2) with the computer code TURBOMOLE [16]. The Gaussian basis set triple-zeta valence double polarization [17] was used in both calculations, and the exchange-correlation functionals employed in the DFT calculations were the local-density approximation (LDA) and PBE0 [18]. We obtain Ar $3p$ C_{60} T_{1u} hybridization gaps of 1.46, 1.69, and 1.45 eV for PBE0, MP2, and LDA, respectively. In contrast to the calculations in

---

[*] greber@physik.uzh.ch

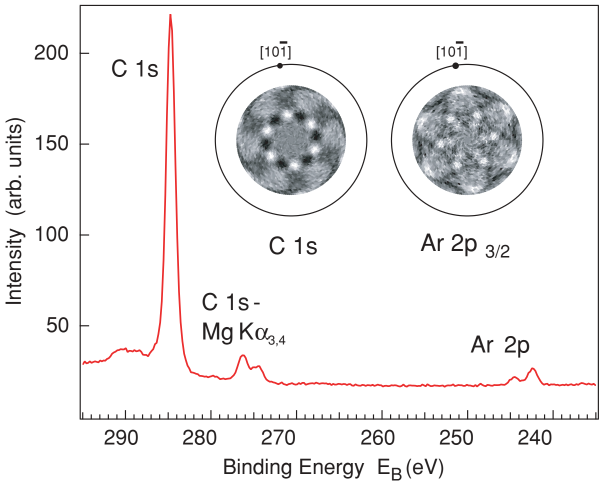

FIG. 1. (Color online) Mg $K\alpha$ XPS and corresponding angle-scanned XPD pattern of Ar@C_{60}. XPS indicates a film thickness of seven monolayers and a C:Ar stoichiometry of $(63 \pm 2) : 1$. The C 1s ($E_B = 284.7$ eV) and Ar $2p_{3/2}$ ($E_B = 242.4$ eV) XPD patterns show azimuthal ordering of the molecules, where the high anisotropy ratio between Ar 2p and C1s indicates that Ar sits inside the carbon cages.

Ref. [13] where the 240 carbon valence electrons are treated as jellium in a spherical shell, here the full atomic structure is taken into account.

Figure 1 shows the characterization of an Ar@C_{60} layer on Al(111). The x-ray photoelectron spectrum consists of a dominant C 1s and a weak Ar 2p peak. From the intensity ratio and the atomic cross sections, a C:Ar atomic ratio of $(56 \pm 7) : 1$ is inferred from two different preparations. This is consistent with the nominal stoichiometry of Ar@C_{60} and indicates no significant contribution of contaminations containing carbon, such as, for example, C_{60} molecules from an incomplete purification process. In contrast to early reports [19], no evidence for depletion of argon was found under Mg $K\alpha$ and He $I\alpha$ radiation. As for Dy_3N@C_{80} on Cu(111) [8], the XPD patterns in Fig. 1 have sixfold rotational symmetry for the carbon cage as well as for the endohedral unit. The anisotropy of the Ar signal is 6.8 times larger than that of the carbon pattern. As for nitrogen in Dy_3N@C_{80} [8], this indicates Ar in the center of C_{60}, which was confirmed by scattering simulations of 60 carbon emitters compared with the pattern of a single emitter in the center of C_{60}.

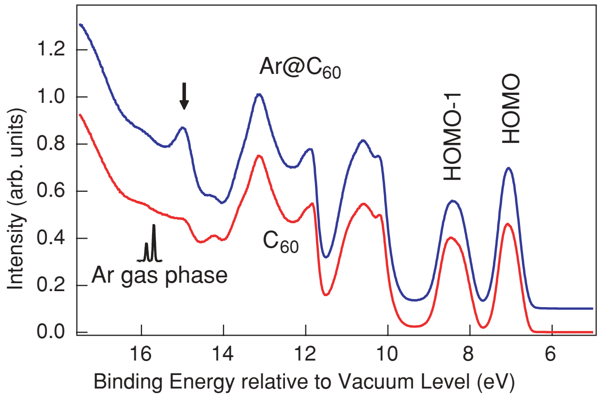

FIG. 2. (Color online) He $I\alpha$ excited normal emission spectra of Ar@C_{60} (blue upper curve), C_{60} (red lower curve), and gas phase Ar (black inset). The energies refer to the vacuum level. The arrow at 15 eV indicates the Ar peak in the Ar@C_{60} spectrum, which lies, due to better screening of the photoemission final state, above the Ar 3p gas-phase lines.

Figure 2 shows the valence-band photoemission spectra of multilayers of C_{60} and Ar@C_{60}. The two spectra look similar and are dominated by the molecular orbitals of the C_{60} cages. The energies are referenced with respect to the vacuum level, and no significant energy shift between the highest occupied molecular orbital (HOMO) of C_{60} and Ar@C_{60} is observed. However, at about 15 eV, Ar@C_{60} has a clear additional feature. As the inset shows, the energy is close to the Ar 3p levels in the gas phase, with an ionization potential of 15.76 eV. Endohedral Ar has a lower 3p binding energy and a larger peak width (0.53 eV) than in the gas phase where the spin-orbit splitting of 177 meV [20] is resolved. In line with photoemission from condensed Ar [20,21], this indicates a better screening and a significant coupling of the photoemission final state to the many degrees of freedom in the molecule. There is also an indirect indication on the endohedral species: The partial cross-section ratio between the two molecular orbitals HOMO and HOMO-1 is 0.96 ± 0.02 and 0.84 ± 0.01 for Ar@C_{60} and C_{60}, respectively. In view of the known oscillations of the partial photoemission cross sections [22,23] and its understanding [24], this is an indication that the potential of the endohedral unit influences the phase of photoelectrons from different molecular orbitals differently. The intensity of the Ar-induced feature, however, does not confirm a giant photoemission cross section as predicted by theory, where it was argued that the coupling of the photon to the C_{60} and the Ar cage could enhance the cross section due to resonant interchannel coupling between the Ar 3p and the C_{60} photoemission channels [13].

In order to better understand the coupling between the endohedral unit and the C_{60} cage, we performed DFT calculations that yield the eigenvalues and symmetries of the C_{60} and Ar@C_{60} molecular orbitals. The expectation that the Ar 3p level only interacts with molecular orbitals with the corresponding symmetry (T_{1u}) with similar energy and overlap is confirmed nicely. Figure 3 shows calculated PBE0 eigenvalues of C_{60} and Ar@C_{60}. Up to $6T_{1u}$ with the same symmetry as the Ar 3p level, the C_{60} orbitals are unaffected by Ar; that is, they have energy differences for C_{60} and Ar@C_{60} below 25 meV. In C_{60}, $5T_{1u}$ is an orbital with σ bond character and shows no hybridization (less than 1 meV) due to the lack of overlap. The $6T_{1u}$ orbital with π character and the nearby Ar 3p orbital hybridize in Ar@C_{60} into a bonding orbital (B) and an antibonding orbital (AB), split by 1.47 eV. This indicates a strong hybridization between the endohedral Ar unit and the C_{60} cage. The $2A_g$ orbital of C_{60} at an energy of 27.62 eV is not shown in Fig. 3. Theory predicts a 455-meV 3s-$2A_g$ hybridization, though these energy levels are experimentally not accessible with He $I\alpha$ radiation.

If we want to compare the theoretical prediction with the experiment, we first have to assign the Ar peak (see Fig. 2) to the B or the AB orbital. For this purpose, the theoretical molecular orbital eigenvalues are correlated with

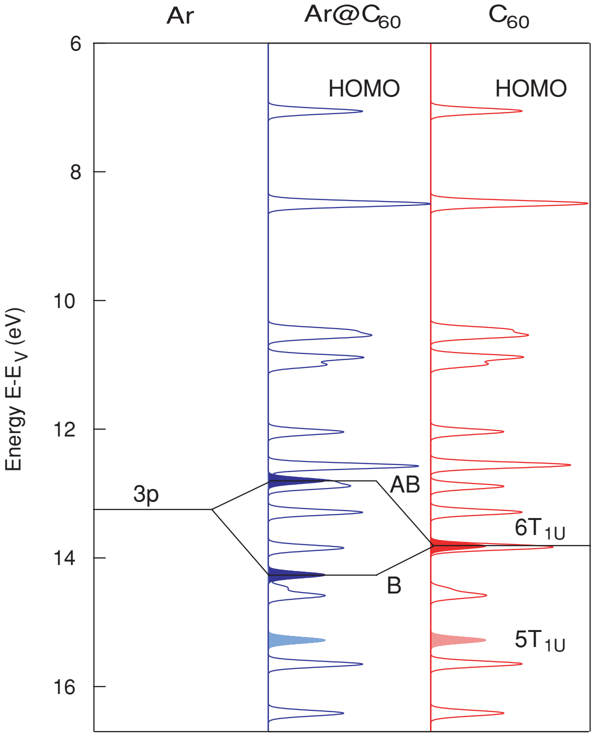

FIG. 3. (Color online) Energy eigenvalues (PBE0) of molecular orbitals of C$_{60}$ and Ar@C$_{60}$ as calculated with DFT. The orbital energies refer to the vacuum level E_V and are broadened by a Gaussian with 100-meV full width at half maximum. The orbitals with T_{1u} symmetry are solid. In C$_{60}$, 5T_{1u} is a σ orbital and 6T_{1u} a π orbital. 6T_{1u} hybridizes with the Ar $3p$ shell into a B and an AB orbital with a theoretical splitting of 1.47 eV.

the experimentally observed molecular orbital peaks [25]. If we assume the deviation between theory and experiment to be proportional to the energy [25], the PBE0 results suggest that the experimental Ar peak is 0.64 eV more strongly bound than the calculated B orbital. This difference between experiment and theory is 2.16 eV when we assign the AB orbital to the Ar peak at 14.95 eV. For MP2 calculations, B also fits with a corresponding difference of −0.57 eV better in the experiment than AB, where the difference is 1.25 eV. We therefore assign the experimentally distinct Ar peak to the Ar $3p$–C$_{60}$ 6T_{1u} bonding hybrid B. For the experiment, this means that the antibonding $3p$-6T_{1u} hybrid orbital must have a lower binding energy than the Ar peak and that the 6T_{1u} orbital of C$_{60}$ must lie in between them. A closer inspection of the spectra in Fig. 2 shows that this is the case. The corresponding region of interest is shown in Fig. 4(a). In order to quantify the difference between the two spectra, we show the asymmetry $A = [I(\mathrm{Ar@C_{60}}) - I(\mathrm{C_{60}})]/[I(\mathrm{Ar@C_{60}}) + I(\mathrm{C_{60}})]$ between the Ar@C$_{60}$ and the C$_{60}$ spectrum in Fig. 4(b). Clearly, the Ar peak (B) has the largest asymmetry, and at 1.6 eV above this line a new peak shows up. Between the two Ar@C$_{60}$ peaks, a C$_{60}$ peak (with a local asymmetry minimum) is seen. With this we can identify the $3p$-6T_{1u} AB hybrid and the 6T_{1u} C$_{60}$ molecular orbital. The asymmetry curve in Fig. 4(b) is not flat below B and above AB. This is likely related to the fact that the photoemission cross sections of all other molecular orbitals are affected by the endohedral unit, as seen in the different HOMO:(HOMO-1) intensity ratios.

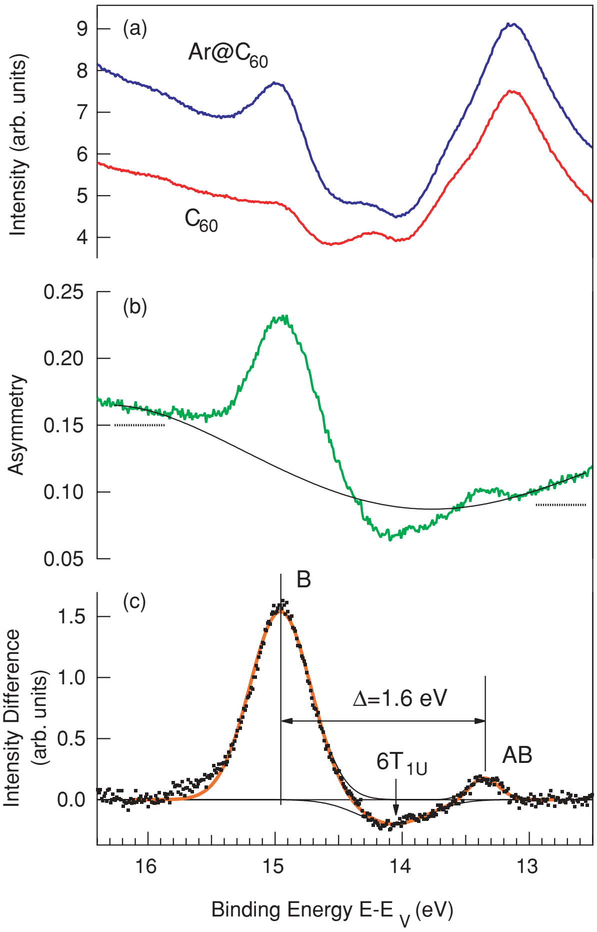

FIG. 4. (Color online) Experimental evidence for the $3p$-T_{1u} hybridization in Ar@C$_{60}$ (blue) by comparison with C$_{60}$ (red). (a) Raw data as extracted from the spectra in Fig. 2. (b) Asymmetry between Ar@C$_{60}$ and C$_{60}$ (green) and the background that has been subtracted for quantification. The dashed horizontal lines are the supporting points of the background polynomial. (c) Difference between Ar@C$_{60}$ and C$_{60}$ from (a) and the asymmetry in (b) without background. The splitting Δ between the bonding and the antibonding hybrid is 1.6 ± 0.2 eV. The negative part of the difference indicates the 6T_{1u} orbital of empty C$_{60}$.

In order to quantify the difference between Ar@C$_{60}$ and C$_{60}$, we subtract a fourth-order polynomial background from the asymmetry curve in Fig. 4(b) and reconstruct the difference between the Ar@C$_{60}$ and C$_{60}$ spectrum. In Fig. 4(c), this difference shows a splitting Δ between B and AB of 1.6 ± 0.2 eV, which is close to the calculated value of 1.47 eV. As expected, the hybridizing 6T_{1u} molecular orbital of C$_{60}$ shows up with negative values in the intensity difference between Ar@C$_{60}$ and C$_{60}$. It lies 0.7 eV below AB, or 0.9 eV above B. This suggests that AB has more 6T_{1u} character and correspondingly B more Ar $3p$ character. If 6T_{1u} would lie in the middle between B and AB, no big difference between the intensity of B and AB would be expected. The ratio between the B and AB intensity depends on the position in the hybridization gap. Together with the fact that the He $I\alpha$ photoemission cross section is larger for an Ar $3p$ electron than for a C $2p$ electron, this is consistent with the observation that B has a stronger cross section than AB.

Finally, we would like to discuss the absolute photoemission cross sections of the different molecular orbitals. For the ten HOMO electrons of C_{60}, the experimental photoemission cross section at 21-eV photon energy is 100 and 50 Mb for the gas phase [26] and condensed C_{60} [27], respectively. Comparison of these cross sections with that of atomic C $2p$ (1.5 Mb/e^-) [28] suggests for the molecule a C $2p$ cross-section enhancement of a factor 7 to 3. The data shown in Fig. 4 allow a comparison of the Ar@C_{60} hybrid orbital cross section, which turns out to be 0.44 ± 0.05 times that of the HOMO and is close to the value of 38 Mb for the Ar $3p$ level [28]. This corresponds to the values as expected from the semiclassical result, and thus we have no indication of a giant cross-section enhancement in low-energy photoemission of Ar in solid Ar@C_{60}, as was proposed for the gas phase [13]. A possible source for the discrepancy might be the energy of the plasmon excitation. In Ref. [13], the giant enhancement is assigned to a redistribution of oscillator strength between a plasmon of C_{60} at 16.5 eV and the close-lying Ar $3p$ level at 15.76 eV. However, the experimental plasmon excitation for C_{60} is about 20 eV in the gas phase, while it shifts to 28 eV in the bulk [29], and a possible resonance between Ar and the C_{60} cage is likely detuned.

In conclusion, it is shown that in Ar@C_{60}, the Ar $3p$ and the C_{60} $6T_{1u}$ orbital strongly hybridize. This coupling between the endohedral unit and the carbon cage establishes Ar@C_{60} as a noble gas compound.

Technical support by Martin Klöckner is gratefully acknowledged. The project was financially support by the Swiss National Science Foundation.

---

[1] H. W. Kroto, J. R. Heath, S. C. O'Brien, R. F. Curl, and R. E. Smalley, Nature (London) **318**, 162 (1985).

[2] J. R. Heath, S. C. O'Brien, Q. Zhang, Y. Liu, R. F. Curl, H. W. Kroto, F. K. Tittel, and R. E. Smalley, J. Am. Chem. Soc. **107**, 7779 (1985).

[3] T. Almeida Murphy, T. Pawlik, A. Weidinger, M. Höhne, R. Alcala, and J. M. Spaeth, Phys. Rev. Lett. **77**, 1075 (1996).

[4] W. Harneit, Phys. Rev. A **65**, 032322 (2002).

[5] M. Saunders, H. A. Jiménez-Vázquez, R. J. Cross, S. Mroczkowski, M. L. Gross, D. E. Giblin, and R. J. Poreda, J. Am. Chem. Soc. **116**, 2193 (1994).

[6] T. Pichler, M. S. Golden, M. Knupfer, J. Fink, U. Kirbach, P. Kuran, and L. Dunsch, Phys. Rev. Lett. **79**, 3026 (1997).

[7] K. Suenaga, T. Tence, C. Mory, C. Colliex, H. Kato, T. Okazaki, H. Shinohara, K. Hirahara, S. Bandow, and S. Iijima, Science **290**, 2280 (2000).

[8] M. Treier, P. Ruffieux, R. Fasel, F. Nolting, S. F. Yang, L. Dunsch, and T. Greber, Phys. Rev. B **80**, 081403 (2009).

[9] M. Saunders, R. J. Cross, H. A. Jiménez-Vázquez, R. Shimshi, and A. Khong, Science **271**, 1693 (1996).

[10] S. Ito, A. Takeda, T. Miyazaki, Y. Yokoyama, M. Saunders, R. J. Cross, H. Takagi, P. Berthet, and N. Dragoe, J. Phys. Chem. B **108**, 3191 (2004).

[11] H. M. Lee, M. M. Olmstead, T. Suetsuna, H. Shimotani, N. Dragoe, R. J. Cross, K. Kitazawa, and A. L. Balch, Chem. Commun. 1352 (2002).

[12] A. Takeda *et al.*, Chem. Commun. 912 (2006).

[13] M. E. Madjet, H. S. Chakraborty, and S. T. Manson, Phys. Rev. Lett. **99**, 243003 (2007).

[14] T. Greber, O. Raetzo, T. J. Kreutz, P. Schwaller, W. Deichmann, E. Wetli, and J. Osterwalder, Rev. Sci. Instrum. **68**, 4549 (1997).

[15] J. Osterwalder, T. Greber, A. Stuck, and L. Schlapbach, Phys. Rev. B **44**, 13764 (1991).

[16] R. Ahlrichs, M. Bär, M. Häser, H. Horn, and C. Kölmel, Chem. Phys. Lett. **162**, 165 (1989).

[17] A. Schäfer, C. Huber, and R. Ahlrichs, J. Chem. Phys. **100**, 5829 (1994).

[18] PBE0 is a hybrid functional in which 25% of Hartree-Fock exchange is mixed into the generalised gradient approximation by Perdew, Burke and Ernzerhof [J. P. Perdew, K. Burke and M. Ernzerhof, Phys. Rev. Lett. **77**, 3865 (1996)].

[19] B. A. DiCamillo, R. L. Hettich, G. Guiochon, R. N. Compton, M. Saunders, H. A. Jiménez-Vázquez, A. Khong, and R. J. Cross, J. Phys. Chem. **100**, 9197 (1996).

[20] U. Hergenhahn, S. Barth, V. Ulrich, M. Mucke, S. Joshi, T. Lischke, A. Lindblad, T. Rander, G. Öhrwall, and O. Björneholm, Phys. Rev. B **79**, 155448 (2009).

[21] K. Jacobi, Phys. Rev. B **38**, 5869 (1988).

[22] P. J. Benning, D. M. Poirier, N. Troullier, J. L. Martins, J. H. Weaver, R. E. Haufler, L. P. F. Chibante, and R. E. Smalley, Phys. Rev. B **44**, 1962 (1991).

[23] T. Liebsch, O. Plotzke, F. Heiser, U. Hergenhahn, O. Hemmers, R. Wehlitz, J. Viefhaus, B. Langer, S. B. Whitfield, and U. Becker, Phys. Rev. A **52**, 457 (1995).

[24] A. Rüdel, R. Hentges, U. Becker, H. S. Chakraborty, M. E. Madjet, and J. M. Rost, Phys. Rev. Lett. **89**, 125503 (2002).

[25] P. Colavita, G. De Alti, G. Fronzoni, M. Stener, and P. Decleva, Phys. Chem. Chem. Phys. **3**, 4481 (2001).

[26] S. Korica, D. Rolles, A. Reinköster, B. Langer, J. Viefhaus, S. Cvejanović, and U. Becker, Phys. Rev. A **71**, 013203 (2005).

[27] S. Korica, Ph.D. thesis, Technische Universität Berlin, 2006.

[28] J. J. Yeh and I. Lindau, At. Data Nucl. Data Tables **32**, 1 (1985).

[29] I. V. Hertel, H. Steger, J. de Vries, B. Weisser, C. Menzel, B. Kamke, and W. Kamke, Phys. Rev. Lett. **68**, 784 (1992).

7.4 Additional Information

In publication B, multilayers of $Ar@C_{60}$ were examined with photoelectron spectroscopy. We discuss two main points: A hybridization between argon and the C_{60} cage and the cross section of argon in C_{60}. Apart from the data presented in publication B, additional data have been measured that are worth mentioning.

7.4.1 Photoemission spectra with He IIα-radiation:

In publication B, a cross section enhancement of the argon 3p shell, as predicted by Madjet et al.[28], is discussed. The authors calculate the 3p photoionization cross section for free and endohedral argon for photon energies between 10 and 50 eV. In publication B, only the data for He Iα-radiation are shown. We also measured with He IIα-radiation at a photon energy of 40.8 eV. At this energy, the predicted difference between free (∼1.3 Mbarn) and endohedral argon (∼1.7 Mbarn) becomes small. Furthermore it is challenging to detect argon at all because of the low cross section and the noisier spectra due to the lower photon flux of He IIα which is only 5% of He Iα.

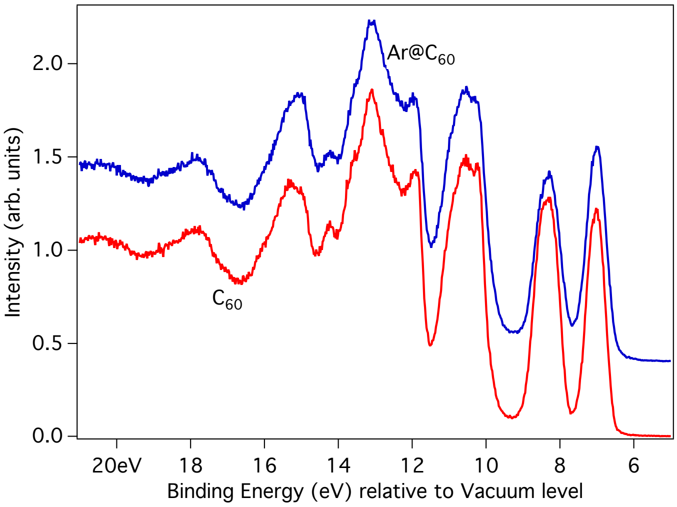

Figure 40: Photoemission spectra of $Ar@C_{60}$ and empty C_{60} measured with He IIα-radiation (hw=40.8 eV). The bonding orbital is not directly visible anymore, the spectra have to be analyzed following the procedure described in publication B to extract the argon related peaks.

In figure 40, the He IIα spectra are presented. In contrast to the He Iα spectra, no more obvious difference can be found. The argon peak has to be extracted by careful data analysis. We proceeded with the same method as used in the publication for the He Iα-spectra, i.e. we form the asymmetry and then fit the asymmetry at exactly the same position with a fourth order polynomial. The fit is then used to correct the C_{60}-spectrum for a different background. Then the difference between the argon spectrum and the corrected C_{60} spectrum is calculated. This is shown in figure 41. The He Iα-data (dashed lines) from the publication are shown as well for comparison. For the graph, the He IIα data have been multiplied by 50 to account for the lower photon flux and the lower cross section. As in the He Iα-data, the bonding orbital can be nicely resolved. The antibonding orbital, however, is hidden below the noise which is much higher for He IIα because of the low photon flux.

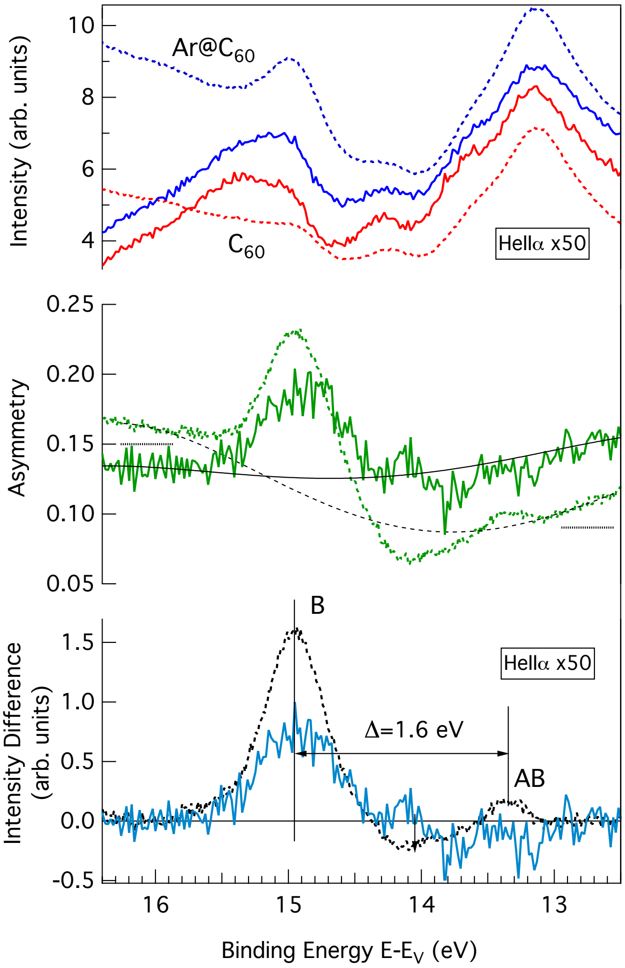

Figure 41: Background subtraction for He IIα-photoemission spectra. The procedure is the same as the one used for the He Iα-spectra described in publication B. For comparison, the He Iα-data are also shown (dashed lines). The He IIα-spectra have been multiplied by 50 to account for the lower photon flux and lower cross section. The position of the fitting mask is the same as for He Iα. In the background subtracted difference spectrum, the bonding orbital is clearly present. However, the antibonding is hidden in the noise.

7.4.2 Cross Section Enhancement

Madjet et al. [28] calculated a giant cross section enhancement for endohedral Ar in C_{60} compared to free Ar. As mentioned in publication B, we have found no evidence for such an enhancement in condensed $Ar@C_{60}$. It should be emphasized, however, that the calculation is probably only valid for gas-phase $Ar@C_{60}$ because the enhancement is maximal in the vicinity of the surface plasmon of C_{60} at ≈20 eV. However, for solid C_{60}, this plasmon is not observed, instead a bulk plasmon at ≈28 eV is measured. [39]

In figure 42, the theoretical cross sections by Madjet et al. and by Yeh et al. [40] as well as our experimental cross sections are shown. They are determined using cross section values for the HOMO of C_{60} of 61.5 Mb (21.2 eV) and 8.2 Mb (40.8 eV) that were measured by Korica et al. [41] for solid C_{60}. The cross section is then determined as

$$\sigma_{Ar} = \frac{I_{Ar3p}}{I_{HOMO}} \cdot \sigma_{HOMO} \cdot \frac{e^{-\frac{d}{2\lambda}}}{\frac{\lambda}{d}(1-e^{-\frac{d}{\lambda}})}$$

where I_{x} are the respective integrals of the orbitals, d the interlayer distance and λ the mean free path which was taken from [42]. The second term in the formula constitutes a correction term that accounts for the short mean free path. In the figure, the experimental values have been determined with and without this factor.

As already shown in the publication, a cross section enhancement cannot be verified at 21.2 eV. In figure 42, the data are shown for 40.8 eV as well. Here also no enhancement is observed.

In a recent calculation for $Xe@C_{60}$, Chakraborty, Madjet et al. [43] predicted a hybridization between the Xe 5s level and the C 2s level. The resulting cross section for the hybrid states is quite different from the free Xe 5s or C 2s cross section. It can be expected that a cross section calcultion including a hybridization between Ar 3p and C_{60} would result in different cross sections than predicted by Madjet et al.

7.4.3 Ratio Homo/Homo-1

C_{60} exhibits well known oscillations in the cross section ratio of the HOMO and the HOMO-1 as a function of the photon energy. Measurements can be found e.g. in [44]. The oscillations have been explained by Xu et al. [29] as an intramolecular interference effect of photoelectron waves.

In figure 43, the valence band spectra of empty C_{60} and $Ar@C_{60}$ are shown again. Here the spectra are normalized to the HOMO. Obviously all orbitals agree quite well, except for the HOMO-1, i.e. the ratio HOMO/HOMO-1 clearly changes. This is also true for the He IIα-data. The results are summarized in table 1.

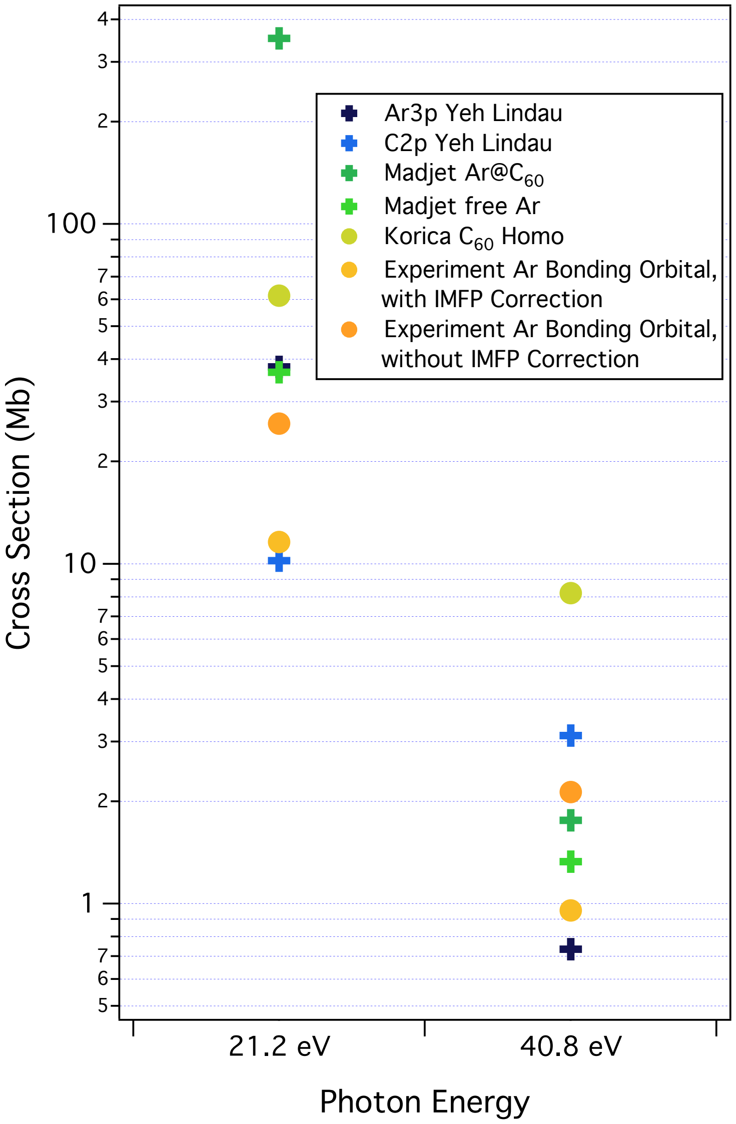

Figure 42: Theoretical (cross symbol) and experimental (circle symbol) cross sections for free and endohedral argon. The experimental values have been obtained by summing up the bonding and antibonding hybrid orbital intensity (He Iα) or by using the bonding orbital (He IIα). An additional term can be included that accounts for the low mean free path, however the results agree worse with the prediction if the correction is included.

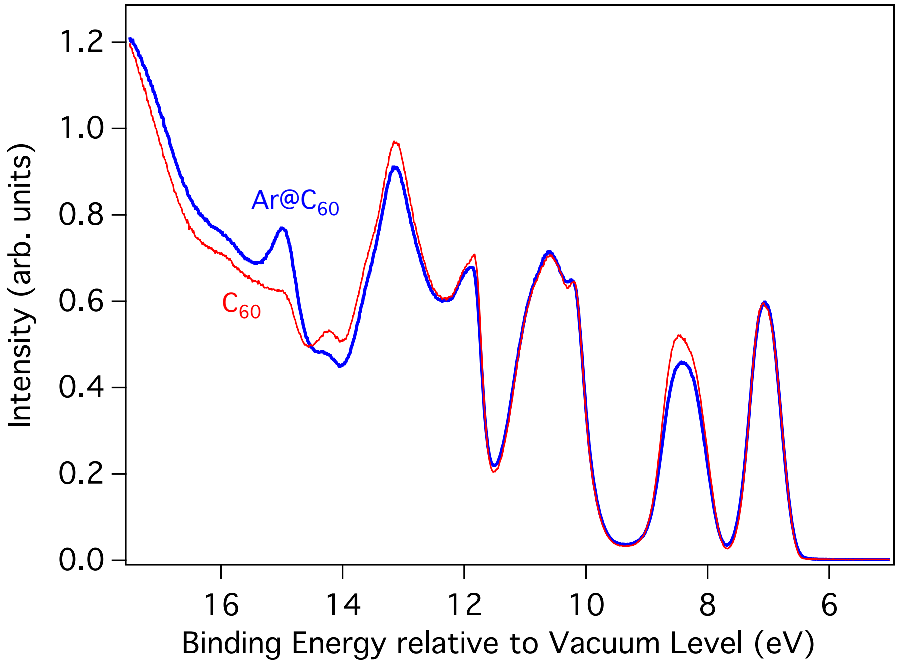

Figure 43: He Iα-photoemission spectra normalized to the HOMO. The spectra agree quite well, except for the HOMO-1.

	$Ar@C_{60}$	C_{60}	Becker [44]
21.2 eV	0.94	0.81	1.06
40.8 eV	0.86	0.70	0.76

Table 1: Cross Section Ratio HOMO/HOMO-1

The different ratio can be explained either by a change in the interference of the photoelectron waves or by energy dependent diffraction effects at the argon atom.

7.4.4 Radiation Damage

In the first photoemission characterisation of $Ar@C_{60}$, DiCamillo et al. [45] reported a depletion of Ar in $Ar@C_{60}$ due to radiation damage. They used Al Kα x-rays (1486.6 eV). As mentioned in publication B, we cannot observe a depletion of argon. However, we clearly observe radiation damage, in the XPS spectra as well as in the UPS spectra. Both are shown in the figures 44 and 45. In the first graph, the width of the HOMO has been measured as a function of time, while the sample was illuminated with He Iα-radiation. The broadening is linear, with a time constant of $3.4 \cdot 10^{-5} eV/s$. Unfortunately, the sample current has not been measured, which makes it impossible to calculate the dose that the sample has been exposed to. Furthermore, different photon energies have been

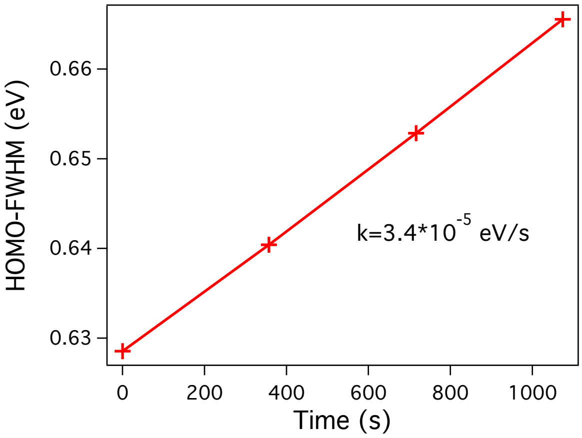

Figure 44: Broadening of the HOMO caused by He Iα radiation damage. The same spectrum has been measured four times within 18 minutes.

used, each with a different flux and spot size, and the sample surface has been moved relative to the light spot several times.

In the XPS spectra, an interesting feature shows up after the C_{60} molecules are desorbed by heating the sample. For a well prepared C_{60} monolayer on Al(111), the molecules should desorb at 730 K [46]. Here, however, not all C_{60} molecules desorb, the characteristic C 1s peak is still visible, yet smaller. On the lower binding energy side, a new peak shows up which does not disappear at typical C_{60} desorption temperatures. It is possibly related to damaged molecules.

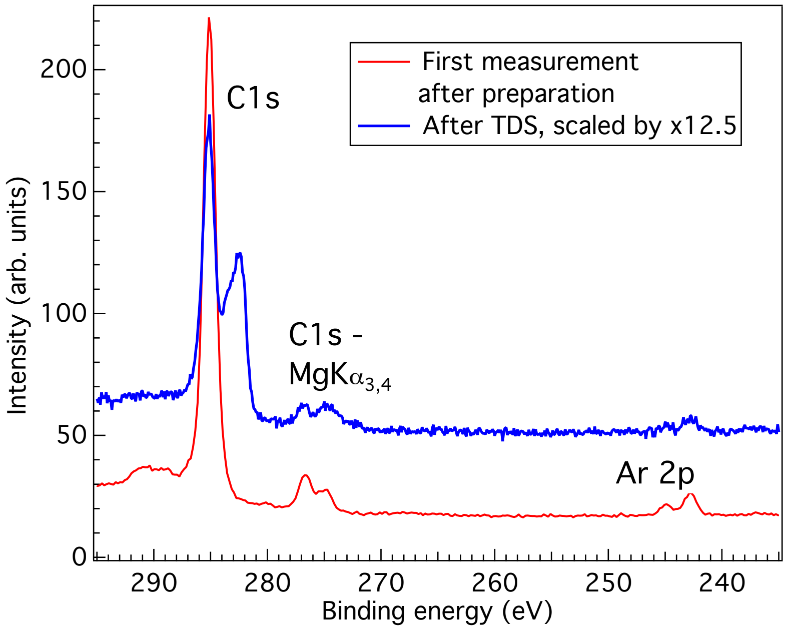

Figure 45: Radiation damage is also visible in the core level spectra. The red curve shows an XPS spectrum immediately after evaporation of $Ar@C_{60}$. Then measurements have been performed on the sample that lasted several hours. Afterwards the molecules were desorbed by heating the sample. However, it was not possible to remove all molecules. A second C 1s component shows up that is maybe related to damaged molecules. The blue curve is multiplied by 12.5 for comparison.

8 $H_2@C_{60}$

8.1 Summary

In addition to the data measured by Tobias Wassmann that are presented in his bachelor thesis [47], new experiments with monolayers of $H_2@C_{60}$are shown. A candidate for the H_2-peak was found, but could not be confirmed yet.

8.2 Introduction

Hydrogen is very difficult to measure in photoemission because it has only one electron which is often transferred to a bonding partner, thus it becomes “invisible”. Furthermore molecular hydrogen dissociates on many metal surfaces. However, molecular hydrogen has been measured in the gas phase. Turner published the first photoemission data of simple molecules in the gas phase, e.g. hydrogen, nitrogen or oxyen [48]. He could clearly resolve the individual vibronic levels of the molecules. Turner’s spectrum of hydrogen, measured with He Iα at 21.218 eV, is shown in figure 46. The coherent peak and several vibronically excited states are observed. The peak intensity corresponds to the population of the individual levels in the final state. There are also measurements of molecular hydrogen in the solid state. Eberhardt et al. [49] adsorbed it on a Cu(100) and a polycrystalline Au surface with a coverage of one layer and five layers. For the monolayer, they observe a FHWM of 0.9 eV, i.e. the vibrational sublevels cannot be resolved anymore. For five layers, the peak is further broadened, a width of 2.1 eV is determined. The authors give a detailed discussion about the line width broadening.

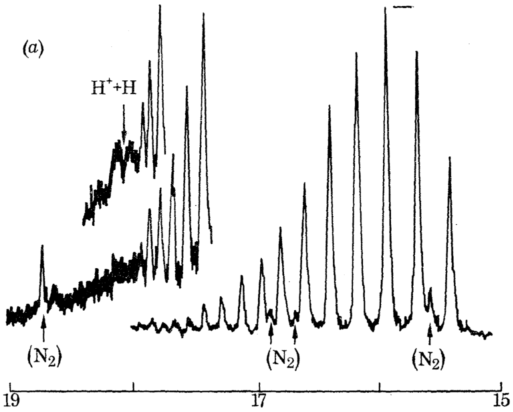

Figure 46: Gas phase spectrum of molecular hydrogen, measured by Turner [48]. Instead of a single peak corresponding to the bonding hydrogen orbital, several additional peaks are visible that are caused by vibrational excitations in the molecule.

When going to $H_2@C_{60}$, several questions have to be adressed:

- Can H_2 in C_{60} be measured with photoemission at all? The H 1s-level has a very low photoionization cross-section. However, the same is true for the C 2p-level which is closest in energy to the H 1s-level. With photoemission, typically signals down to the per mill level can be detected. A simple estimate shows whether the measurement of H_2 is feasible or not. We use the cross sections of Yeh and Lindau [40] for the H 1s and C 2p level at a photon energy of 21.2 eV. The values are given in Mega-barn (Mb). For H 1s Yeh and Lindau calculate 1.888 Mb, for C 2p 6.128 Mb, where the occupation number is one for H 1s and two for C 2p. For one $H_2@C_{60}$-molecule, we calculate therefore:

$$\frac{N_H}{N_C} \cdot \frac{\sigma_{H_{1s}}}{\sigma_{C_{2p}}} = 0.01$$

  i.e. the signal of hydrogen amounts to 1% of the C 2p-intensity. However, there are several complications to this simple calculations. First of all, the C 2p levels hybridize, giving rise to a rather complicated energy level structure. The calculated

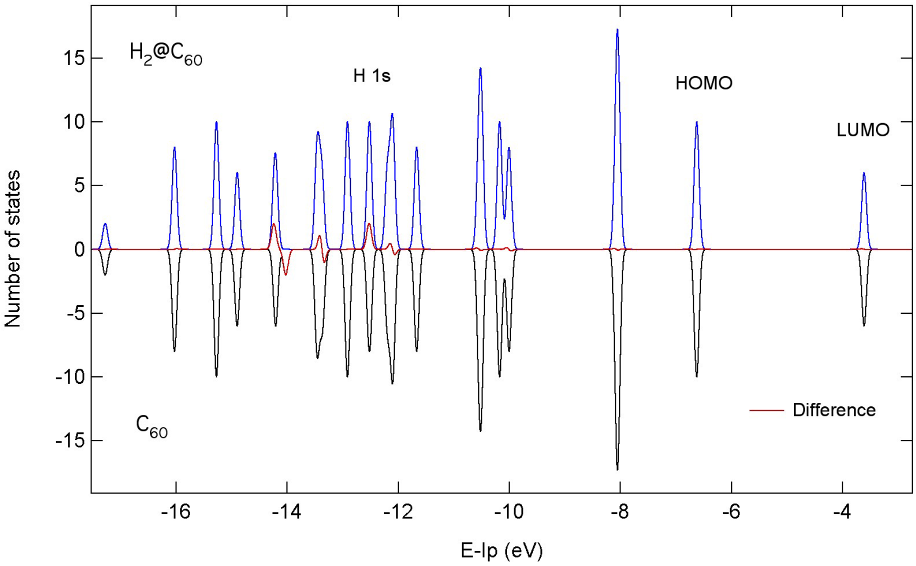

Figure 47: DFT calculations of $H_2@C_{60}$ and C_{60} by Ari Seitsonen [47]. The electronic structure is very similar, except for the region between 12 and 14 eV. The difference between the two molecules is shown as red line.

energy spectrum is plotted in figure 47 for both $H_2@C_{60}$ and C_{60}. The hybridization reduces the number of C 2p electrons in the vicinity of the H 1s level, which increases the propability to measure it. On the other hand, the molecular levels of C_{60} have a cross section which is quite distinct from the C 2p cross section, as discussed in sect. 7.4.2. Likewise, the cross-section of hydrogen in C_{60} may be modified by the surrounding cage.

- Can the vibrational sublevels be observed? As discussed above, in adsorbates the sublevels are either broadened or quenched, depending on the interaction of the adsorbate with the substrate. This leads to the next question:
- How are the molecule and the surrounding cage interacting with each other?

8.3 Experiment

The experiments were performed in two blocks. During his bachelor thesis, Tobias Wassmann mainly measured multilayers of $H_2@C_{60}$. The results are presented in his report “The Electronic Structure and Quantum Dynamics of $H_2@C_{60}$” [47]. No clear signature of hydrogen could be found. Therefore, in a second round of experiments, we focused on monolayers because the reproducibility of preparations and therefore the comparability is easiest for monolayers. They can be obtained by exploiting the fact that the binding energy of the layer in contact to the substrate is higher than the binding energy between C_{60} layers. In practice, the sample is exposed to a temperature ramp until all layers except the last one are desorbed.

Such monolayers have been prepared on an Al(111) crystal. The substrate was cleaned with repeated cycles of argon sputtering and annealing. In total two $H_2@C_{60}$ - and two empty C_{60}-preparations have been examined. Both molecules were evaporated from custom-made copper Knudsen cells, the same as used for publication B. The cleanliness of the samples was examined with XPS. All data presented here have been measured with monochromatized He Iα-radiation (21.218 eV).

In figure 48, the best spectra of C_{60} and $H_2@C_{60}$ are shown. Additionally, the DFT calculation is shown at the bottom as an orientation where spectral contributions by hydrogen are expected. At first sight, the two spectra are very similar, an obvious H_2-related feature cannot be found. Therefore we proceed with the analysis in a similar way as used in publication B. First we form the asymmetry of the two spectra, which is shown in the second panel. Interestingly, a peak in the asymmetry appears closely to the position where it is predicted by DFT. If we take into account the scale correction that was discussed in publication B, the measured peak position matches very well with the expected one. We proceed by fitting a fourth-order polynomial background to the asymmetry, which is fitted only at the positions indicated by the red lines. This background is used to correct the C_{60} spectrum for the different secondary electron background. Then the difference between the two spectra can be calculated, which is presented in the third panel. Here the H_2-peak candidate is nicely resolved. A width of 0.69 eV and a binding energy of 7.4 eV relative to the Fermi level are inferred. To calculate the HOMO cross section, we use the C_{60}-data by Korica et al. [41] that was already used as a reference in the cross section determination of the HOMO of $Ar@C_{60}$ in publication B. We calculate a value of 1.4 Mbarn, which is in good agreement with the value calculated by Yeh and Lindau.

The same spectra as presented in the upper panel were measured with a bias voltage of 10 V to determine the work function. The spectral features should not be influenced by the bias, except for the energy shift and consequently a different transmission of the analyser. In figure 49, in addition to the discussed asymmetry also the one formed from the spectra with bias is shown. The peak candidate is still visible, but the shape changes, and a second peak at lower binding energy shows up. Therefore one has to be very careful in the peak assignment. For the asymmetry with bias, no background subtraction has been attempted.

Is the peak in the third panel really related to hydrogen? To answer this question, we use the second preparation of each molecule. Unfortunately the quality of the preparation is

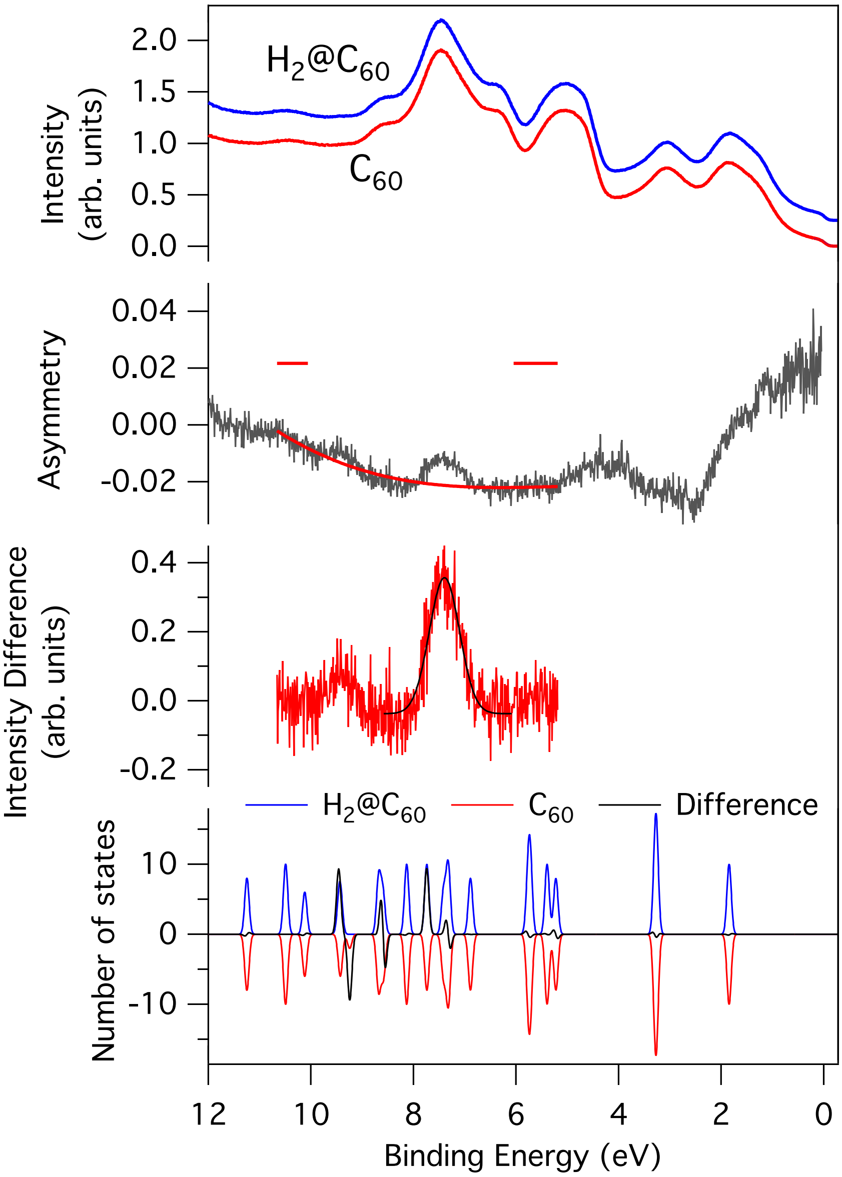

Figure 48: Upper panel: Photoemission spectra of $H_2@C_{60}$ and C_{60}. The spectra are very similar, no obvious difference can be found. Second panel: Asymmetry of $H_2@C_{60}$ and C_{60}, measured with and without bias voltage. In the asymmetry without bias, a possible hydrogen signature is visible. A background subtraction procedure as described in publication B clearly shows the possible hydrogen peak (third panel). However, the asymmetry with bias voltage looks different in the region of interest. In the lower panel, the calculated number of states for $H_2@C_{60}$ and C_{60} and the difference between the two is shown.

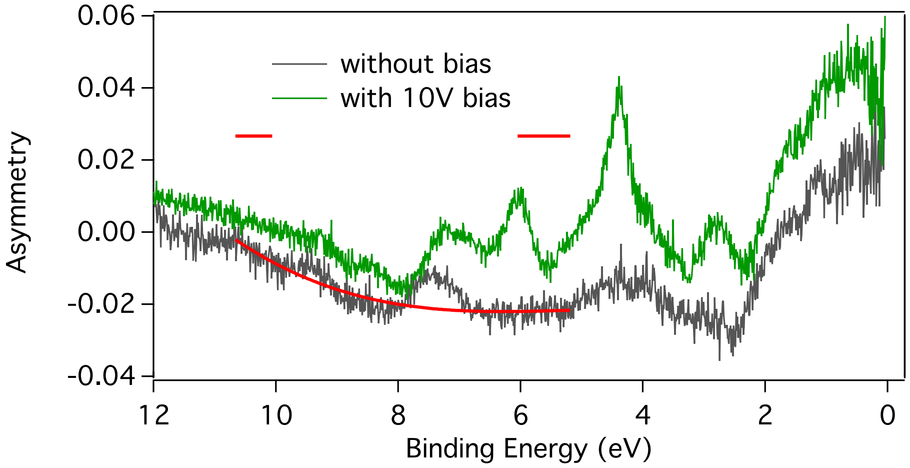

Figure 49: Comparison of the asymmetry of $H_2@C_{60}$ and C_{60}, measured with and without 10V bias.

slightly worse than for the spectra shown above, therefore additional differences in the asymmetry appear. The spectra are shown in figure 50, where the curves labeled with Prep 1 (Preparation 1) are the ones shown in figure 48. In the second panel, several asymmetries are shown. The grey curve shows the asymmetry discussed above with the hydrogen peak candidate as a reference. The yellow curve is the asymmetry of two empty C_{60} preparations, here no hydrogen-related peak should be visible. There is clearly more structure in the asymmetry, and at the position of the possible H_2-peak, there is also a feature in this asymmetry.

The orange curve represents the asymmetry between two $H_2@C_{60}$-samples. Here a strong peak asymmetry at the hydrogen position is visible, which contradicts the expectation if the peak was really related to hydrogen, because then, even if one preparation was completely depleted of hydrogen, the peak asymmetry should not exceed the reference (grey curve).

Finally, the green curve shows the asymmetry between the first $H_2@C_{60}$ preparation and the second C_{60}-sample. Again, a peak at the expected position is visible, but the width is smaller, and the peak is on top of an asymmetry with much more features.

To conclude, we have measured additional photoemission data on $H_2@C_{60}$. We have identified a possible candidate for a hydrogen related peak, but with the present spectra we cannot confirm the peak assignment.

What could be done to clearly identify the hydrogen signature? We believe that after the experiments described here and in the bachelor thesis of Tobias Wassmann, the experimental possibilities at ESCA are exhausted. However, the experiment could be repeated at a synchrotron where the photon energy can be tuned. The cross section of hydrogen increases from 1.884 Mb at 21.218 eV to 3.635 Mb at 16.7 eV, as calculated by Yeh and Lindau[40]. However, this is only a factor of two. The C 2p cross section increases from 6.121 Mb at 21.218 eV to 8.279 Mb at 16.7 eV.

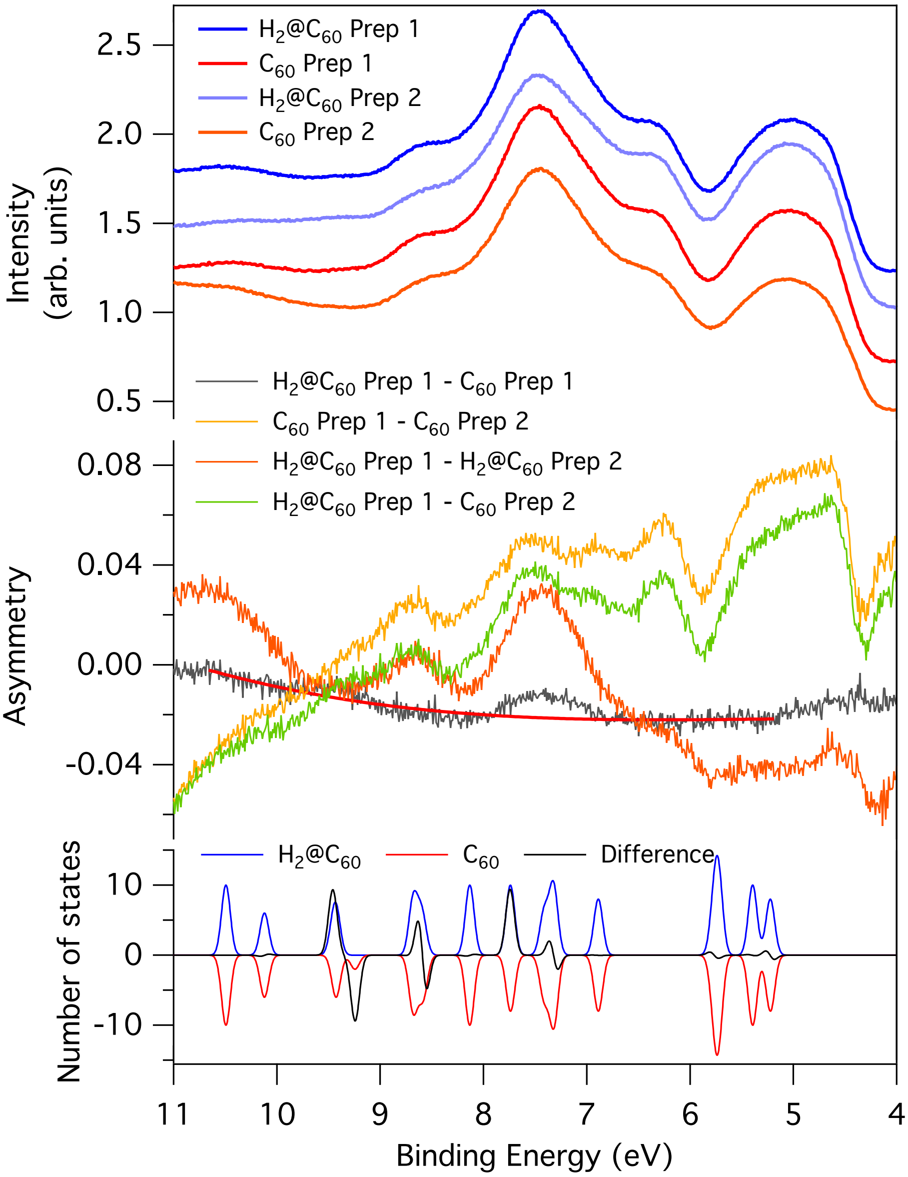

Figure 50: Upper panel: Photoemission spectra of both preparations of both molecules. The second preparations are qualitatively different, therefore the asymmetries involving them have more structure. In the middle panel, several asymmetries are formed that are discussed in the text. The lower panel shows again the DFT calculation.

9 $Dy_3N@C_{80}$

9.1 Summary

The endohedral clusterfullerene $Dy_3N@C_{80}$ is a promising candidate for applications in molecular spintronics. Here, mono-and multilayers of $Dy_3N@C_{80}$ were prepared on a Ni(111) crystal that was covered with a monolayer of h-BN. The magnetic coupling between the substrate and the Dy 4f electrons was studied with XMCD and resonant photoemission with circularly polarized light.

9.2 Introduction

The interest in endohedral fullerenes has been purely academic so far. However, there are possible applications where endohedral fullerenes could indeed bring new functionality. The proposals mainly focus on the magnetic properties of certain endohedral fullerenes, which are interesting for two reasons:

- An intriguing property of several endohedrals is the long lifetime of a spin on a guest atom. The most prominent example is $N@C_{60}$, which has been proposed to be used as a Qbit for quantum computing [1].
- Endofullerenes containing atoms with a high magnetic moment (e.g. gadolinium or dysprosium) are proposed to serve as contrast agents in magnetic resonance imaging (MRI) [50]. The fullerene cage isolates the guest atoms chemically, magnetically and biologically, which is important since rare-earth metals are often toxic.

Magnetic endofullerenes have been examined with techniques like SQUID [51] or XMCD [52], where an external magnetic field is applied and the magnetization of the molecules is measured. Here, instead of an external magnetic field, we study the coupling to a magnetic substrate. Such experiments have been performed for porphyrins on magnetized Co and Ni thins film in[53] and [54], where a ferromagnetic coupling between the metal center of the porphyrin and the substrate could be demonstrated. In the following experiment we try to answer the question if there is also a coupling between an endohedral fullerene and a magnetic surface.
For this purpose, we chose to use $Dy_3N@C_{80}$, a cluster-endofullerene which is already quite well known. It has been studied by Shiozawa et al. [3], who used photoemission and -absorption to measure the electronic structure of the guest cluster and the cage, and by Treier et al. [4] who used XPD to determine the geometric arrangement of the endohedral cluster.

9.3 Experimental

The experiments were performed on a Ni(111) yoke crystal, the same crystal as used for publication A. A single layer of h-BN has been grown on the substrate to decouple the endofullerenes electronically from the substrate, because it is well known that fullerenes on metal substrates often exhibit significant charge transfer. In the model case of C_{60}, the charge transfer between the fullerene and the h-BN covered Ni(111) substrate has been examined by Muntwiler et al [55]. They observe a temperature dependent charging of the C_{60} molecules. At room temperature, the LUMO is occupied by 0.4 electrons, while at 150K it is almost empty.

The growth method for h-BN is described in [56].

A thin film of $Dy_3N@C_{80}$ was grown with a custom-made evaporator called LOTNE (LOw Temperature Nanogram Evaporator) that allows the deposition of small amounts of molecules at relatively low temperatures. It can be approached quite closely to the substrate (here ≈2cm).

All experiments were conducted in the NearNode endstation described in publication A. XAS and XMCD spectra were recorded in the Total Electron Yield (TEY) mode. The spectra were measured at room temperature and at 90 K. The magnetization of the nickel substrate was verified by XMCD. Both resonant photoemission and XMCD data were measured at normal emission, i.e. at an angle of 55° relative to the light incidence direction.

9.4 Results

Two methods were used to detect a possible magnetization of the dysprosium cluster: XMCD and resonant photoemission. The XMCD data are shown in figure 51. In the upper panel, a typical absorption spectrum is shown, measured at the Dy M_5-edge. In the vicinity of the Dy peak, the point density was increased. The relatively high noise is due to the low concentration of Dy on the surface and the low photon flux in this photon energy range (the third harmonic was used). In the lower panel, several asymmetries are shown for at three different azimuthal angles. The first asymmetry consists of spectra at an angle (called 0°) where the substrate dichroism is maximal. Then the sample was rotated by 180°, which should result in an inversion of any magnetic signal. At 270°, any magnetic signal should vanish, because here the magnetization vector is perpendicular to the light incidence direction. Additional spectra at 0° were measured as an additional check. Clearly the noise level increases in the vicinity of the Dy peaks, but a clear evidence of a signal related to a magnetization of Dy cannot be found. The data presented in the figure were measured at ≈90K.

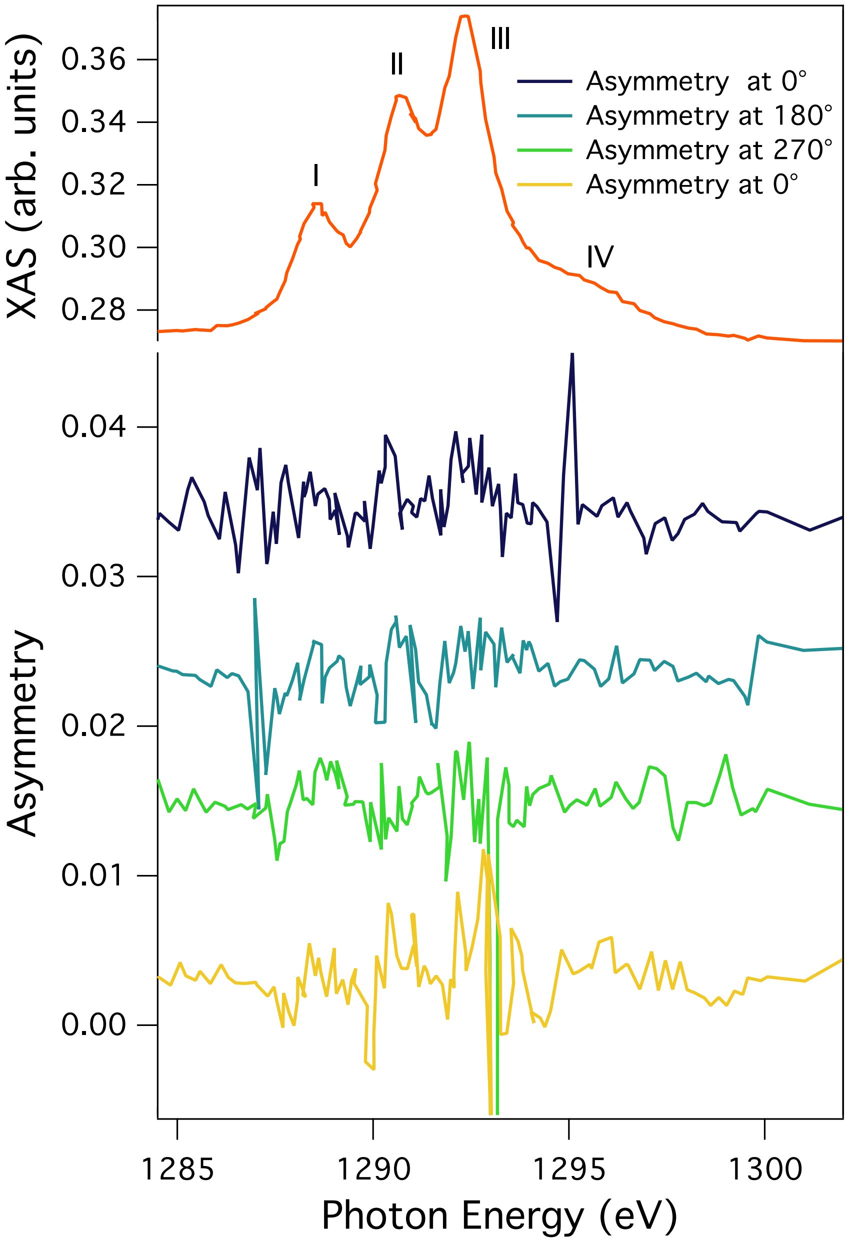

Figure 51: XAS and XMCD spectra of dysprosium at the Dy M_5-edge. In the upper panel, a typical absorption curve is shown, where the polarisation was right-circular. In the lower panel, four different asymmetries are shown. The asymmetry is formed as $AS = \frac{\sigma_+ - \sigma_-}{\sigma_+ + \sigma_-}$. In the first asymmetry, the sample was azimuthally oriented such that the dichroism of the substrate is maximal. This angle is referred to as 0°. In the following asymmetries, the sample has been rotated by 180°, 270° and finally by 360°. All spectra have been recorded at a polar angle of 55° relative to the X-ray incidence direction. The substrate was magnetized by ≈50%, as determined by XMCD. The spectra were recorded at a temperature of ≈90K.

To extract an upper limit for the magnetization from our data, we compare our spectra to the measurements by Bondino et al. [52] who investigated $Dy@C_{82}$ and $Dy_2@C_{88}$ by XMCD at the Dy M_5 edge with an external applied field of 7T at 4K. For both molecules, they measure a maximum asymmetry of about -0.39, where the $Dy_2@C_{88}$-asymmetry is slightly lower. The authors mention that this asymmetry corresponds to a situation where the magnetization is almost at saturation, only 2-5% below.

As mentioned above, we do not observe a peak in the asymmetry in our XMCD spectra. Therefore, we determine the standard deviation of the XMCD spectrum in the region of interest and use it as an upper limit for the magnetization of the Dy-cluster. We define the region of interest as follows: We fit peak I and III in figure 51 with a Gauss curve. We define the region of interest as the position of peak I minus the standard deviation of the fit to the position of peak III plus the standard deviation of the fit. Four all asymmetries, the standard deviation in this region is below 0.0027. Now we have to consider the finite magnetization of our crystal and the reduced XMCD signal due to the experimental geometry. The magnetization was ≈50%. The correction factor for the incidence angle depends on the azimuthal angle, the polar angle was identical for all four spectra. We arrive at an upper limit of the Dysprosium 4f magnetization of ≈2%.

It has to be mentioned that the photo current was quite low, around 100 pA, which is the reason for the noisy spectra. One XMCD spectrum with one polarization took 16 minutes.

In figure 9.4, several valence band photoemission spectra around the resonance photon energy are shown. The strong enhancement directly at the resonance is clearly visible. We measured spectra at this energy for both circular polarizations. The result is displayed in figure 37. In the upper pannel, the photoemission spectra are shown. The two spectra are slightly shifted against each other in energy. The shift is time dependent, it decreases with time. The shift can be measured by tracking the apparent Fermi energy in the spectrum (here the Fermi energy was determined by taking the maximum of the derivative in the vicinity of the expected position), or by tracking the position of a reference peak, e.g. the C 1s-peak. This is shown in figure 54. As expected, both curves follow a similar trend and become constant after about two hours. It has to be mentioned that the C 1s peak is probably not a good reference value since radiation damage on the $Dy_3N@C_{80}$ molecules may shift the C 1s peak additionally, therefore the Fermi edge position is probably the most reliable reference. The shift does not depend on the polarization, only on the time of measuring relative to the first spectrum. The consequence of this shift is shown in the lower panel of figure 37. The green curve represents the asymmetry that is formed without correcting for the energy shift. Artificial peaks appear that might be confused with a magnetic signal. When the spectra in the

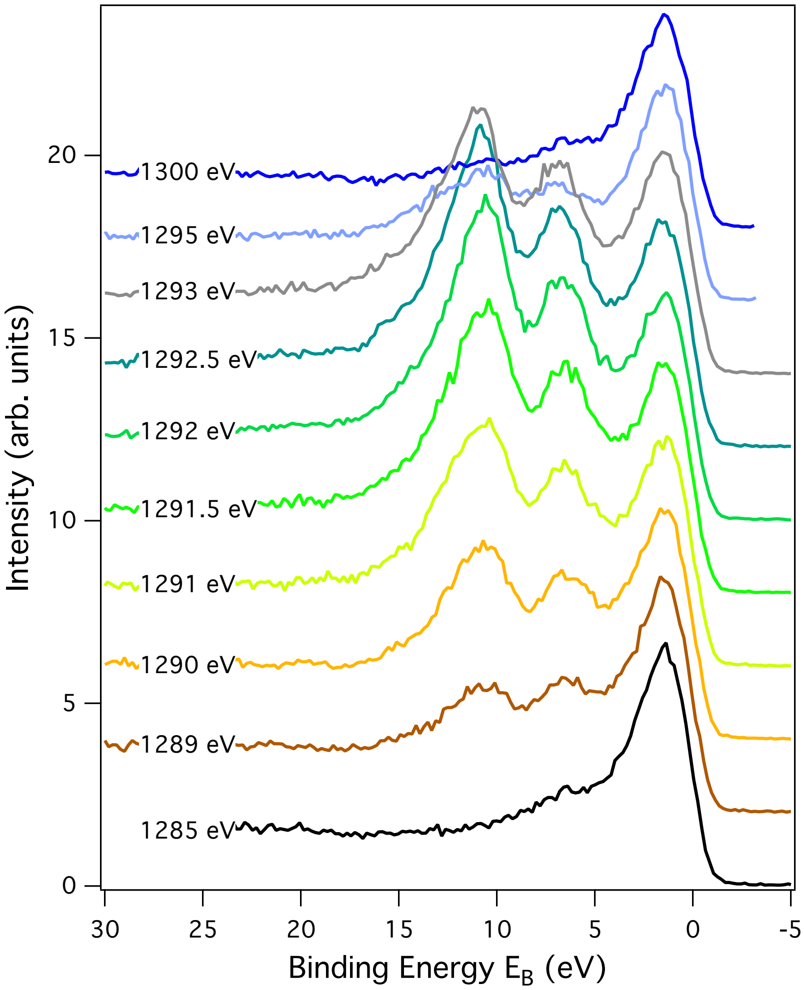

Figure 52: Valence band photoemission spectra of $Dy_3N@C_{80}$ on h-BN/Ni(111), measured with photon energies close to the Dy M_5-edge. The dramatic increase of intensity of the resonant Auger peaks at the resonance photon energy is clearly visible.

upper panel are corrected for the shift, the new asymmetry does not exhibit such peaks anymore, and no more dichroic signal is present, in agreement with the XMCD data.

The origin of the energy shift is not yet clear. There are two possible explanations, either a real photon energy shift at the beamline monochromator (e.g. through warming up of the gratings) or a problem at the energy analyser at NearNode. An easy control experiment would be to measure the energy position of a photoemission peak and an Auger peak simultaneously over a certain time.

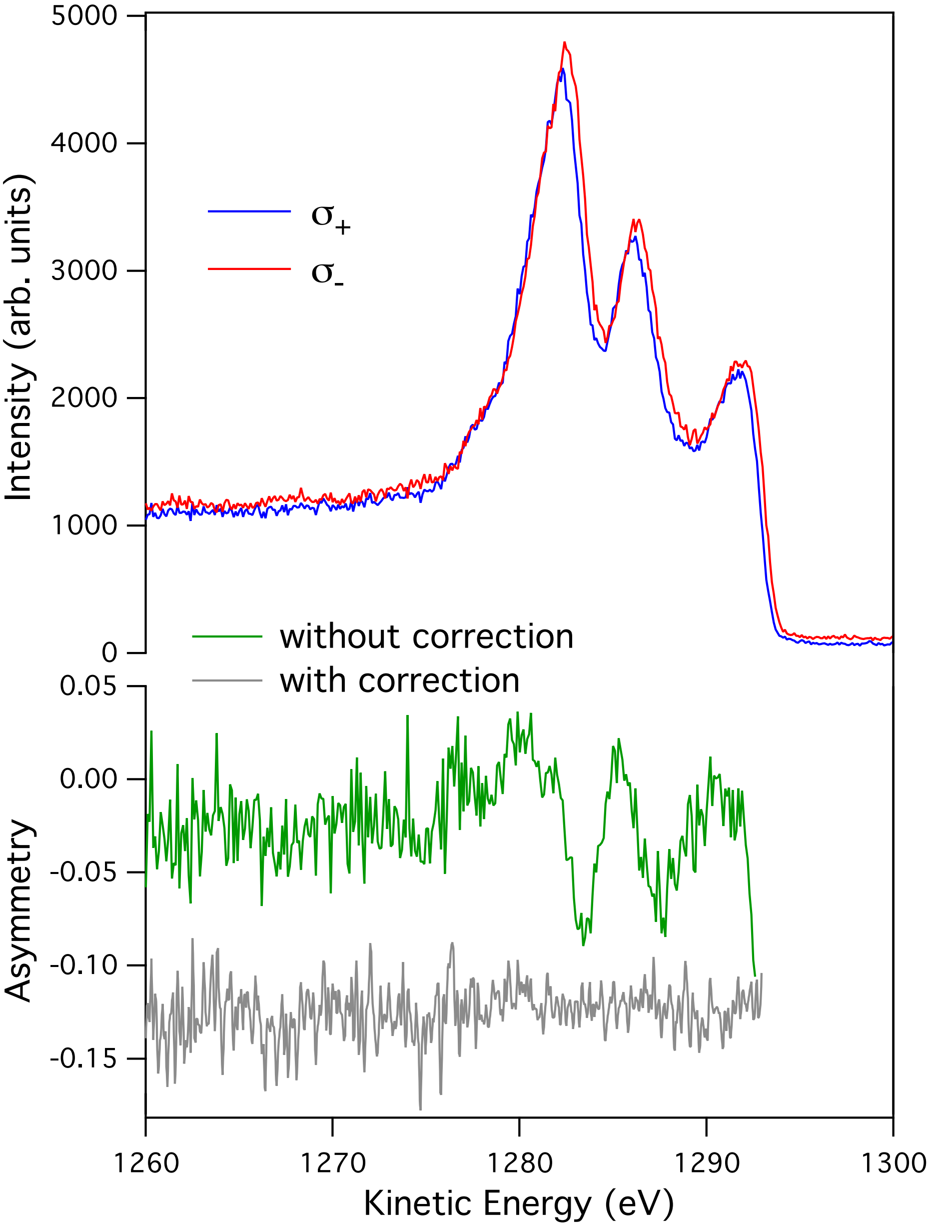

Figure 53: Valence band photoemission spectra at normal emission, measured with both circular polarizations and at room temperature. The magnetization was ≈60%. The sample is azimuthally oriented along the magnetization direction. A slight shift in energy is observed. When the asymmetry is formed without correcting this shift, an artificial dichroism is obtained. After correction, the dichroism disappears.

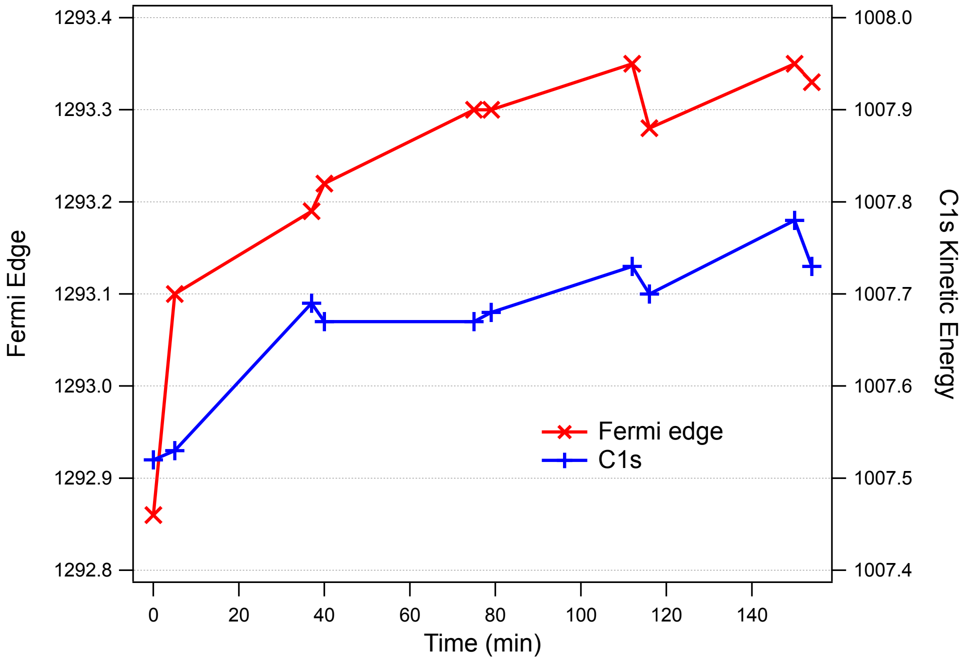

Figure 54: Position of the Fermi edge and the C 1s peak as a function of time. After a certain time the position becomes stable.

9.5 Conclusions

From the data presented above, no magnetization of the Dy cluster could be inferred, neither at room temperature nor at 90K. The data quality is influenced by an energy shift in the spectra, but they can be corrected by using the Fermi edge position.

10 STM Luminescence

10.1 Introduction

A small fraction of the electrons that tunnel between the STM tip and the sample induces photon emission. The main two mechanisms are inelastic electron tunneling (IET), which dominant for metal surfaces, and hot carrier injection, which is characteristic for semiconductors [57]. The photons are collected either by a lens system or by an optical fiber and then are counted either by a photomultiplier, or with a spectrometer including a sensitive, cooled CCD camera which allows to analyze the wavelength of the emitted light. Good reviews were given by Berndt et al. [58] and by Rossel et al. [59].

The photon emission in STM luminescence of noble metals is well understood by now [60, 61]. Metallic systems have also been covered with insulating monolayers and the luminescence properties have been measured, however not spatially resolved [62], [63].

A well studied case for insulating monolayers on a metal surface is the nanomesh [64]. It is a periodically rippled sheet of hexagonal boron nitride on a Rh(111) surface with a lattice constant of 3.2 nm. The goal of this project was to investigate if the periodicity of the nanomesh is reflected in the light emission properties.

The experiments described here were parts of two master theses by Jeanette Schmidlin [65] and Mario Thomann [66]. In the first thesis, J. Schmidlin designed the optical setup, while the author set up the signal electronics and the readout software. First measurements by J. Schmidlin did not show a correlation between the topography of the h-BN nanomesh and the STM luminescence map.

Mario Thomann's master thesis began by installing a new redsensitive photomultiplier (Hamamatsu R5929). The PMT can be cooled with gaseous nitrogen to about -80°C, which decreases the darkcounts by three orders or magnitude to ≈20/s. The detection probability of a 2 eV photon in this setup was ≈0.4%. The results presented below are measurments by M. Thomann.

10.2 Results

In figure 55(a), a topography image of the nanomesh is shown. The scanning parameters are U=-2.5V, i.e. tunneling from the sample to the tip, I=2.6nA, 0.59l/s, scan size 30x15 nm. The image has been recorded with a gold coated tungsten tip, because gold is known to enhance the luminescence efficiency by about one order of magnitude [67]. Despite a modest resolution, the nanomesh is clearly resolved. However, during scanning there are tip changes that modify the image resolution and contrast. The lines where tip changes occur are marked with A, B, C. In figure 55(b), the light intensity map is shown

which is measured in parallel to the topography map. This allows an straightforward correlation of topographic and light intensity features. For a few dozen lines, a strong light emission contrast is observed. The modulation period corresponds to the periodicity of the nanomesh, as inferred from a cut in (b) and (c). Due to the low scanning speed, a strong drift is present in the image, which distorts the hexagonal superlattice. The light intensity is strongest in the region of the so-called "holes", i.e. the region where the h-BN is in close contact to the rhodium surface. Interestingly, the topographic contrast and resolution is reduced in the region of strong photon emission. At A and C, tip changes occur that distinctly change resolution and contrast. However, the onset of strong light emission does not coincide with A or C. The tip condition clearly has an influence on the luminescence properties, but the exact details are not known yet.
The results presented here are part of a publication in "Frontiers of Physics in China" [68].

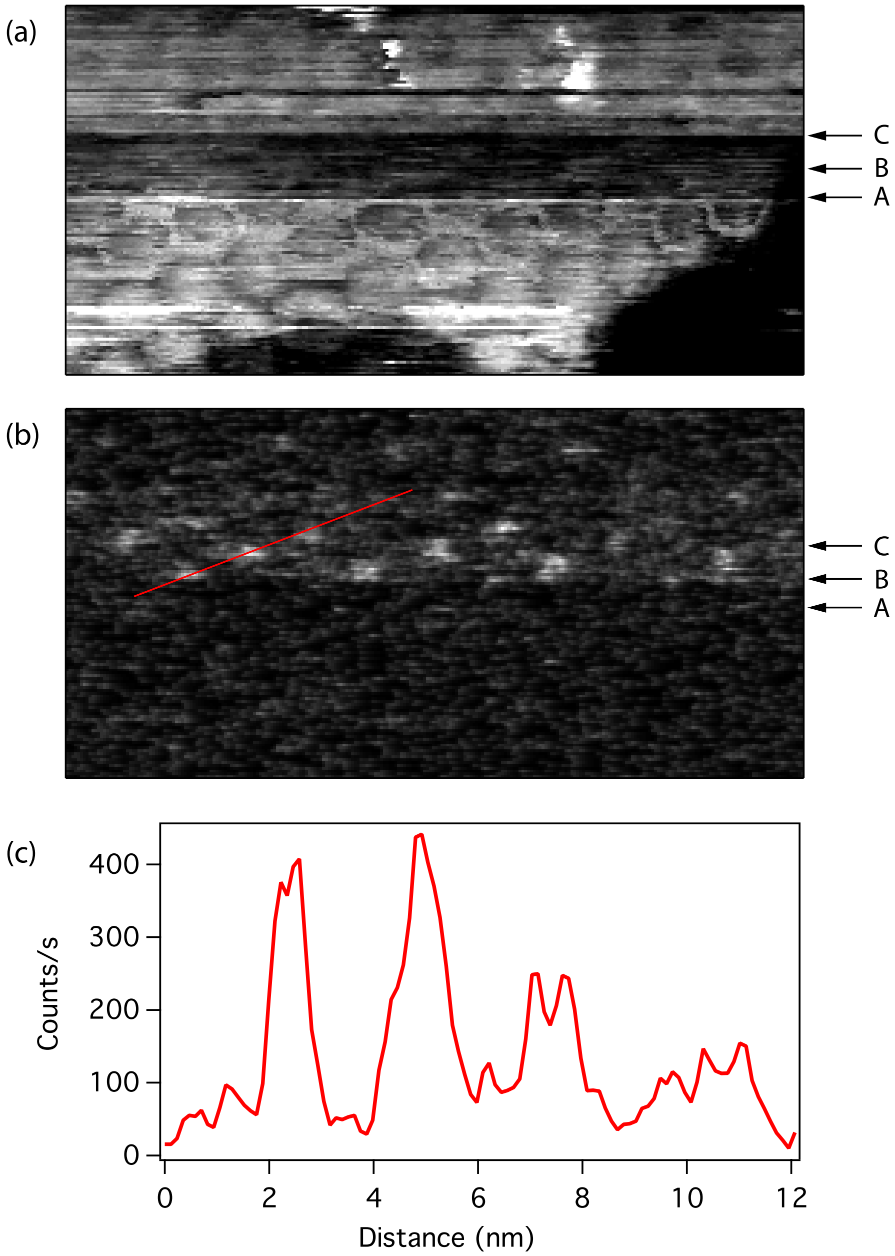

Figure 55: (a) Topography image of the nanomesh (30x15 nm, I=2.6nA, U=-2.5V, 0.59 l/s). During scanning, several tip changes occur, the two most noticeable ones are marked with A and C. (b) Light intensity map, recorded simultaneously with the topography map. The light intensity is periodically modulated, where the periodicity corresponds to the one of the nanomesh. This can be confirmed by taking a cut through the light profile (red line), which is shown in (c). However, due to the slow scanning speed and the resulting drift in the images, the periocity is only 2.5nm instead of 3.2nm. Light emission only occurs for several dozen lines. The onset of light emission is marked with B. The onset does not coincide with the tip changes in A and C. The tip condition certainly plays a crucial role, but exact details remain to be understood.

11 Conclusion and Outlook

In this thesis, the design and construction of a new Mott detector for spin resolved photoemission has been described. The electrons are measured with scintillators which allows to move all electronics to outside of the vacuum chamber. First test data with an unpolarized electron source have been shown. The data demonstrate that the setup is working, asymmetries can be measured. However, the photon detection system is not efficient enough yet, and the detector needs to be thermally stabilized. Both problems have been adressed and solutions are under way.

What are the first experiments that could be performed with the detector? As mentioned above, the Ni(111) yoke sample was extensively used in this thesis. This surface has also been proposed as a cathode for a spin polarized electron gun where the h-BN covered Ni film is excited with two-photon photoemission (M. Hengsberger, M. Muntwiler, T. Greber, J. Lobo-Checa, US patent no. WO 2007/006168). An interesting first experiment would be to use a standard electron gun and measure the electron reflectivity of the h-BN Ni(111) surface with spin resolution as a function of the incident kinetic energy. Precise knowledge of the spin reflectivity may allow to design a simple, yet inert and stable spin polarized electron source. In turn, it might also allow use the h-BN Ni(111) films as targets in VLEED spin detectors, which could enhance the target lifetime of these detectors.

The Mott detector was planned for experiments with magnetic molecules, e.g. the endohedral fullerenes discussed in chapter 9. There, XMCD was used to study the magnetic coupling between the Dy_3N-Cluster and the h-BN covered Ni(111) surface. These experiments could be repeated and improved by using spin resolved photoemission. The main advantage is the permanent availability of the Mott detector, i.e. it is not necessary to apply for beamtime at a synchrotron. This allows a much faster experimental progress. Additionally, when working with a laser as light source, one may study the time evolution of a magnetic molecule after an excitation in a pump-probe scheme.

In the thesis, a method was presented that allows the determination of the magnetization direction relative to the geometric structure. It relies on magnetic circular dichroism, measured with resonant photoemission. The method was demonstrated on a Ni(111) surface, but could be extended to any ferromagnetic system. It should also be applicable to adsorbates or molecules that couple to a ferromagnetic substrate, as mentioned above. An even more interesting application might be to study antiferromagnets or ferrimagnets which are composed of more than one element and where the different magnetic sublattices can be distinguished by photoemission.

The other two endohedral fullerenes that have been analyzed during this thesis are $H_2@C_{60}$ and $Ar@C_{60}$. For $Ar@C_{60}$, a hybridization between the Ar 3p level and a close-lying C_{60} orbital was found. The resulting bonding and antibonding orbital are resolved in the photoemission data. No giant photoemission cross section enhancement could be found. The results are accepted for publication at Physical Review A.

For $H_2@C_{60}$, the H_2 signature could not be unambiguously identified. It would be necessary to perform additional experiments, if possible at a synchrotron where the photon energy can be tuned close to the H 1s absorption edge to increase the hydrogen cross section.

Finally, in the STM luminescence experiment, a correlation between the topography map of the h-BN nanomesh and the simultaneously recorded light map has been found. In the region of the so-called "holes", an increased light emission is observed. However, the light emission properties are strongly tip dependent.

An interesting question in this context is the behaviour of molecules on the nanomesh. Specifically, one could adress the question if the nanomesh is sufficient to insulate the molecule from the substrate such that molecular fluorescence can be observed, as it was the case for porphyrin molecules on $Al_2O_3/NiAl(110)$ Qiu [62]. It could well be the case that a molecule which is trapped in a "hole" is different from a molecule on a "wire". To answer these questions, however, it would be necessary to replace the photomultiplier with an optical spectrometer. Furthermore, the experiment should be performed at low temperatures to increase the stability and minimize sample drift.

12 Appendix

This section contains construction drawings of the Mott detector and the tube at the exit of the electron energy analyzer where the detector is going to be housed.

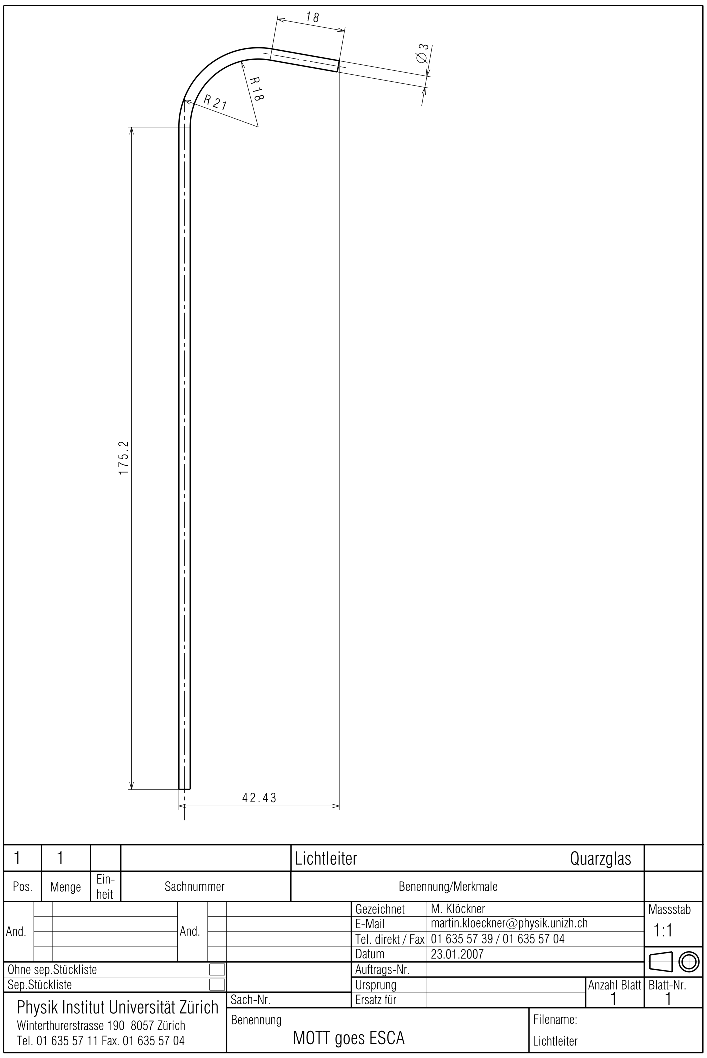

1 | 1 | Lichtleiter | Quarzglas
Pos. | Menge | Ein-heit | Sachnummer | Benennung/Merkmale
Änd. | Änd.
Gezeichnet: M. Klöckner
E-Mail: martin.kloeckner@physik.unizh.ch
Tel. direkt / Fax: 01 635 57 39 / 01 635 57 04
Datum: 23.01.2007
Massstab: 1:1
Ohne sep.Stückliste ☐
Sep.Stückliste ☐
Auftrags-Nr.:
Ursprung:
Ersatz für:
Anzahl Blatt: 1
Blatt-Nr.: 1
Sach-Nr.:

Physik Institut Universität Zürich
Winterthurerstrasse 190 8057 Zürich
Tel. 01 635 57 11 Fax. 01 635 57 04

Benennung: MOTT goes ESCA
Filename: Lichtleiter

Figure 56: Drawing of the light guide. The material is quartz glass.

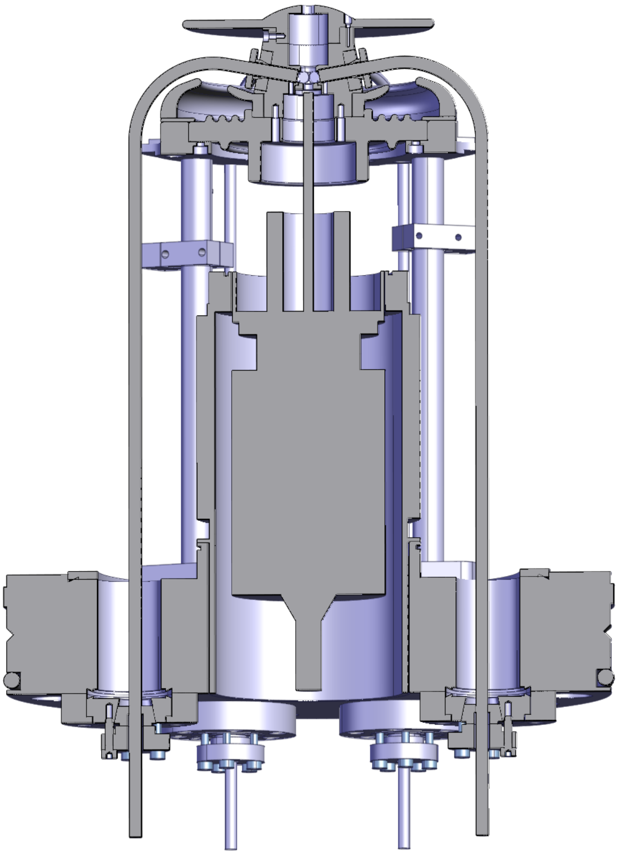

Figure 57: Mott detector core and base flange

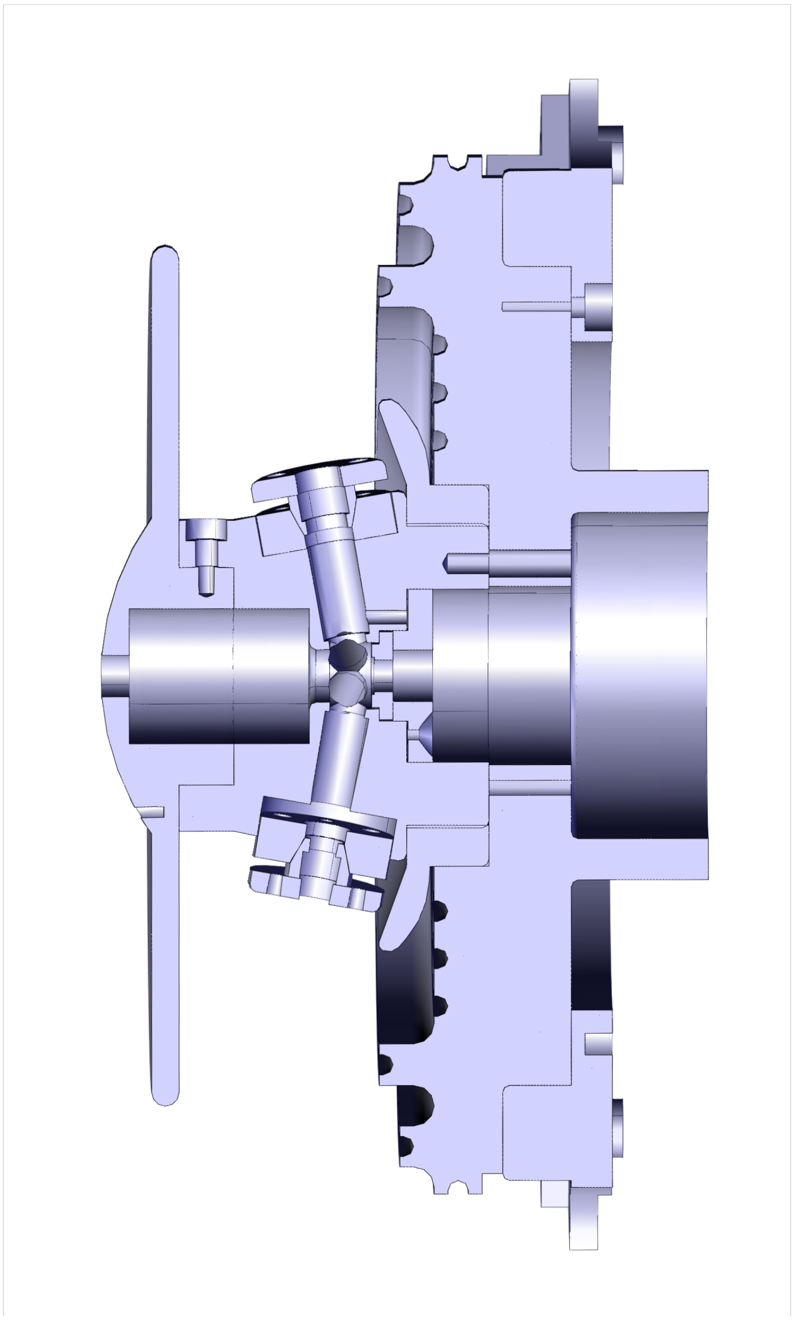

Figure 58: Mott detector core with gold foil, glass rods, insulating ceramics and aluminum support.

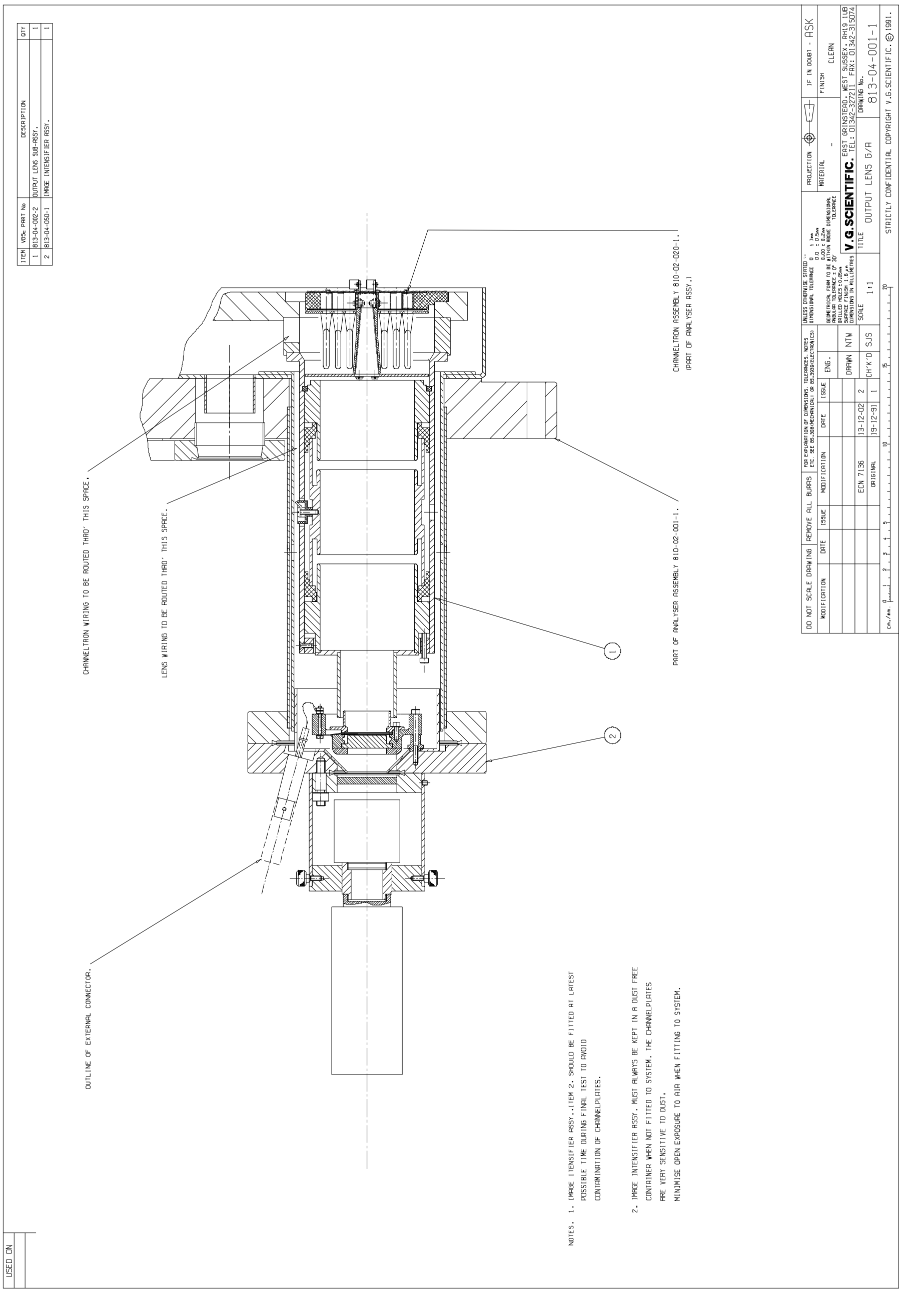

ITEM	VGSc PART No	DESCRIPTION	QTY
1	813-04-002-2	OUTPUT LENS SUB-ASSY.	1
2	813-04-050-1	IMAGE INTENSIFIER ASSY.	1

NOTES. 1. IMAGE ITENSIFIER ASSY..ITEM 2. SHOULD BE FITTED AT LATEST POSSIBLE TIME DURING FINAL TEST TO AVOID CONTAMINATION OF CHANNELPLATES.

2. IMAGE INTENSIFIER ASSY. MUST ALWAYS BE KEPT IN A DUST FREE CONTAINER WHEN NOT FITTED TO SYSTEM. THE CHANNELPLATES ARE VERY SENSITIVE TO DUST.
MINIMISE OPEN EXPOSURE TO AIR WHEN FITTING TO SYSTEM.

Figure 59: Drawing of the channeltron assembly and the tube where the Mott detector is to be installed. Here, the optional XPS imaging unit is drawn in the tube, which was not purchased.

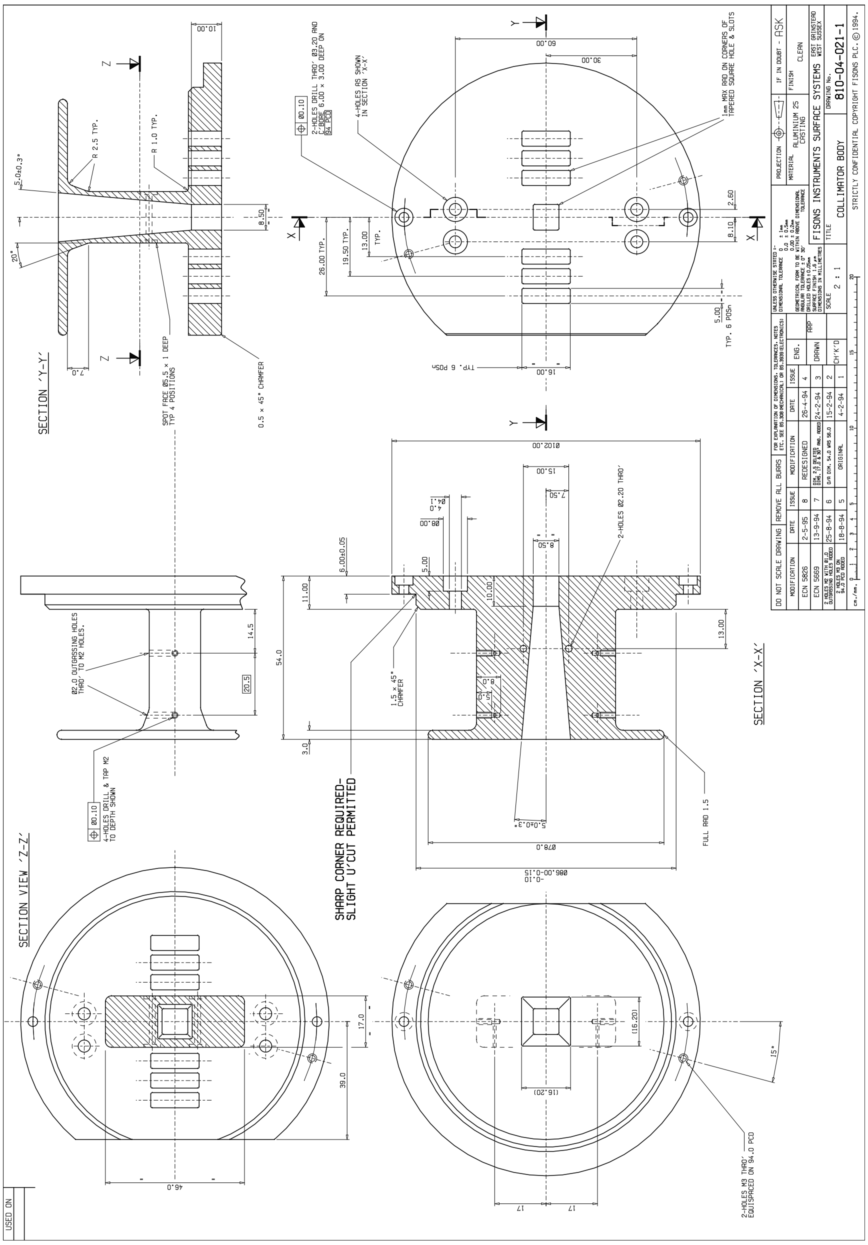

Figure 60: Drawing of the channeltron assembly and the exit slit to the Mott detector.

References

[1] W. Harneit, *Fullerene-based electron-spin quantum computer*, Physical Review A **65**, 032322 (2002), DOI: 10.1103/PhysRevA.65.032322.

[2] L. Dunsch and S. Yang, *Endohedral clusterfullerenes - playing with cluster and cage sizes*, Phys. Chem. Chem. Phys. **9**, 3067 (2007), DOI: 10.1039/b704143h.

[3] H. Shiozawa, H. Rauf, T. Pichler, D. Grimm, X. Liu, M. Knupfer, M. Kalbac, S. Yang, L. Dunsch, B. Büchner, et al., *Electronic structure of the trimetal nitride fullerene Dy3N@C80*, Physical Review B **72**, 1 (2005), DOI: 10.1103/PhysRevB.72.195409.

[4] M. Treier, P. Ruffieux, R. Fasel, F. Nolting, S. Yang, L. Dunsch, and T. Greber, *Looking inside an endohedral fullerene: Inter- and intramolecular ordering of Dy3N@C80 (Ih) on Cu(111)*, Physical Review B **80**, 081403 (2009), DOI: 10.1103/PhysRevB.80.081403.

[5] J. Kessler, *Polarized Electrons* (Springer, 1985).

[6] J. Dil, *Spin and angle resolved photoemission on non-magnetic low-dimensional systems*, Journal of Physics: Condensed Matter **21**, 403001 (2009), DOI: doi:10.1088/0953-8984/21/40/403001.

[7] N. Mott, *The scattering of fast electrons by atomic nuclei*, Proceedings of the Royal Society of London, Series A **124**, 425 (1929).

[8] N. Mott, *The polarisation of electrons by double scattering*, Proceedings of the Royal Society of London, Series A **135**, 429 (1932).

[9] M. Hoesch, *Spin-resolved fermi surface mapping*, Ph.D. thesis, Universität Zürich (2002).

[10] R. Allenspach, *Spin-polarized scanning electron microscopy*, IBM J. Res. Develop. **44**, 553 (2000), DOI: http://dx.doi.org/10.1147/rd.444.0553.

[11] V. Petrov, V. Grebenshikov, A. Andronov, P. Gabdullin, and A. Maslevtcov, *Ultrafast compact classical mott polarimeter*, Review of Scientific Instruments **78**, 025102 (2007), DOI: 10.1063/1.2437112.

[12] Petrov, V.N., private communication.

[13] M. A. Khakoo, D. Roundy, C. Hicks, N. Margolis, E. Yeung, A. W. Ross, and T. J. Gay, *Monte carlo studies of mott scattering asymmetries from gold foils*, Physical Review A **64**, 052713 (2001), DOI: 10.1103/PhysRevA.64.052713.

[14] M. Yasuda, K. Tamura, H. Kawata, K. Murata, and M. Kotera, *A monte carlo study of spin-polarized electron backscattering from thin gold films*, Nuclear Instruments and Methods in Physics Research B **183**, 196 (2001), DOI: 10.1016/S0168-583X(01)00707-8.

[15] S. Qiao and A. Kakizaki, *Monte carlo calculations for the design of mott scattering spin polarimeters*, Review of Scientific Instruments **68**, 4017 (1997), DOI: 10.1063/1.1148381.

[16] E. V. D. van Loef, P. Dorenbos, C. W. E. van Eijk, K. Krämer, and H. U. Güdel, *High-energy-resolution scintillator: Ce3+ activated LaBr3*, Applied Physics Letters **79**, 1573 (2001), DOI: 10.1063/1.1385342.

[17] V. Petrov, M. Landolt, M. Galaktionov, and B. Yushenkov, *A new compact 60 kV Mott polarimeter for spin polarized electron spectroscopy*, Review of Scientific Instruments **68**, 4385 (1997), DOI: 10.1063/1.1148400.

[18] M. von Ardenne, *Tabellen zur angewandten Physik, Band III* (1973).

[19] E. R. I. Abraham and E. A. Cornell, *Teflon feedthrough for coupling optical fibers into ultrahigh vacuum systems*, Applied Optics **37**, 1762 (1998).

[20] Hamamatsu Photonics, *Photomultiplier Tubes - Basics and Applications* (2007).

[21] A. Dorokhov, A. Glauser, Y. Musienko, C. Regenfus, S. Reucroft, and J. Swain, *Study of the hamamatsu avalanche photodiode at liquid nitrogen temperatures*, Nuclear Instruments and Methods in Physics Research Section A: Accelerators, Spectrometers, Detectors and Associated Equipment **504**, 58 (2003), DOI: 10.1016/S0168-9002(03)00753-8.

[22] http://simion.com.

[23] Heraeus Quarzglas GmbH, *Quartz glass for optics: Data and properties*.

[24] V. N. Petrov, M. S. Galaktionov, and A. S. Kamochkin, *Comparative tests of conventional and retarding-potential mott polarimeters*, Review of Scientific Instruments **72**, 3728 (2001), DOI: 10.1063/1.1396658.

[25] C. Chen, N. Smith, and F. Sette, *Exchange, spin-orbit, and correlation effects in the soft-x-ray magnetic-circular-dichroism spectrum of nickel*, Physical Review B **43**, 6785 (1991), DOI: 10.1103/PhysRevB.43.6785.

[26] H. Daimon, F. Matsui, F. Guo, and T. Matsushita, *Circularly polarized x-ray photoelectron diffraction - stereo photograph of atomic arrangement*, Journal of Electron Spectroscopy and Related Phenomena **156-158**, 1 (2007), DOI: 10.1016/j.elspec.2006.12.004.

[27] H. Daimon, T. Nakatani, S. Imada, S. Suga, Y. Kagoshima, and T. Miyahara, *Strong circular dichroism in photoelectron diffraction from nonchiral, nonmagnetic material - direct observation of rotational motion of electrons*, Jpn. J. Appl. Phys. **32**, 1480 (1993), DOI: 10.1143/JJAP.32.L1480.

[28] M. E. Madjet, H. S. Chakraborty, and S. T. Manson, *Giant enhancement in low energy photoemission of Ar confined in C60*, Physical Review Letters **99**, 1 (2007).

[29] Y. Xu, M. Tan, and U. Becker, *Oscillations in the photoionization cross section of C60*, Physical Review Letters **76**, 3538 (1996), DOI: 10.1103/PhysRevLett.76.3538.

[30] M. Amusia, *Photoionization and vacancy decay of endohedral atoms*, Journal of Electron Spectroscopy and Related Phenomena **161**, 112 (2007), DOI: 10.1016/j.elspec.2007.04.004.

[31] S. Lo, A. Korol, and A. Solov'yov, *Dynamical screening of an endohedral atom*, Physical Review A **79**, 063201 (2009), DOI: 10.1103/PhysRevA.79.063201.

[32] V. Dolmatov, *Structure and photoionization of confined atoms*, Radiation Physics and Chemistry **70**, 417 (2004), DOI: 10.1016/j.radphyschem.2003.12.024.

[33] M. Y. Amusia, A. S. Baltenkov, and L. V. Chernysheva, *Photoionization of Xe 3d electrons in molecule Xe@C60: Interplay of intradoublet and confinement resonances*, Physical Review A **75**, 1 (2007), DOI: 10.1103/PhysRevA.75.043201.

[34] A. Takeda, Y. Yokoyama, S. Ito, T. Miyazaki, H. Shimotani, K. Yakigaya, T. Kakiuchi, H. Sawa, H. Takagi, K. Kitazawa, et al., *Superconductivity of doped Ar@C60*, Chemical communications pp. 912–4 (2006).

[35] K. Yakigaya, A. Takeda, Y. Yokoyama, S. Ito, T. Miyazaki, T. Suetsuna, H. Shimotani, T. Kakiuchi, H. Sawa, H. Takagi, et al., *Superconductivity of doped Ar@C60*, New Journal of Chemistry **31**, 973 (2007).

[36] H. Steinrück, *Angle-resolved photoemission studies of adsorbed hydrocarbons*, J. Phys.: Condens. Matter 8 **8**, 6465 (1996), DOI: 10.1088/0953-8984/8/36/003.

[37] O. Björneholm, H. Tillborg, A. Nilsson, N. Martensson, H. Agren, and C. Liegener, *Vibrationally and orientationally selective probing of intramolecular potentials in physisorbed molecules*, Physical Review Letters **73**, 2551 (1994), DOI: 10.1103/PhysRevLett.73.2551.

[38] V. Averbukh and L. S. Cederbaum, *Interatomic electronic decay in endohedral fullerenes*, Physical Review Letters **96**, 1 (2006), DOI: 10.1103/PhysRevLett.96.053401.

[39] S. Wu, K. Xun, J. Deng, J. Yao, F. Liu, S. Lu, Z. Wang, R. Han, and Z. Gu, *Observation of the development of the electronic structure of C60 films from submonolayer coverage to two and three dimensionality*, Physical Review B **47**, 13830 (1993), DOI: 10.1103/PhysRevB.47.13830.

[40] J. Yeh and I. Lindau, *Atomic subshell photoionization cross sections and asymmetry parameters*, Atomic Data and Nuclear Data Tables **32**, 1 (1985), DOI: 10.1016/0092-640X(85)90016-6.

[41] S. Korica, *Photoionization and photofragmentation of fullerenes*, Ph.D. thesis, Technische Universität Berlin (2006).

[42] A. Goldoni, L. Sangaletti, F. Parmigiani, G. Comelli, and G. Paolucci, *Surface and bulk normal state transport properties in K3C60*, Physical Review Letters **87**, 076401 (2001), DOI: 10.1103/PhysRevLett.87.076401.

[43] H. Chakraborty, M. Madjet, T. Renger, J. Rost, and S. Manson, *Photoionization of hybrid states in endohedral fullerenes*, Physical Review A **79**, 061201 (2009), DOI: 10.1103/PhysRevA.79.061201.

[44] S. Korica, D. Rolles, A. Reinköster, B. Langer, J. Viefhaus, S. Cvejanović, and U. Becker, *Partial cross sections and angular distributions of resonant and non-resonant valence photoemission of C60*, Physical Review A **71**, 1 (2005), DOI: 10.1103/PhysRevA.71.013203.

[45] B. DiCamillo, R. Hettich, G. Guiochon, R. Compton, M. Saunders, H. Jiménez-Vázquez, A. Khong, and R. Cross, *Enrichment and characterization of a noble gas fullerene: Ar@C60*, Journal of Physical Chemistry **100**, 9197 (1996), DOI: 10.1021/jp960049k.

[46] A. Maxwell, P. Brühwiler, D. Arvanitis, J. Hasselström, M.-J. Johansson, and N. Mårtensson, *Electronic and geometric structure of C60 on Al(111) and Al(110)*, Physical Review B **57**, 7312 (1998), DOI: 10.1103/PhysRevB.57.7312.

[47] T. Wassmann, *The electronic structure and quantum dynamics of H2@C60*, Bachelor's thesis, Universität Zürich (2007).

[48] D. Turner, *Molecular photoelectron spectroscopy*, Philosophical Transactions of the Royal Society of London, Series A, Mathematical and Physical Sciences **268**, 7 (1970).

[49] W. Eberhardt, R. Cantor, F. Greuter, and E. Plummer, *Photoemission from condensed layers of H2 on Cu and Au*, Solid State Communications **42**, 799 (1982), DOI: 10.1016/0038-1098(82)90009-6.

[50] H. Shinohara, *Endohedral metallofullerenes*, Reports on Progress in Physics **63**, 843 (2000).

[51] M. Wolf, K. Müller, D. Eckert, Y. Skourski, P. Georgi, R. Marczak, M. Krause, and L. Dunsch, *Magnetic moments in Ho3N@C80 and Tb3N@C80*, Journal of Magnetism and Magnetic Materials **290-291**, 290 (2005), DOI: 10.1016/j.jmmm.2004.11.211.

[52] F. Bondino, C. Cepek, N. Tagmatarchis, M. Prato, H. Shinohara, and A. Goldoni, *Element-specific probe of the magnetic and electronic properties of Dy incar-fullerenes*, Journal of Physical Chemistry B **110**, 7289 (2006), DOI: 10.1021/jp055938z.

[53] A. Scheybal, T. Ramsvik, R. Bertschinger, M. Putero, F. Nolting, and T. Jung, *Induced magnetic ordering in a molecular monolayer*, Chemical Physics Letters **411**, 214 (2005), DOI: 10.1016/j.cplett.2005.06.017.

[54] H. Wende, M. Bernien, J. Luo, C. Sorg, N. Ponpandian, J. Kurde, J. Miguel, M. Piantek, X. Xu, P. Eckhold, et al., *Substrate-induced magnetic ordering and switching of iron porphyrin molecules*, Nature Materials **6**, 516 (2007), DOI: 10.1038/nmat1932.

[55] M. Muntwiler, W. Auwärter, A. P. Seitsonen, J. Osterwalder, and T. Greber, *Rocking-motion-induced charging of C60 on h-BN/Ni(111)*, Physical Review B **71**, 1 (2005), DOI: 10.1103/PhysRevB.71.121402.

[56] A. Nagashima, N. Tejima, Y. Gamou, T. Kawai, and C. Oshima, *Electronic dispersion relations of monolayer hexagonal boron nitride formed on the Ni(111) surface*, Physical Review B **51**, 4606 (1995), DOI: 10.1103/PhysRevB.51.4606.

[57] N. Nilius, *Properties of oxide thin films and their adsorption behavior studied by scanning tunneling microscopy and conductance spectroscopy*, Surface Science Reports **64**, 595 (2009), DOI: 10.1016/j.surfrep.2009.07.004.

[58] R. Berndt, in *Scanning Probe Microscopy* (Springer, Berlin, 1998).

[59] F. Rossel, M. Pivetta, and W. Schneider, *Luminescence experiments on supported molecules with the scanning tunneling microscope*, Surface Science Reports **65**, 129 (2010), DOI: 10.1016/j.surfrep.2010.06.001.

[60] R. Berndt, J. Gimzewski, and P. Johansson, *Inelastic tunneling excitation of tip-induced plasmon modes on noble-metal surfaces*, Physical Review Letters **67**, 3796 (1991), DOI: 10.1103/PhysRevLett.67.3796.

[61] R. Berndt and J. Gimzewski, *Photon emission in scanning tunneling microscopy: Interpretation of photon maps of metallic systems*, Physical Review B **48**, 4746 (1993), DOI: 10.1103/PhysRevB.48.4746.

[62] X. H. Qiu, *Vibrationally resolved fluorescence excited with submolecular precision*, Science **299**, 542 (2007), DOI: 10.1126/science.1078675.

[63] E. Ćavar, *Electronic and optical properties of supported C60 molecules studied by scanning tunneling microscopy*, Ph.D. thesis, EPFL (2005).

[64] S. Berner, M. Corso, R. Widmer, O. Groening, R. Laskowski, P. Blaha, K. Schwarz, A. Goriachko, H. Over, S. Gsell, et al., *Boron nitride nanomesh: functionality from a corrugated monolayer*, Angewandte Chemie (International ed. in English) **46**, 5115 (2007), DOI: 10.1002/anie.200700234.

[65] J. Schmidlin, *Luminiszenz von h-BN nanomesh*, Master's thesis, Universität Zürich (2008).

[66] M. Thomann, *Photon emission during inelastic electron tunneling with nanometer resolution from the h-BN nanomesh*, Master's thesis, Universität Zürich (2009).

[67] R. Berndt, J. Gimzewski, and P. Johansson, *Electromagnetic interactions of metallic objects in nanometer proximity*, Physical Review Letters **71**, 3493 (1993), DOI: 10.1103/PhysRevLett.71.3493.

[68] H. Ma, M. Thomann, J. Schmidlin, S. Roth, M. Morscher, and T. Greber, *Corrugated single layer templates for molecules: From h-BN nanomesh to graphene based quantum dot arrays*, Frontiers of Physics in China **5**, 387 (2010), DOI: 10.1007/s11467-010-0137-0.

Curriculum vitae

Name	MORSCHER Martin
Birth	12.12.1979 in Feldkirch, Austria
Nationality	Austria

Education

1998	Matura, BG Bludenz, Austria
1999 – 2005	ETH Zurich, Studies of physics
Nov 2004 – March 2005	Diploma thesis in physics ‘Hexagonal Boron Nitride on Pd(111): Nanomesh or Moiré Pattern?’ at the Physik-Institut, University of Zurich
since Jan 2006	PhD studies of ‘Tools for Investigating Molecular Magnetism: A New Mott Detector and Resonant Photoelectron Diffraction with Circular Dichroism’ at the Physik-Institut, University of Zurich, Switzerland in the surface physics group of Prof. J. Osterwalder

Teaching

2002 – 2005	Teaching assistant, Mathematics department, ETH Zurich
since Jan 2006	Teaching assistant, Physik-Institut, University of Zurich basic courses in mechanics, thermodynamics, optics, electricity and magnetism; lab-courses for medical and for physics students; solid state physics

Publications

- M. Morscher, A. P. Seitsonen, S. Ito, H. Takagi, N. Dragoe, and T. Greber, *Strong 3p-T1u hybridization in Ar@C60*, Phys. Rev. A **82**, (2010) 051201 , DOI: 10.1103/PhysRevA.82.051201.
- H. F. Ma, M. Thomann, J. Schmidlin, S. Roth, M. Morscher, and T. Greber, *Corrugated single layer templates for molecules: From h-BN nanomesh to graphene based quantum dot arrays* Front. Phys. China **5**, (2010) 387-392 , DOI: 10.1007/s11467-010-0137-0.
- T. Okuda, J. Lobo-Checa, W. Auwärter, M. Morscher, M. Hoesch, V. N. Petrov, M. Hengsberger, A. Tamai, A. Dolocan, C. Cirelli, M. Corso, M. Muntwiler, M. Klöckner, M. Roos, J. Osterwalder, and T. Greber, *Exchange splitting of the three Gammabar surface states of Ni(111) from three-dimensional spin- and angle-resolved photoemission spectroscopy* Physical Review B **80**, (2009), 180404 DOI: 10.1103/PhysRevB.80.180404.
- M. Morscher, M. Corso, T. Greber, and J. Osterwalder, *Formation of single layer h-BN on Pd(111)*, Surface Science **600**, (2006), 3280-3284 DOI: 10.1016/j.susc.2006.06.016.